National Technical University of Athens
School of Mechanical Engineering
Fluids Department
Parallel CFD & Optimization Unit

Development of a Simulation Tool for the Lubrication between the Piston Rings and the Cylinder Bore of an Internal Combustion Engine

Diploma Thesis

Alexandra-Ioanna Liosi

Academic advisor:
Kyriakos C. Giannakoglou, Professor NTUA

Industrial advisor:
Dr. Konstantinos Gkagkas, Expert Toyota Motor Europe

Athens, 2021

Acknowledgments

Firstly, I am thankful to my professor Kyriakos Gianniakoglou, who suggested this industrial subject in collaboration with Toyota Motor Europe for my diploma thesis. Ever since the beginning of my studies, he has been an inspiring figure through his vast knowledge and his unique teaching style. I am very satisfied, that I was given the opportunity to work and develop my engineering insight under his academic supervision on this challenging topic.

Secondly, I would like to express my sincere gratitude for my industrial supervisor Dr. Konstantinos Gkagkas. During my internship, he was always very eager to help me, answer any of my questions and provide me with insightful guidance. Also, I would like to thank Dr. Marco Di Genaro and the rest of the Advanced Research department for creating a very warm, working environment and assisting me in any means possible. I am grateful to Toyota Motor Coorporation engineers whose contribution was essential for further developing the project.

Thirdly, I wholeheartedly appreciate the support, that I received from Dr. Konstantinos Gkaragkounis. Despite his busy schedule, he was always available and willing to share his knowledge for solving any problem that arose. I would also like to thank all the members of PCOpt/NTUA research team who were more than willing to help, if necessary.

Lastly, I would like to thank my family whose love has formed the foundation of my personal development and my friends for always believing in me and for literally and figuratively accompanying me in each of my journeys.

Εθνικό Μετσόβιο Πολυτεχνείο
Σχολή Μηχανολόγων Μηχανικών
Τομέας Ρευστών
Μονάδα Παράλληλης Υπολογιστικής Ρευστοδυναμικής & Βελτιστοποίησης

Ανάπτυξη Λογισμικού Προσομοίωσης της Λίπανσης μεταξύ των Δαχτυλιδιών Πιστονιού/Χιτωνίου Μηχανής Εσωτερικής Καύσης

Διπλωματική Εργασία

Αλεξάνδρα-Ιωάννα Λιόση

Ακαδημαϊκός Επιβλέπων:
Κυριάκος Χ. Γιαννάκογλου, Καθηγητής ΕΜΠ

Βιομηχανικός Επιβλέπων:
Δρ. Κωνσταντίνος Γκαγκάς, Ειδικός, Toyota Motor Europe

Αθήνα 2021

Περίληψη

Για τη μείωση των απωλειών κατά τη λειτουργία μίας εμβολοφόρου Μηχανής Εσωτερικής Καύσης, το εσωτερικό του χιτωνίου υποβάλλεται σε κατεργασίες φινιρίσματος. Η διπλωματική εργασία ασχολείται με την εύρεση των χαρακτηριστικών της επιφάνειας του χιτωνίου που οδηγούν σε μειωμένες απώλειες λόγω τριβής. Ακόμη, προετοιμάζει το μεγαλύτερο μέρος των απαιτούμενων εργαλείων για τη βελτιστοποίηση με αιτιοκρατικές ή στοχαστικές μεθόδους. Αυτή η τριβολογική ανάλυση βασίζεται στη λίπανση μεταξύ του εμβόλου, των δαχτυλιδιών του και το τοίχωμα του κυλίνδρου. Επιλύονται οι εξισώσεις Navier-Stokes για τη μόνιμη, στρωτή ροή ασυμπίεστου λιπαντικού στην περιοχή όπου επικρατεί υδροδυναμική λίπανση, στο περιβάλλον του OpenFOAM. Η τραχύτητα στο εσωτερικό του χιτωνίου δημιουργείται από διαδοχικές ή διασταυρούμενες αυλακώσεις τριγωνικής διατομής και διαστάσεων σε μm. Για το λόγο αυτό, δεν προσομοιώνεται ολόκληρη η διαδρομή του εμβόλου. Οι οριακές συνθήκες για την πίεση και την ταχύτητα επιλέγονται σε μια συγκεκριμένη ταχύτητα περιστροφής και για μια συγκεκριμένη γωνία στροφάλου. Το υπολογιστικό χωρίο δημιουργείται από αλγόριθμο, στον οποίο δύναται να εισαχθούν διαφορετικές γεωμετρίες δαχτυλιδιών και ποιότητες επιφανείας. Από τις προσομοιώσεις που υλοποιήθηκαν με δειγματοληψία τιμών των μεταβλητών σχεδιασμού, προτείνεται η τελική επιφάνεια του χιτωνίου να απαρτίζεται από βαθιές αυλακώσεις, που βρίσκονται κοντά μεταξύ τους.

Επιπρόσθετα, συγκρίνονται τα αποτελέσματα μεταξύ των ροών Couette και Poiseuille για απλοποιημένες γεωμετρίες και της συχνά εφαρμοζόμενης εξίσωσης Reynolds ως προετοιμασία για την εξίσωση της μέσης ροής. Τέλος, η μελέτη επεκτείνεται με τη διατύπωση των εξισώσεων μη-μόνιμης ροής στο απόλυτο και στο κινούμενο σύστημα αναφοράς για αυτόν τον τύπο προσομοιώσεων. Μεγάλο μέρος της διπλωματικής εργασίας πραγματοποιήθηκε στις εγκαταστάσεις της Toyota Motor Europe στις Βρυξέλες, κατά τη διάρκεια εξάμηνης πρακτικής.

National Technical University of Athens
School of Mechanical Engineering
Fluids Department
Parallel CFD & Optimization Unit

Development of a Simulation Tool for the Lubrication between the Piston Rings and the Cylinder Bore of an Internal Combustion Engine

Diploma Thesis

Alexandra-Ioanna Liosi

Academic Advisor: Kyriakos C. Giannakoglou, Professor NTUA

Industrial Advisor: Dr. Konstantinos Gkagkas, Expert, Toyota Motor Europe

Athens 2021

Abstract

For decreasing power losses during the operation of a reciprocating Internal Combustion Engine, the inner cylinder wall undergoes surface finishing. This diploma thesis proposes a combination for the cylinder bore's surface characteristics, that leads to lower friction losses. Also, it prepares the ground for performing a gradient-free or gradient-based optimization, by developing a major part of the required tools. This tribological analysis is based on the lubrication between the piston, its top ring and the cylinder wall. The steady-state Navier-Stokes equations are solved for the laminar flow of an incompressible lubricant in the hydrodynamic lubrication regime, in the OpenFOAM environment. The liner's surface topography is introduced as a pattern of triangular grooves with base dimensions in μm. For this reason, the complete cylinder's stroke isn't simulated. The pressure and velocity boundary conditions are selected for a specific crank angle and rotational speed. A framework is used for quickly creating the necessary geometry files, which include different ring profiles and alternative liner features. Though an adequate sampling of the design space and evaluation on the CFD tool of the selected samples, it is proposed for the bore's surface finish to create deep grooves in close proximity. Additionally, a comparison between the results of the fundamental velocity-driven and pressure-driven flows, in fully-flooded condition, in simplified geometries and the frequently used Reynolds equation is made. Lastly, the analysis is extended by extracting the unsteady flow equations in multiple frames of reference for this kind of simulations. Major part of this work was carried out in midst a 6-month long internship, at the premises of Toyota Motor Europe in Brussels.

Acronyms

NTUA	National Technical University of Athens
ICE	Internal Combustion Engine
RMS	Root Mean Squared
TDC	Top Dead Center
BDC	Bottom Dead Center
HL	Hydrodynamic Lubrication
NS	Navier-Stokes
OEM	Original Equipment Manufacturer
CFD	Computational Fluid Dynamics
SI	Spark Ignition Engine
CI	Compression Ignition Engine
STP	Standard Temperature & Pressure conditions
PDE	Partial Differential Equation
CV	Control Volume
FVM	Finite Volume Method
BC	Boundary Condition
CAD	Computer Aided Design
CPU	Central Processing Unit
TMC	Toyota Motor Coorporation
FMEP	Friction Mean Effective Pressure
MRF	Multiple Frame of Reference

Contents

List of Figures

List of Tables

Chapter 1

Introduction

The automotive industry is developing rapidly and is regularly challenged to surpass its current best. Every year, national and global regulations on transportation become more and more strict and they set more demanding design goals to the manufacturers. These are related with the vehicle's fuel consumption, its mechanical efficiency and the pollution caused during its lifespan. As a result, hybrid vehicles and plug-in hybrid vehicles are likely to become the dominant means of transport in the future[1]. According to [2], the annual sales of non-electrified vehicles are aimed to be 4.5 million units by 2030. The same applies for Hybrid Vehicles(HEV) and Plug-in Hybrid Vehicles(PHEV), even though their annual sales were 1.4 million units only in 2016. Even though the automotive industry is shifting towards electrification, the vehicles equipped with Internal Combustion Engines(ICE) will still hold, at least, 50 % of the passenger vehicles annual sales. For this reason, further improvements are demanded on the engine's design, manufacturing techniques and incorporation to automobiles in terms of vehicle performance, passenger's comfort, decreased fuel consumption and more environmental-friendly operation.

1.1 Tribology in Developing Engineering Devices

Regardless the type of the powertrain, numerical and experimental studies are conducted for minimizing energy losses and increasing the operation cycles of its compartments. In the drivetrains, notably, the developed friction in rotating or moving parts, the force magnitudes applied at each component and the thermal transport phenomena hold great importance during those researches. These phenomena are included and described quantitatively by the science of Tribology[3]. In short, this is the science of interacting surfaces in relative motion. It includes the study and application of the principles of friction, lubrication, and wear. It is highly inter-

disciplinary, since it employs many academic fields, including physics, chemistry, materials science, mathematics, biology, and engineering.

The majority of engineering applications include two, or more, mechanical components moving relative to each other, either in translational or rotational motion. Each time, the selected machine elements under investigation form a tribo-system. The study of the relative motion's impact over the surfaces of the mechanical components, in terms of friction and wear, is a fundamental part of the tribological analysis[4]. In more detail, friction is the resistance force opposing to the mechanical components' relative motion, while generating heat between those two. Consequently, it causes wear on the solid surfaces of either one or both of the components' material. To reduce friction and wear at interface, a lubricant is supplied.

Within the current thesis' context, attention is primarily given to the resistance force, which is developed between solid-solid, or solid-liquid interfaces of sliding components. An additional performance metric for the vertical dynamics of the examined pair of surfaces, is the load carrying capacity. For plenty of engineering applications, the friction is aimed to be minimized, while the load-carrying capacity of the investigated contact is held constant, or increased. Therefore, those objectives can be satisfied with insightful mechanical design, that reinforces the lubrication effectiveness.

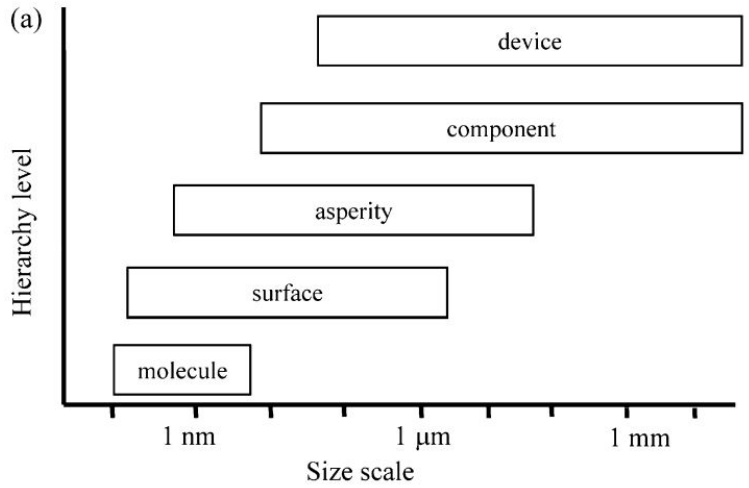

Figure 1.1: *Hierarchy levels introduced by different scales on machine micro-devices*

The development of an engineering device is a cyclic process which can be roughly decomposed in design, simulation and experimental validation. Those steps are sequentially repeated until the design goals are satisfied. At the design stage, the device's geometry is defined. Normally, the dimensions of most machine elements, or micro-devices, are expressed in mm, or μm, they are observable without the assistance of additional tooling and belong to the macroscale. Next, the device's surface features, which are related with geometry and roughness, are determined.

The surface topography is generally expressed in magnitudes from 1 nm to 1 μm, thus belongs to the mesoscale. Then, the manufacturing and assembling methods are selected. It is common to investigate the interaction of raw materials' molecules under different conditions(temperature, pressure, etc.) and with different additives, in order to choose the manufacturing techniques and coatings, that enhance materials' properties. Tribological analyses are performed in every stage of product development and are adapted to the required scale, or hierarchy level[5].

1.2 Surface Topography

Almost, all engineering devices undergo surface finishing in order to increase their wear resistance, or resistance to other deteriorative mechanisms, enhance their mechanical properties and acquire specific roughness and tolerances that assist in their assembly. Most importantly, their resistance to external loads is increased and the developed friction can be controlled according to the surface roughness. The applied friction is restrained by effective lubrication. The oil's flow and the lubricating film thickness upon the moving surfaces is affected by their roughness, especially by the locations of their asperities (high points/heels) or valleys (low points), their density and their distribution across each surface. All solid surfaces are found to be uneven, when they are examined on sufficiently fine level. At the molecular, or atomic level, even the smoothest surfaces have irregular profiles. For instance, the roughness of manufactured surfaces is usually between $[0.1 - 10]\mu$m, whereas typical atomic diameters are between $[0.0001 - 0.001]\mu$m[6].

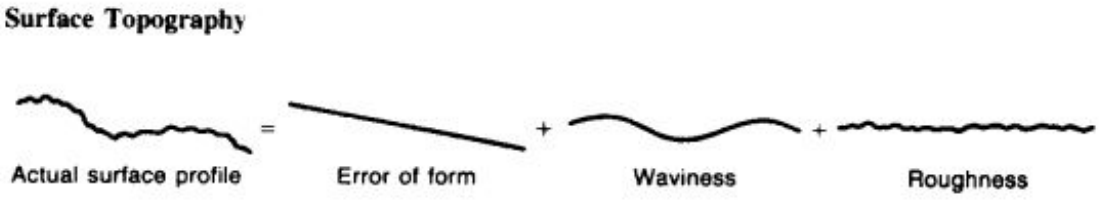

Figure 1.2: *Surface topography of machined surfaces*

Each manufacturing process used on engineering components, leaves characteristics marks on their surface, referred to as *surface topography*, or *surface texturing*. These features are presented in Figure 1.2 and can be divided into three main categories[7]. Therefore, every machined surface can be described by one, or, usually, a combination of those characteristics.

- ***Error of form***, where the surface deviates from its designed shape or prominent directional machining marks are made, because of manufacturing errors, such as wrong tool positioning etc.

- ***Waviness***, where relatively long waves are found in the surface profile due to tool vibration, unwanted machine/work deflection etc.
- ***Roughness***, excluding the previous two, refers to irregularities inherent in the production process left by the machining agent, e.g. tool tip, grit, spark.

1.2.1 Measurement of Surface Topography

Various methods[8] for determining the texturing characteristics of any machined surface can be employed, depending on the required level of resolution. They are broken down into two main categories. The first group is based on contact measurements and are the most widely used methods. Some of them use the contact of a fine stylus, while others depend on electrical, or thermal measurements over an area. Alternatively, a fluid can be poured between the surface of interest and an opposing plane. For this pair, the fluid's flow is observed, in order to illustrate the surface's topography. The second category is associated with different optical methods. In this case, the most common practise is to examine the surface by electron, or light microscopy. The surface topography is represented by a dataset of height, or heading, measurements z along with the coordinates of their position on the surface, regardless the measuring method. It is resolved accurately, providing that the distance between neighbouring measurement points is adequately lower than the size of its features.

Stylus profilometry measurements

In stylus profilometry, the roughness height measurements are made by interactions with a probe. In detail, a fine stylus is moved with constant velocity, across the examined surface, by an actuator. Also, the actuation system is responsible for measuring the lateral and longitudinal position of the stylus, while its vertical position is monitored via a transducer. The individual, parallel, linear profiles can be superimposed and generate an areal roughness profile. However, the surface roughness is smoothed by the shape of the stylus, as shown in Figure 1.3, because its tip is unable to penetrate fully into deep narrow surface features. Attention must be given, when dealing with very compliant, or fragile surfaces because, even though the load applied by the stylus is small, it may cause sufficient local stress to distort, or damage the surface. For this type of surfaces, non-contacting, optical methods of surface measurement are used.

Non-contacting optical methods

The dominant, non-contacting methods for determining surface texturing are interferometry, and optical focus. In both cases, the whole surface is examined, in order to detect its texturing on a pixel-by-pixel basis, using image processing algo-

rithms. Compared to stylus profilometry, optical methods have greater resolution, because they are microscope-based. Furthermore, larger areas can be analysed at high resolution by stitching together data from separate measurement areas. Lastly, attention should be given and additional actions are taken, when dealing with transparent, or translucent surfaces.

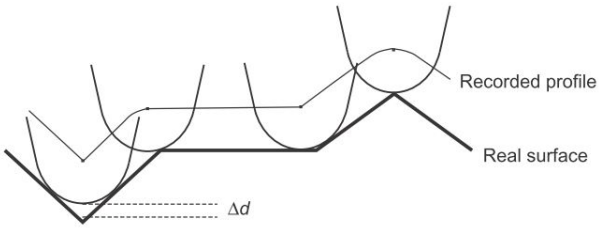

Figure 1.3: *Difference between the actual and the measured surface profile using stylus profilometry*

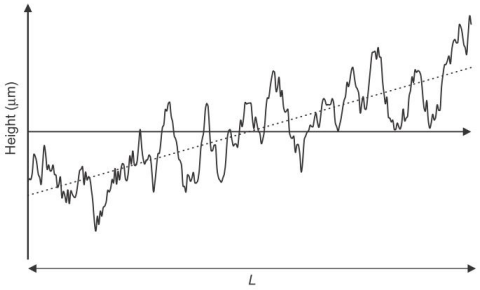

Figure 1.4: *Best linear fit(dashed line) for a measured surface profile*

1.2.2 Quantifying Surface Topography

Aside from obtaining a visual representation of the machined surface's topography, it is important to extract useful information concerning its characteristics. Standardized magnitudes are calculated based on in-line, or areal texturing readings, in order to quantify the examined surface's error of form, waviness and roughness. The most common method for describing them quantitatively is formed upon in-line readings and the most widely used profile parameter is the average roughness, R_a. It is defined[8] as the arithmetic mean deviation, $|z|$, of the surface's height measurements from the profile's mean line and is shown in eq. 1.1

$$R_a = \frac{1}{L}\int_0^L |z(x)|\,dx = \frac{1}{N}\sum_{n=1}^{N} |z_n| \tag{1.1}$$

where z is the height measurement of the surface roughness, L is the sampling length of the examined surface and N is the number of dataset points. The mean line for a profile dataset is shown in Figure 1.4 and is found as the best linear fit of the dataset with equal areas of the profile lying above and below it.

Another important profile parameter is the Root Mean Squared (r.m.s.) value, R_q, which is defined[8] as the root mean square deviation of the profile from the mean line, as shown below

$$R_q = \sqrt{\frac{1}{L}\int_0^L z^2(x)\,dx} = \sqrt{\frac{1}{N}\sum_{n=1}^{N} |z_n^2|} \tag{1.2}$$

Many surfaces may have similar R_a and R_q values and in case that their texturing follows a Gaussian distribution, it is known that $R_q = 1.25R_a$. Even though these profile parameters are useful in describing quantitatively the surface topography, they don't provide any further information on the shapes, or the spacing of the surface's irregularities. For this reason additional profile parameters[8], or alternative methods[9], [10], [11] can be employed, in order to represent more accurately the surface's features. In this diploma thesis, a more complex method is adopted for expressing the surface topography of the cylinder bore, which is described in Section 1.3.4.

1.3 Friction in the Internal Combustion Engine

1.3.1 Description of the Engine's Operation

In a reciprocating engine, each piston is moving back and forth inside the cylinder and transmits power from the high-pressure and temperature burned-gases inside the combustion chamber through the piston, its connecting rod and the crank mechanism to the drive shaft[12]. The rotational motion of the crank-shaft is converted to a rectilinear, periodic motion for the piston. The majority of reciprocating engines operate on a four-stroke cycle, which require two crank-shaft revolutions for delivering the necessary power and for preparing their cylinders for the next cycle. Alternatively, two-stroke cycle engines can be used in order to obtain higher power output with simpler valve design but limited engine size. Within the thesis context, attention is given to the four-stroke engines due to the available experimental data. However, the followed methodology and the developed tools are applicable in both cases. The operation cycle of a four-stroke engine is shown in Figure 1.5 and is composed by the intake, the compression, the power and the exhaust stroke. Each stroke refers to the distance travelled by the piston from the Top Dead Center(TDC) which is the highest point of the cylinder, to the Bottom Dead Center(BDC) which is the lowest point of the cylinder, or in reverse.

- ***Intake Stroke:*** The cycle starts with the intake stroke, where the piston is positioned at the TDC. Fresh air, or fuel-air mixture is drawn into the cylinder, until the piston reaches the BDC. The air is inducted by the inlet valve, which opens shortly before the stroke starts and closes after it ends.
- ***Compression Stroke:*** When the piston is at the BDC for the first time, the compression stroke starts and the mixture inside the cylinder is compressed to a small fraction of its initial volume. Combustion is triggered and the cylinder pressure rises rapidly, when the piston is close to the TDC.
- ***Power Stroke or Expansion Stroke:*** The piston is at the TDC and is moving towards the BDC, because it is pushed down by the high-temperature,

high-pressure gases. Its motion drives the crankshaft to rotate and is transmitted as power to the drive-shaft. The expansion work is normally five times greater than the compression work. Towards the end of the expansion stroke, the exhaust valve opens, in order to decrease the in-cylinder pressure close to the exhaust system's pressure.

- ***Exhaust Stroke:*** The exhaust valve is open and since the pressure inside the cylinder is greater than the ambient pressure, the exhaust gases are exiting the cylinder. Simultaneously, the piston moves from BDC to TDC and pushes the remaining burned gases outside of the cylinder. Near the TDC, the exhaust valve closes and the inlet valve opens in order for the cycle to start again.

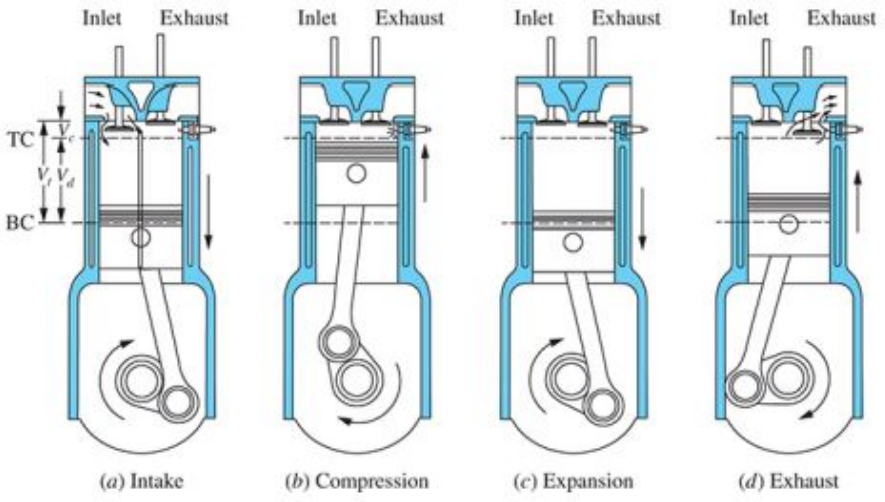

Figure 1.5: *The operating cycle of a four-stroke engine cylinder[12]. V_c, V_d and V_t indicate clearance, displaced, and total cylinder volumes.*

1.3.2 Friction Losses

Strict legislation regarding environmental pollution demands from the IC engine manufacturers to produce power units with improved fuel economy. By applying this measure, the pollutants' decrease can be justified by considering the equilibrium of mass inside the engine cylinder, where the fuel's mass combined with the needed air for combustion is, roughly, equal to the pollutant's mass. Therefore, with lesser fuel, the necessary air for combustion will be decreased too, leading to fewer pollutants. Furthermore, the competitiveness of the reciprocating engine against electrical power unit can be enhanced with decreased fuel consumption due to even lesser expenses for gas, or oil.

Improvement in fuel economy is achieved by increasing the engine's efficiency. Considering that it is aimed to decrease the fuel intake, the output power remains constant as long as power loss due to friction is decreased. It is evident, that

the cylinder's usable power, which is delivered to the drive-shaft(effective work) is lower than the work provided by the high-pressure, high-temperature gases inside the combustion chamber(indicated work). The difference between the effective and indicated work is called friction work[12]

$$Friction\,Work = (Indicated\,Work) - (Effective\,Work) \tag{1.3}$$

and is dissipated within the engine and its auxiliaries with various ways. It is a sufficiently large fraction of the indicated work and is dependent on the engine's load and rotational speed. For instance, it is 10% of the indicated work at full load and lower speeds, but it reaches percentages up to 50% at light load, or to 100% at idle or no-load.

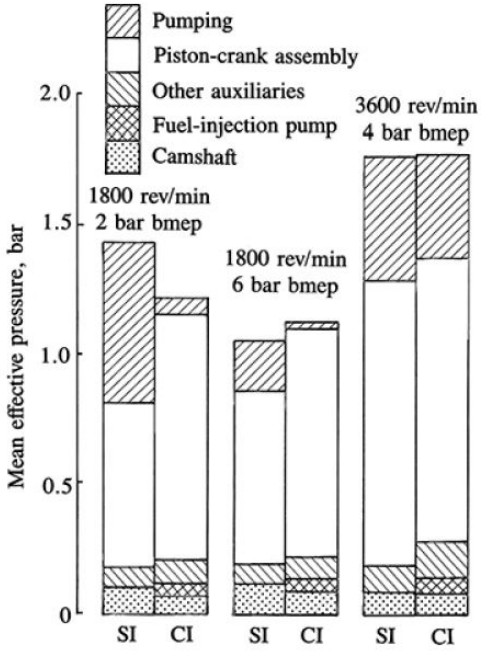

Figure 1.6: *Major categories of friction work, expressed as mean effective pressure values at different loads and speeds[12]. SI: Gasoline engines, CI: Diesel engines*

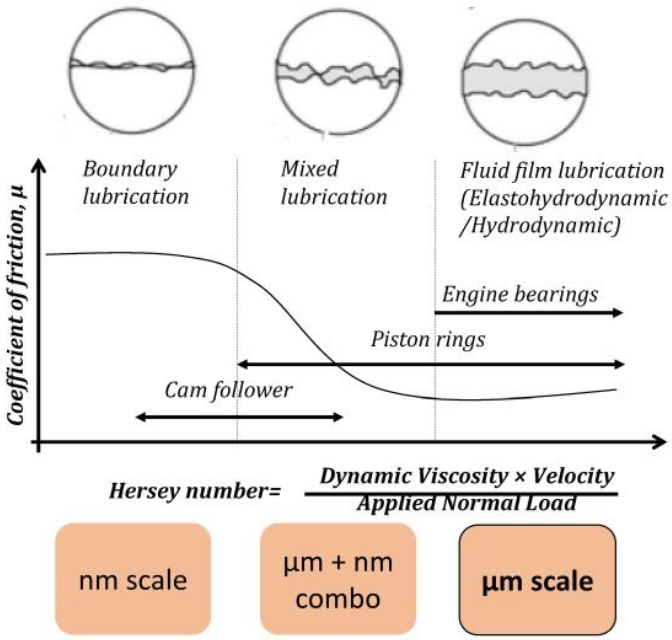

Figure 1.7: *Stribeck curve across different scales for different engine components*

Friction work expresses power losses due to the forces opposing the relative motion between the moving parts of the engine. Also, it includes the pumping work under which the fresh mixture enters the cylinder through the intake system and the burned gases exit the cylinder through the exhaust system. Moreover, it contains the needed power for driving important engine accessories such as pumps, the fan etc. In Figure 1.6, the relative importance of the friction work's components, is illustrated. Typical ranges are crankshaft's friction losses from 10 to 15%, losses of reciprocating parts from 25 to 30%, camshafts' losses from 10 to 15%, auxiliaries from 10 to 15%, and

total pumping work[1] from 30 to 45%[12]. From this figure, it is apparent that in all cases, the friction losses of the piston assembly hold the greatest percentages. For this reason, this thesis focuses on proposing solutions for decreasing the resistance forces which are applied to the piston assembly. Even though total pumping work is comparable to the piston assembly losses, it isn't taken under consideration. It is excluded from this study, because pumping work is affected by the detailed design and functioning of each individual pump which falls outside the scope of this thesis.

1.3.3 Lubrication

The friction opposing the relative motion between two engine components is decreased by applying a lubricant between them. The resistance force is mainly dependent on the vertical load applied to each surface, the relative velocity of the pair, the lubricant's properties and the interacting surfaces' topography. During an engine cycle, the vertical load and the pair's relative velocity vary in a great manner, hence the developed friction is changing accordingly and different features of lubrication are encountered at each piston position. In general, the types of lubrication are divided into three major categories which are presented in Figure 1.7:

1. ***Boundary lubrication***, where the oil film thickness is very thin and cannot prevent contact between the solid surfaces. Hence, asperity interaction occurs. Since, the load is supported by the surface roughness, where the contact area is very small, high friction is developed. Its magnitude is mostly determined by the surfaces' properties.

2. ***Mixed lubrication***, where a thin oil film is present between the surfaces. It is the transition regime from boundary to hydrodynamic lubrication. Consequently, partial asperity interaction exists and the developed friction is reliant on the surfaces' and the lubricant's properties.

3. ***Hydrodynamic lubrication***, where both surfaces are separated by a film of liquid, or gaseous lubricant. For this reason, the friction is equal to the viscous forces opposing the oil's flow and there is no interaction between the surfaces' asperities. The vertical load is supported by the oil film. This type of lubrication is, usually, met between conformal shapes.

An alternative type of HL is ***Elasto-Hydrodynamic lubrication***. It describes the lubrication regime, where sufficiently large pressures cause elastic deformation to the lubricated surfaces. It is dependent on the material properties of the interacting surfaces, such as roughness, hardness, elasticity plasticity, shearing strength, thermal conductivity and wettability with respect to the lubricant and it is found among non-conformal surfaces.

[1]Total pumping work includes the power needed for the operation of the oil pump, fuel pump, water pump and air pump, if used for emission control.

Several methods are available for identifying the lubrication regime for the investigated engine subsystem. The most prevailing method uses the Stribeck curve, as shown in Figure 1.7, where the dominant lubrication parameters are combined. Particularly, the dependent variable is the friction coefficient μ, which is the fraction of the friction force divided by the vertical load, that is applied to the surface. In this figure, the variation of μ is depicted, as the Hersey number is increasing. The Hersey number is defined by

$$Hersey\ Number = \frac{Viscocity \cdot Velocity}{Unit\ Normal\ Load} \tag{1.4}$$

and is a dimensionless magnitude.

It is clear that for low velocities, the friction coefficient is very high and its magnitude is independent of the pair's velocity, as it remains almost constant in the boundary lubrication regime. This type of lubrication occurs between engine parts during starting and stopping, at the piston ring and cylinder interface in stroke reversals, between heavily loaded parts etc.[12]. As the velocity increases, the friction coefficient decreases in a linear manner. In the mixed lubrication regime, features of the boundary and hydrodynamic lubrication coexist and are usually caused by abrupt load or speed variation or mechanical vibration. On the other hand, in the HL regime, the coefficient of friction rises in a linear way with the velocity increase. This is justified by the viscous nature of the developed friction and its growing dependence from the lubricant's properties. This type of lubrication is encountered in engine bearings, between piston skirt and cylinder liner, between piston rings and cylinder liner for high sliding velocities.

Motor oils are essential for the normal operation and the lifespan of ICEs, because they are responsible for reducing friction and wear between lubricated surfaces. Also, they can assist in cooling of the engine block and its components, in forming seals between piston to rings and rings to cylinder walls, in surface cleaning and in preventing corrosion. They can be mineral oils, synthetic oils or solid lubricants, like grease, depending on the engine subsystem, that are applied. The most important properties for describing a lubricant are the viscosity and the viscosity index. The first one expresses the resistance of the oil molecules to external shear stresses. The viscosity index indicates the variation of viscosity with changes in temperature. Lower viscosity variation with temperature is achieved by lubricants with high level of viscosity index.

1.3.4 Lubrication in Piston Ring-Pack

The piston assembly is consisted of the piston and the piston skirt, the ring-pack which includes 2-4 compression rings, 0-3 oil control rings and possibly scraper rings, the piston pin and the connecting rod as shown in Figure 1.8. Within the thesis

context, focus is given at the interaction of the piston and its ring-pack with the cylinder liner. The compression rings are responsible for preventing the exhaust gases from transferring to the crankcase. The oil control rings are distributing evenly the available lubricant and the dissipated heat along the cylinder wall and are scrapping off the excessive oil back to the crankcase during downstroke. Scraper rings assist in both functions of sealing the combustion chamber and spreading the lubricant. Lastly, the ring-pack is stabilizing the piston, in order to avoid contact with the cylinder liner, especially during cold starts.

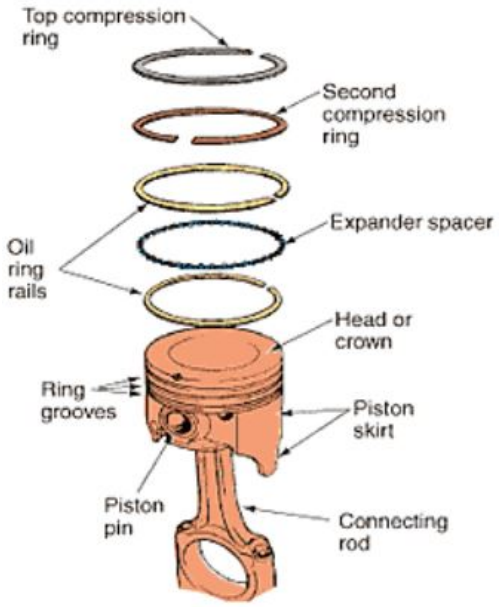

Figure 1.8: *The piston-ring assembly*

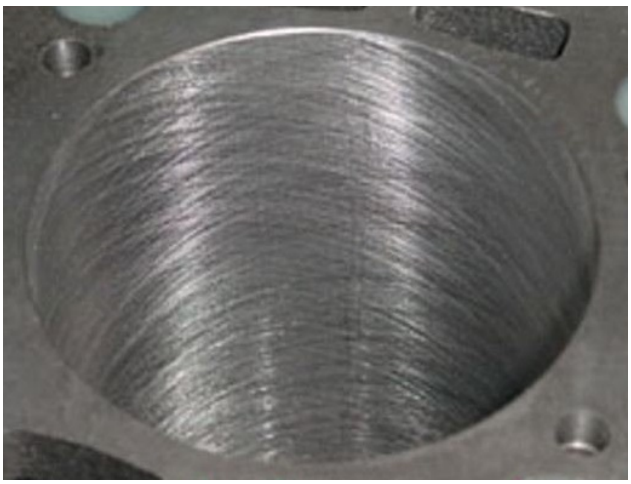

Figure 1.9: *The result of honing on the cylinder liner surface*

It is a common practise to use honing as a surface finishing process for the cylinder liner. Honing[13] is an abrasive machining process, that is used for producing high-precision machine elements, in terms of geometric form, or improves surface finish. It is performed by scrubbing a grinding stone, or wheel against the surface of the machine element along a controlled path, where specific, precise shapes are required such as inside tubes, holes and outside of bores. It was established for the cylinder liner, because the formed grooves(long, narrow cuts) as shown in Figure 1.9, which are deeper compared to initial surface roughness, assist in decreasing oil consumption, in increasing its durability and in enhancing its wear resistance[14]. In the same figure, it is observed that the grooves are intersecting with each other. This pattern is called cross-hatch and is aiding in ensuring effective lubrication and combustion chamber sealing, because the intersection points serve as oil reservoirs.

The surface topography of the cylinder liner, here is described by four parameters, namely the groove pitch, the hatch-angle, the groove width and the groove depth as shown in Figure 1.10. The groove pitch expresses the distance between two consecutive grooves at any section which is defined by two intersection points.

The hatch-angle represents the angle between two intersecting grooves towards the longitudinal direction. In this diploma thesis, the groove's cross-section is taken as triangular, even though in reality it can have circular, barrel, or more complex shapes, depending on the available machining processes. Therefore, the groove depth declares the triangle's height, or how deep the groove is penetrating inside the cylinder liner. The groove width is referring to the triangle's base, or, for a singular groove to the distance between its edges normal to the lengthwise direction, on the shame plane. This method was selected, because the average roughness R_a and the r.m.s magnitude of roughness R_q don't provide any useful information regarding the groove's shape, orientation and positioning across the wall. The inner cylinder wall is not covered entirely by grooves, so the remaining areas, named as plateau, have non-directional roughness. This is not taken under account, in order to simplify the cylinder liner's topography.

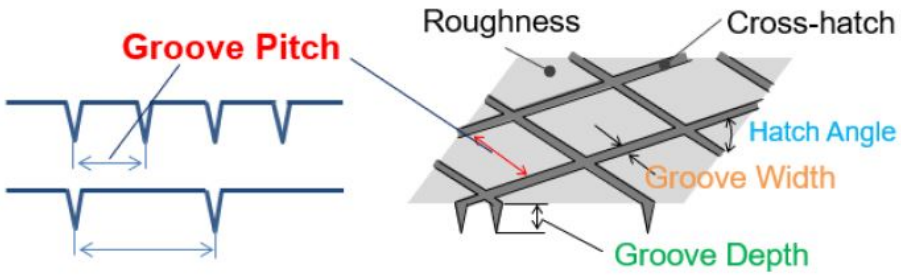

Figure 1.10: *Describing the surface topography of the cylinder liner*

The smooth functioning of the ring-pack is achieved by forming the necessary conditions for the lubricant's flow between the rings and the liner. Especially for the compression rings, a thick oil film thickness is essential during the expansion stroke for stalling the exhaust gases from leaking to the crankcase. During the engine's operation, regulated oil supply to be distributed along the cylinder wall, is crucial for reducing the friction applied at the reciprocating piston. Also, oil-starvation must be avoided for ensuring load support from the formed film thickness and for preventing metal-to-metal contact of the piston and its rings with the liner. All these rely upon the geometry of the rings, the surface topography of the liner, the lubricant's properties, the pressure conditions inside the cylinder and the piston's velocity.

The first purpose of this thesis is to develop a CFD model for the lubrication between the piston rings and the cylinder liner, that considers all the aspects mentioned above and provides useful information regarding the applied forces. The performance of this tribo-system is examined based on different surface features for the cylinder liner. After the investigation is completed, a combination of the groove characteristics that leads to reduced friction, is proposed for the cylinder liner. This way, instead of conducting experiments for measuring the friction which is applied at the piston for every alternative of the liner surface features, it is possible to test only

the most promising options that are proposed by this computational model. It is a measure for assisting in the design of actual experiments and the overall product development of an engine, in order to save time and resources. Then, the developed model is compared with the most commonly used method in the automotive industry and their advantages and disadvantages are discussed. Lastly, a more complex method is investigated, that would be useful in understanding the perplexing phenomena of transient lubrication inside the engine cylinder.

1.4 Thesis Outline

Following this introduction, the five chapters composing this thesis are presented:

- Chapter 2: Since the features of the cylinder liner are expressed in μm, the validity of the continuum approach is checked for the lubricant's flow. Its flow equations are described, while attention is given to the analytical solutions of the fundamental fluid flows. The computational method used for solving the oil's flow field is described, accompanied with the performance indicators for assessing the lubrication effectiveness.
- Chapter 3: The aspects of the physical problem are clarified and the geometry of the computational domain, along with proper boundary conditions are presented. Before proceeding with the simulations, the results of the mesh sensitivity analysis are demonstrated for a reference case. Next, the flow-fields and the lubrication performance for a sample of the design space are found and the influence of the liner's surface characteristics is exhibited.
- Chapter 4: The frequently used method which is based on the Reynolds equation is described. A comparison is held between the developed model and the Reynolds equation for a simplified geometry. The benefits and the limitations for each method are discussed.
- Chapter 5: Considering the transient nature of the lubrication inside the internal combustion engine, the flow equations are extracted for the unsteady flow of the lubricant in multiple frames of reference, in order to account for the relative motion between the piston and the cylinder wall.
- Chapter 6: This work is summarised and conclusions are drawn, based on which proposals for future work are formed.

Chapter 2

Formulation of the Physical Problem

2.1 Introduction

In this chapter, the applicability of continuum mechanics is investigated, because the surface characteristics of the cylinder liner belong to the meso-scale. Once it is verified that the lubricant can be considered as a continuum substance, the fundamentals of fluid mechanics are briefly described. Attention is paid to a specific set of analytical solutions for the conservation of a fluid's mass and momentum, namely the Couette and the Poiseuille flows. These two serve as the foundation of most proposals for modelling the lubrication problem. The method for transforming the governing PDEs of the lubricant's flow into a set of linearized algebraic equations is presented on hexagonal grids, using the Finite Volume Method. This linear system of equations is solved by the SIMPLE algorithm[15]. Lastly, the metrics, which are used to quantify the lubrication performance, are demonstrated and further explained. These values are of out-most importance for the developed model, because its validity, usefulness and ability to be implemented in the industrial processes are dependent on those results.

2.2 Continuum Approach

Before proceeding with the fundamentals of fluid dynamics in the macro-scale, it is essential to investigate their applicability to the current micro-fluidics problem.

All the substances found in nature exist either in solid, liquid, or gaseous forms or states, depending on the pressure and temperature conditions. Each of these states has a specific molecular structure, allows certain movements of atoms and behaves very differently to external stresses. During analytical, or numerical modelling, each phase is represented by a control volume, which is restricted by either its physical boundaries for the solid form, or the occupied volume (such as a vessel or containers) for the fluid/gaseous form.

It is important to determine a constitutive control volume of suitable size (usually in the range of several μm edge length, assuming that the CV is represented by a rectangle), in order to investigate the behaviour of a liquid under specific conditions. The sufficiency of the CV' size comes from the number of singular atoms, that can be contained and whether it is large enough for averaging all the effects exerted by those atoms. The purpose of averaging the individual atom's impact is to extract a uniform influence to the fluid. Consequently, the fluid is treated as being a continuous piece of matter, which is why this approach is referred to as the continuum approach or the continuum hypothesis[16]. This influence-averaging is favourable for both analytical/numerical and experimental studies. For the first case, it usually results in a significantly more predictable behaviour for the continuum, while for the second case, it gives rise to more steady experimental data. Especially for fluids, these can be treated as having average values for velocity, acceleration, entropy or enthalpy and other magnitudes, which are derived by them. However, these are averaged values, so they are discontinuous when looking at the atomic scale.

With the purpose of identifying a fluid as a continuum substance, or not, its CV dimensions are selected, based on the required level of detail. Then, the number of molecules contained in this CV is calculated and is checked whether it is greater or lower than a threshold value. If it is greater, then the fluid is modelled as a continuous piece of matter and the laws of classical physics describe its flow field. If it is lower, then the fluid's behaviour should be modelled in smaller scales, for example at the molecular level, or lower. For most macro-scale and micro-fluidic applications, this threshold value is 10 000 atoms. After a fluid is characterized as continuous substance, it can be broken down to smaller CVs, each of which has distinct values of the field variables and represent the cells of the computational domain.

The needed steps for the lubrication problem are presented, in detail, for characterizing the lubricant as a continuous substance. First, the greatest level of detail is limited to $0.1\mu m$ for the current application. For this reason, it is necessary to investigate if the laws of continuum physics are applicable to this problem. Secondly, the oil's properties are needed, namely its density ρ and molecular weight M_r, which is defined as shown in equation 2.1 by the fraction of the oil's mass m divided by its number of moles n,

$$M_r = \frac{m}{n} \tag{2.1}$$

Even though, the pressure and temperature conditions inside the cylinder vary with time, the oil's density is taken at STP conditions as $\rho = 841.4\frac{kg}{m^3}$ for computing the unit volume of one molecule, using the Avogadro constant. Unfortunately, the oil's composition is unknown, therefore its molecular weight is calculated as the average value of the molecular weights' range for volatile oils[17], that is $M_r = 0.0565\frac{kg}{m^3}$. Hence, 1 mole of substance weighs 0.0565 kg and given that density is defined by the fraction of mass divided by its volume, $\rho = \frac{m}{V}$, it is possible to calculate the volume V_{1mole} that corresponds to 1 mole of lubricant. For this case, it is found as $V_{1mole} = 6.715 \cdot 10^{-5}\ m^3$. It is known that 1 mole of substance contains $6.022 \cdot 10^{23}$ molecules. Therefore, the volume occupied by 1 molecule of substance is found as

$$V_{1molecule} = \frac{V_{1mole}}{6.022 \cdot 10^{23}} \tag{2.2}$$

Next, based on the intended level of detail, a square control volume is selected with side length of 0.1 μm and is examined how many molecules of lubricant fit into this CV. It is found that $8.968 \cdot 10^6$ molecules of oil are contained inside this certain CV. It is observed that the number of calculated molecules is greater than the threshold value of 10 000 and therefore, the continuum approach is valid for the engine lubrication problem.

2.3 Theory of Fluid Dynamics

The behaviour of a fluid flow is described by its physical properties, which originate from the field variables. These magnitudes are either scalar or vectors. The scalar field variables are pressure p, density ρ and temperature T, while there is only one vector variable, velocity $\mathbf{u}^1 = (u_x, u_y, u_z) = (u, v, w)$. These magnitudes follow the governing equations of continuum mechanics, namely the conservation of mass, momentum and energy. Before proceeding with the analytical form of the conservation laws, or the Navier-Stokes equations, it is important to clarify two major simplifications applied to the lubrication modelling.

Firstly, no compressibility effects are taken into account, therefore the lubricant is taken as an incompressible fluid and its density remains constant. Secondly, the temporal variation of temperature inside the combustion chamber is not taken into account and heat transfer is not modelled, thus solving the conservation of energy to acquire the temperature field is not performed. The first simplification is valid, because it has been shown after experimental testing, that the oil's density has a small variation with temperature, as long as the temperature is above 60^oC. The same applies to the oil's viscosity change with temperature. The average cylinder wall temperature was measured during the same series of tests in different engine

[1]For visualization purposes, throughout this text all vectors are presented in bold font

rotational speeds and on several stroke positions. It was observed that its magnitude was beyond the baseline value of 60^oC in each engine speed and stroke position. Hence, the viscosity of the selected lubricant is $5.10\frac{mm^2}{s}$ and is assumed constant during the engine operation.

2.3.1 Conservation of Mass

The continuity equation is expressing the equilibrium between the mass-flow that enters and/or exits a finite control volume(CV) with the temporal variation of the mass inside it. For an incompressible fluid the density does not vary with time, therefore the temporal derivate of density is zero, $\frac{\partial \rho}{\partial t} = 0$ and the continuity equation is expressed as shown below

$$\nabla \mathbf{u} = 0 \Leftrightarrow \frac{\partial u}{\partial x} + \frac{\partial v}{\partial y} + \frac{\partial w}{\partial z} = 0 \Rightarrow R^p = \frac{\partial u_i}{\partial x_i} = 0 \tag{2.3}$$

where R^p refers to the residual of the continuity equation and the index i=1, 2, 3 corresponds to each magnitude in the x, y, z direction in the same order.

2.3.2 Conservation of Momentum

The Navier-Stokes equations is a system of PDEs, one for each direction of motion at the cartesian coordinate system, that expresses the second Newton's law. They indicate that the sum of a fluid's momentum temporal variation and the momentum that enters/exits the investigated space of the flow-field is equal to the external forces applied to it. The momentum equation[18] is expressed for an incompressible fluid in an unsteady, laminar flow,

$$\frac{\partial \mathbf{J}}{\partial t} + \mathbf{S} = \sum_{i=1}^{n} F_i \Leftrightarrow R_i^u = \frac{\partial u_i}{\partial t} + u_j \frac{\partial u_i}{\partial x_j} - \frac{\partial}{\partial x_j}[\nu(\frac{\partial u_i}{\partial x_j} + \frac{\partial u_j}{\partial x_i})] + \frac{\partial p}{\partial x_i} \tag{2.4}$$

where $\mathbf{J}$ is the momentum of the fluid inside the designated space, $\mathbf{S}$ is the flow of momentum towards inside and outside its limits, $\sum_{i=1}^{n} F_i$ is the sum of external forces applied at it, R_i^u is the residual of the momentum equation and ν is the kinematic viscosity of the fluid. In this form, the symbol p represents the fraction of pressure divided by the density of the fluid $p = \frac{Pressure}{Density}$ in $\frac{m^2}{s^2}$.

2.3.3 Fundamental Fluid Flows

The set of NS equations for steady, laminar flow of an incompressible fluid under specific boundary conditions have analytical solutions for the velocity field, depending

on the pressure difference between the inlet and the outlet of the domain. Special focus is given at the flow between two parallel flat-plates, because this pair resembles, or is a piece of the most geometries found at lubrication systems. Two flow scenarios are presented in further detail, because they are used for simplifying the equations that govern the lubrication problem. For both cases, a fluid with a uniform velocity profile enters the space between two smooth flat-plates.

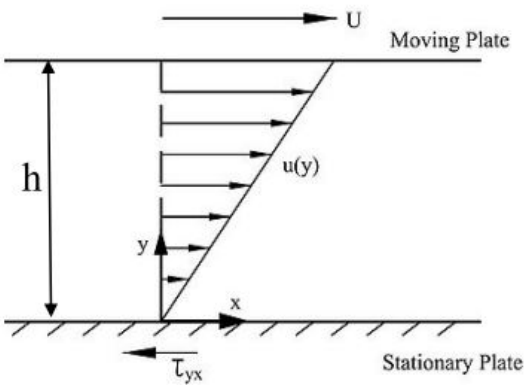

Figure 2.1: *Couette flow*

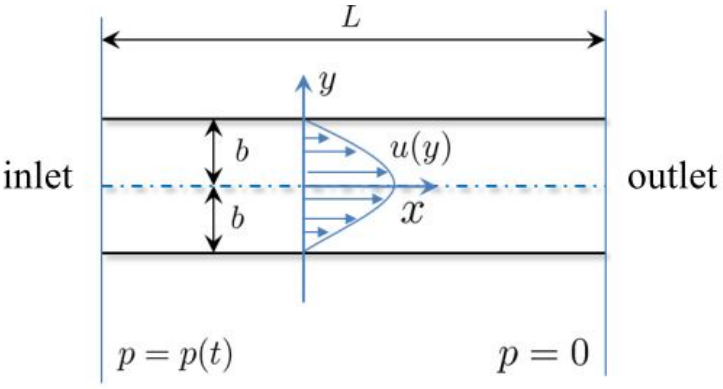

Figure 2.2: *Poiseuille flow*

For the first type of flow, namely Couette, usually, the bottom plate is stationary and the top plate is moving with a constant velocity $\mathbf{V} = (U, 0, 0)$ in parallel with the horizontal axis of motion. Moreover, the inlet and the outlet of the domain have the same pressure. Consequently, the fluid is driven towards the outlet of the domain due to the viscous forces applied at it, by dint of the moving plate's horizontal motion. The remaining boundary conditions are formed at the walls by applying Dirichlet BC for the velocity components equal to the walls' velocity and Neumann BC for the pressure equal to zero. The solution of this fully-defined problem is a uniform pressure field inside the domain and a linear relationship between the velocity and the vertical position on the cross-section, constant towards the axis motion, given by equation

$$\mathbf{u} = (u_x, u_y, u_z) = (\frac{U}{h}y, 0, 0) \tag{2.5}$$

where h is the distance between the parallel, flat-plates and y is the position on the vertical axis. The volumetric flow for a 3-D domain is found as

$$Q_{Couette} = depth \cdot \int_{y=0}^{y=h} \frac{U}{h} y \, dy = depth \cdot U\frac{h}{2} \tag{2.6}$$

For the second type of flow, namely Poiseuille, the pair of plates is stationary, but the pressure at the inlet is different from the pressure at the outlet. Therefore, this pressure difference drives the flow towards the side with the lowest pressure. The same boundary conditions apply as at Couette flow. The resultant pressure

field is constant at each cross-section and decreases in a linear manner according to fluid's direction of motion. The velocity profile has a parabolic relationship with the vertical position on the cross-section and is independent of the position over the horizontal axis,

$$\mathbf{u} = (u_x, u_y, u_z) = (\frac{1}{2\mu}\frac{dp}{dx}(y^2 - \frac{h^2}{4}), 0, 0) \tag{2.7}$$

where $\frac{dp}{dx}$ is the pressure difference between the inlet and the outlet of the domain and $\mu = \nu\rho$ is the dynamic viscosity of the fluid. The volumetric flow is calculated by

$$Q_{Poiseuille} = depth \cdot \int_{y=0}^{y=h} \frac{1}{2\mu}\frac{dp}{dx}(y^2 - \frac{h^2}{4})\, dy = depth \cdot \frac{1}{12\mu}\frac{dp}{dx}h^3 \tag{2.8}$$

2.4 Numerical Solution of the Governing Equations

The equations of the conservation laws are not always solved analytically. This applies to the governing equations for the lubrication problem at hand and for that reason the velocity and pressure fields are obtained using numerical methods. In this thesis, the Finite Volume Method[19] is implemented on hybrid grids for transforming the Navier-Stokes equations into a system of linearized algebraic equations. Then, the discretized equations are solved using the SIMPLE[15] algorithm. The field variables are stored at the elements' centres, since a cell-centered approach is adopted.

In this section, the steps for discretizing and solving the NS equations, are demonstrated for the steady flow of an incompressible fluid. The discretization process initiates by integrating the momentum equation over the volume of a grid's element a.k.a. finite volume. The momentum equation is comprised of the convection term, the diffusion term, the pressure term and explicitly defined source terms, if they are present. The volume integral of the convection and the diffusion terms are converted into surface integrals using the divergence theorem. After the transformation, by using interpolation and extrapolation schemes, a system of equations with unknowns at cell centres arise. The remaining terms are discretized utilizing numerical integration techniques and result into the final system of algebraic equations. The selected approximations affect the accuracy and the robustness of the resultant, numerical description of the flow field.

2.4.1 Variant of the SIMPLE Algorithm

The variant of the SIMPLE[15] algorithm is presented in short[20] for the solution of the primal problem

$$a_P u_{P,i} = \sum_{N=1}^{NB(P)} a_N u_{N,i} - \frac{\partial p}{\partial x_i} + b_i \tag{2.9}$$

where P is the cell index in which the momentum equations are discretized and $NB(P)$ are the neighbouring cells of the cell P, as shown in Figure 2.3. The vector b is referring to specific source terms that may be present in the momentum equations. Lastly, a_P and a_N are coefficients that resulted from the discretization of the convection and the diffusion terms, that consist the momentum equations.

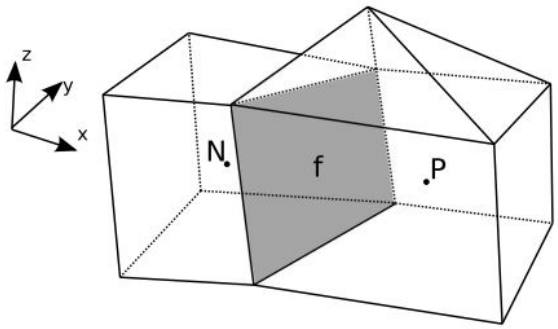

Figure 2.3: *Mesh cell, centered at P and one of its adjacent mesh cells centered at N. The two cells share a single face f, namely their interface. From [20]*

This equation is iteratively solved to acquire the velocity field u^*, using the pressure field p^*, that was obtained through the previous iterations.

$$a_P u^*_{P,i} = \sum_{N=1}^{NB(P)} a_N u^*_{N,i} - \frac{\partial p^*}{\partial x_i} + b^*_i \tag{2.10}$$

However, this velocity field u^* does not satisfy the continuity equation. For this reason, ${u_i}'$ and ${p_i}'$ are introduced as the velocity and pressure corrections that need to be added to u^* and p^* for satisfying the continuity equation

$$u_i = u^*_i + {u_i}'$$
$$p = p^* + p'$$

The velocity and pressure corrections relationship is calculated by subtracting equation 2.10 from 2.9, assuming that the coefficients a_P, a_N and the source terms b_i are

approximately the same in each expression

$$a_P {u_{P,i}}' = \sum_{N=1}^{NB(P)} a_N {u_{N,i}}' - \frac{\partial p'}{\partial x_i} \tag{2.11}$$

The equation 2.11 is further simplified by assuming that the first term on the r.h.s. is negligible compared to the gradient of the pressure correction,

$${u_{P,i}}' = -\frac{1}{a_P}\frac{\partial p'}{\partial x_i} \tag{2.12}$$

The continuity equation must be satisfied by the resultant velocity field, meaning

$$\frac{\partial u_i}{\partial x_i} = 0 \Leftrightarrow \frac{\partial u_i^*}{\partial x_i} = -\frac{\partial {u_i}'}{\partial x_i} \tag{2.13}$$

and by including the expression of the velocity correction ${u_i}'$ from equation 2.12 yields

$$\frac{\partial u_i^*}{\partial x_i} = \frac{\partial}{\partial x_i}(\frac{1}{a_P}\frac{\partial p'}{\partial x_i}) \tag{2.14}$$

Then, equation 2.10 is taken into account, in order to extract a relationship for calculating the pressure field in accordance with the continuity equation by

$$\frac{\partial}{\partial x_i}[\frac{1}{a_P}(\sum_{N=1}^{NB(P)} a_N u_{N,i}^* + b_i^* - \frac{\partial p^*}{\partial x_i})] = \frac{\partial}{\partial x_i}(\frac{1}{a_P}\frac{\partial p'}{\partial x_i}) \Leftrightarrow \frac{\partial}{\partial x_i}(\frac{1}{a_P}\frac{\partial p}{\partial x_i}) = \frac{\partial \hat{u_{P,i}}}{\partial x_i} \tag{2.15}$$

$$\hat{u_{P,i}} = \frac{1}{a_P}(\sum_{N=1}^{NB(P)} a_N u_{N,i}^* + b_i^*) \tag{2.16}$$

In summary, the steps that the SIMPLE algorithm follows, in order to solve the flow equations are:

1. Solve the equation 2.10 to obtain the velocity field u^*, based on the pressure field $p*$ and volume flux m_f from the previous iterations, or the initialization.
2. Compute $\hat{u_{P,i}}$ using the expression 2.16 and interpolate its values to the cell faces utilizing a linear interpolation scheme, since the field variables are stored in the cell centres.
3. Solve the pressure equation 2.15
4. Prepare for the next iteration by updating the volume flux m_f using the ac-

quired pressure field, which satisfies the continuity equation.

5. Explicitly relax the pressure field for applying it to equation 2.10 in the next iteration.
6. Update the velocity fields u_i at the cell centres using the relaxed pressure field.
7. Solve the turbulence model equation(s), if applicable.
8. If the desired level of convergence has been reached for all equations, the execution stops. Otherwise, return to step 1.

In the lubrication problem under investigation, PDEs are discretized and solved on hybrid grids using the cell-centered, collocated, Finite Volume infrastructure of the OpenFOAM toolbox.

2.5 Key Performance Indicators(KPIs)

The results of all performed fluid-dynamics simulations for the lubrication problem were evaluated based on their compliance to the expected output fluid-phenomena, as those are conceived from theory. Instead of examining only the domain's velocity and pressure, three performance indicators were selected and calculated, formed on these magnitudes for every different geometry. These values were used to determine which cylinder bore surface showed more efficient lubrication characteristics, in terms of the shear flow-factor[21], the pressure flow-factor[22] and the specific friction.

2.5.1 Flow-Factors

In general, a flow-factor is calculated by the fraction of the oil's mass-flow Q_{real}, or volumetric flow for incompressible fluids, passing between the piston and the cylinder liner, divided by the mass-flow $Q_{flat//plates}$ of the oil which is passing between two flat, parallel plates, that occupy the same volume, as the real, computational domain.

$$\phi_i = \frac{Q_{real}}{Q_{flat//plates}} \tag{2.17}$$

where ϕ_i is the symbol of the flow-factor, while the index $i = s$ is used to name the shear flow-factor or $i = x$,or z to mark the pressure flow-factor towards the respective axis.

In other words, each flow-factor is an indicator of the mass-flow difference between the oil moving on a rough surface, compared to the same flow over a smooth surface. Textured surfaces are usually preferred from smooth ones, because their morphological features contribute in better lubrication performance. Especially on grooved

walls, each surface cut serves as a "local" oil supply, aiding in the reduction of friction, that is applied on the moving components. Additionally, the groove's volume is used for trapping material's wear, or debris, thus preventing them from interfering with the function, or the motion, of the moving parts. Therefore, better lubrication characteristics are expected with grooved surfaces, that result in small values of the flow-factors, because more oil is stored inside the grooves, when compared with the oil quantity over a smooth surface. Expanding the initial definition, each of the flow-factors is explained below.

- **Shear flow-factor** ϕ_s: Its denominator is the oil's mass flow which is passing between two flat, parallel plates, where the bottom plate is stationary and the top plate is moving with a velocity vector $\mathbf{V} = (U, 0, 0)$, equal to the piston velocity. In this case, the oil undergoes a Couette flow, thus ϕ_s can be calculated as

$$\phi_s = \frac{Q_{real}}{U \cdot \frac{h}{2} \cdot depth} \tag{2.18}$$

  where h is the distance between the two examined, flat, parallel plates and *depth* is the depth of the computational domain.

- **Pressure flow-factor** ϕ_x: The mass-flow of the denominator is found by integrating the oil's velocity profile, which is formed by a pressure difference applied between the inlet and the outlet of the rectangular, computational domain. Likewise, this type of oil-flow is subjected to the principles of Poiseuille flow and ϕ_x can be extracted by

$$\phi_x = \frac{Q_{real}}{\frac{\frac{dp}{dx} \cdot h^3 \cdot depth}{12 \cdot \nu}} \tag{2.19}$$

  where $\frac{dp}{dx}$ is the pressure difference between the inlet and the outlet of the domain.

2.5.2 Specific Friction

Specific friction is defined by the fraction of the friction force, applied on the moving surface, divided by its vertical load

$$\mu_i = \frac{F_i}{F_y} \tag{2.20}$$

where μ_i stands for the specific friction towards the direction of motion and index $i = x$ (2D flow), or $i = z$ (3D flow), corresponds to the axis that the motion is held. In 3D oil-flows, both indexes are applicable. F_i is the friction force opposing the motion of the moving component, applied in the same direction and F_y is the

normal force, exerted normal to direction of motion.

Instead of comparing, directly, separate values of the developed friction and the load carrying capacity for each alternative geometry, these important magnitudes are combined to one, specific friction. This way, both values are taken into account during the performance evaluation of each different, grooved surface. The goal is to reduce specific friction either by decreasing the friction force opposing the piston's motion, or/and by increasing the normal load applied at the piston's rings.

2.6 Summary

In this chapter, the validity of the continuum approach into the examined micro-fluidics problem was inspected. Since it is applicable to the lubrication problem, the fundamentals of fluid mechanics and the computational methods that were applied for acquiring the lubricant's flow field were briefly described. The flow-factors and specific friction serve as performance indicators for the lubrication effectiveness in the following simulations.

Chapter 3

Modelling the Lubrication between the Piston Ring & Cylinder Liner

3.1 Introduction

The process that was followed in order to model the lubrication between the piston's top ring and the liner, is explained. The detailed geometry of the top ring, along with the cylinder's inner wall surface topography were considered. The features of the physical problem are justified along with its simplifying assumptions. The lubricant's properties are presented, while the pressure and the velocity boundary conditions(BC) were derived from the selected operation point of the ICE. Furthermore, an investigation on the velocity BCs for the domain's inlet & outlet, was conducted. The numerical schemes for discretizing the lubricant's flow equations are listed together with the algorithm controls of the simulation. Once the computational model was ready, grid independence studies were performed. Then, a parametric analysis was carried out with the purpose of determining the influence of the groove's width, depth and pitch over the friction which is applied at the top ring.

3.2 Geometry

The geometry consists of the piston, its top ring and the cylinder wall assembly. Every component has a cylindrical, or circular shape. Thus, instead of simulating the entire cylinder, only a periodic cylindrical segment of it was taken into account. Since, the dimensions of the bore's surface texturing is three orders of magnitude lower than the dimensions of the piston-cylinder assembly, the selected angular piece was further broken down to a smaller piece with appropriate length. Its length should be large enough, in order to include the ring's cross-section and two grooves from the cylinder's wall as a minimum, as depicted in Figures 3.1 & 3.2.

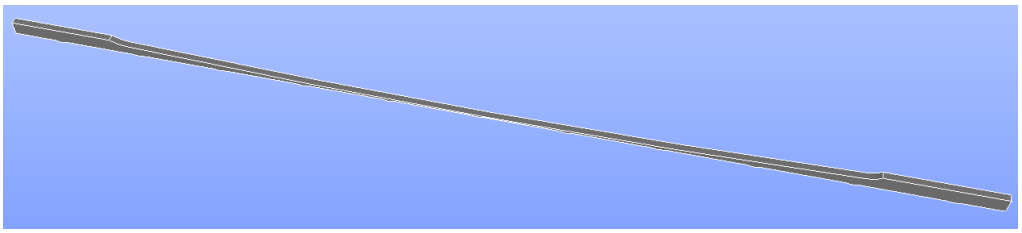

Figure 3.1: *Top ring on grooved cylinder wall, focus is on the top ring*

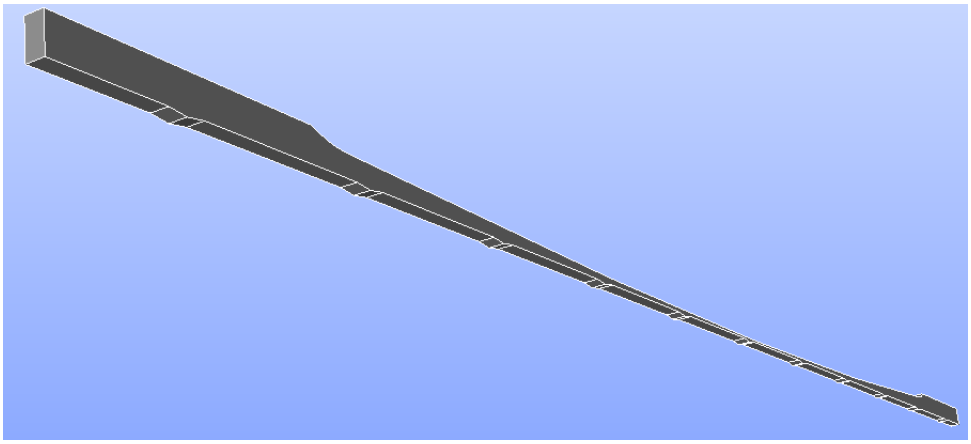

Figure 3.2: *Top ring on grooved cylinder wall, focus is on the grooved wall*

A tool for automatically generating the geometry of the computational domain, is required. For this reason, a framework was developed in FORTRAN 95. Specifically, this receives as inputs the ring's geometry in text format, the design variables, namely groove width, depth and pitch, as shown in Figure 1.10, and several additional quantities, in order to fully define the computational domain. The latest are the domain's depth, which is essential for 3-D simulations and the film thickness, which is the shortest distance between the top ring and the cylinder wall for fully flooded condition. The cylinder liner surface topography was simplified by assuming that the hatch angle is 0^o, meaning that the grooves are not crossing with each other.

The first framework's advantage is that simulations can be performed for alternative top ring geometries, or even for different rings(oil ring, compression ring) of the piston-ring pack. Secondly, it is possible to select the groove's shape, between triangular, or a profile created by a cosinus function. Additionally, its major benefit is that it quickly generates the necessary geometry files in .stl format, based on the imported values of the design variables. Attention was given on the time needed for generating these files. Normally, the detailed geometries of the engineering components are designed using a CAD software. Then, they are exported in .stl format, or any other convenient extension and checked if they compose a watertight geometry. If not, they need further treatment by the CAD software and the previous actions are repeated until the condition is satisfied. This manual, time-consuming process is avoided by the steps that the code follows for creating the geometry files. More information regarding the work-flow of the framework is found in Figure A.2.

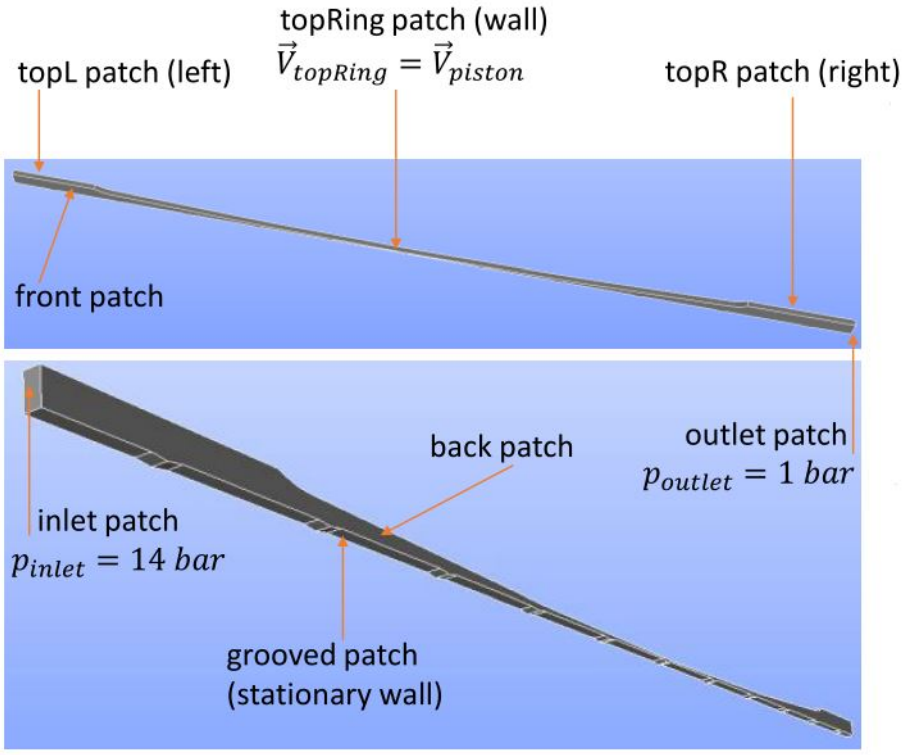

Figure 3.3: *The patches of the computational domain*

The boundaries of the computational domain, that are shown in Figure 3.3, are named according to the engine component that they represent, as listed in Table 3.1. By observing the piece of the cylinder assembly under investigation, as shown in Figure 3.1 with its corresponding dimensions, two different scales are introduced. The first scale is dependent on the oil film thickness δ and is bounded by the range $(0.01 - 2]\mu m$, which is used as reference for the specific problem. The oil film thickness determines the height of the narrowest cross-section inside the computational

domain. The second scale is associated with the dimensions of the cylinder wall's pattern prototype unit. For this case, the geometrical values belong to $[10-2000]\mu m$, or more, depending on the selected length of the computational domain towards the horizontal and the lateral axis.

Name	Explanation
topRing	Top ring's cross-section shape
topR	Piston wall next to the combustion chamber
topL	Piston wall between consecutive rings, where the latter is the examined top ring
grooved	Cylinder bore
inlet	Vertical section of the piston assembly between consecutive rings
outlet	Vertical section of the piston assembly next to the combustion chamber
front	Longitudinal section of the piston assembly(front side)
back	Longitudinal section of the piston assembly(rear side)

Table 3.1: *The boundaries comprising the top ring and the inner cylinder wall*

3.3 Features of the Physical Problem

The lubricant's flow is governed by the steady-state Navier-Stokes equations for an incompressible fluid and the selection of this steady-state solver is justified in the current section. Modelling engine lubrication demands sufficient handling of various, complex, fluid phenomena, such as transient oil-flow, cavitation, heat-transfer etc. Each of these add more computational time to any CFD simulation. The accuracy and the complexity of a computational model is a compromise between the available resources and the needed clock-time for the simulation in most industrial applications. In this regard, the lubrication problem under investigation was simplified and a CFD model was developed for determining the influence of the bore's surface roughness parameters. In reality, the piston performs a periodic motion with a cosine path. In order to conduct an unsteady simulation for the entire cylinder stroke, attention must be given to the base dimensions of the computational domain, the duration of the piston's operation cycle and the timestep. For the current problem, the computational domain is described by a rectangular with dimensions 88.5×80.5 in mm. Assuming that the engine's rotational velocity is $n = 2000$ rpm, then $\omega = \frac{2\pi n}{60} = 209.33\frac{rad}{s}$ and the time needed to complete a cycle is $T = \frac{2\pi}{\omega} = 0.03$ sec. The timestep is dependent on the spacial discretization of the computational domain and their relationship is expressed by the Courant number[23],

$$Co = \Delta t \tau \tag{3.1}$$

$$\tau = \frac{1}{2V} \sum_{faces} \phi_i \tag{3.2}$$

where Δt is the size of the timestep, τ is a characteristic time scale based on the local cell flow scales, V is the cell volume, ϕ_i is the face volumetric flux and $\sum_{faces}$ summation is over all cell faces. In general, the Co number serves as a measure of the rate at which information is transported under the influence of a flux field and as a limiting factor for the performance of numerical schemes. Consequently, its value affects the accuracy of the results and the stability of the solver. Likewise, it is dependent on the application, but it's a common practise for it to be close to 1, $Co \leq 1$ especially for explicit temporal discretization schemes. Accordingly, the timestep is usually fine-tuned until the previous condition is satisfied.

Aiming to ensure the stability of the unsteady, incompressible solver, the timestep size was investigated along with different Courant numbers for a simplified 2D geometry, as shown in Figure 3.4. Considering that the bore's surface characteristics are expressed in μm and the groove depth can reach values as low as 1.5μm, then the spacial resolution of the domain in the vicinity of the cylinder wall has to be at least 0.5μm, in order to sufficiently describe those features. For this reason, a smaller computational domain was used with the same texturing characteristics in order to reduce the mesh volume and its generation time. It comprised of a flat plate on top of a textured surface with consecutive grooves. Next, the timestep size was investigated, in order to perform unsteady simulations with $Co = 0.5, 1, 1.5, 2$ and 3.

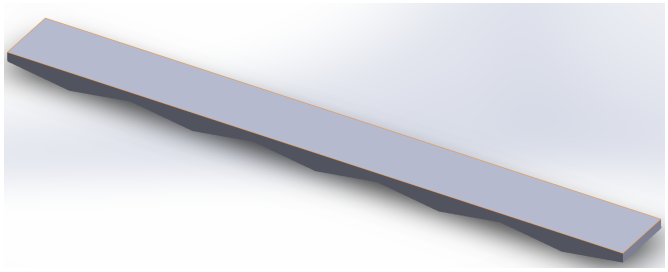

Figure 3.4: *Flat plate on grooved cylinder wall for hatch angle* 0*deg, groove depth 2 μm, groove width and pitch 20 μm*

In the OpenFOAM environment, it is possible to select either an adjustable or a constant timestep during the simulation. In the first case, the timestep is adjusted in order to acquire the maximum Co number, that was defined, while for constant timestep the Co number results from equation 3.1. It is worth mentioning that the timestep should remain constant. In the opposite scenario, there is a chance that the timestep would increase or decrease rapidly from iteration to iteration and valuable information concerning the flow field will be lost or distorted. However, for the problem at hand both alternatives were examined. For the constant timestep, regardless the value of the Courant number, the needed timestep was $\Delta t = O(e^{-12})$ s. In the opposite case, it was observed that the initial timestep should be in the same order of magnitude, but as the solution was marching forward in time, it reached $\Delta t = O(e^{-9})$ s and was oscillating between $\Delta t = 4e^{-9}$ s and $\Delta t = 5e^{-9}$ s.

Assuming that the selected timestep was $\Delta t = 4.5e^{-9}$ s, the average execution time for each iteration was 15 s. Supposing that only one of the engine's strokes were to be simulated, its duration is $\frac{T}{4} = 0.0075$ s. For the selected timestep, it corresponds in $N = \frac{0.0075}{4.5e^{-9}} = 1.66e^{6}$ iterations. Thus, the clock time needed in order to complete this unsteady simulation would be

$$Clocktime = \frac{Iterations \cdot Execution\, time}{3600\frac{sec}{h} \cdot 24\frac{h}{day}} = 289\, days \tag{3.3}$$

which is a very large time period for performing this kind of simulations. As a result, a steady-state solver was used. The usage of an unsteady solver is prohibited by the transient nature of the cylinder's operation, which shows periodicity. This feature would require from the unsteady solver to complete at least 2 to 3 operation cycles of the cylinder until the resultant flow fields reveal the periodicity in the developed flow phenomena.

Furthermore, the type of flow is characterized as laminar, or turbulent, based on the value of the Reynolds number, as long as its value is above one[24]. It is calculated by the fraction of the piston's velocity multiplied by the film thickness and divided by the oil's kinematic viscosity,

$$Re = \frac{V \cdot h_T}{\eta} \tag{3.4}$$

for the problem under investigation. On the other hand, if its value is below one, attention must be given for detecting a creeping flow. In this event, the Reynolds number should be considerably below one, $Re \ll 1$ and the products of Reynolds number multiplied by the Euler number or by the Strouhal number, consecutively, should be one, in the order of magnitude[18]. It should be noted that in creeping flows, the cause of such a small value for the Reynolds number is the low velocity of the moving wall. Also, the inertia convective terms can be neglected from the Navier-Stokes equations, pressure does not have a constant distribution over the film thickness and a different system of linear momentum equations is used for describing the flow[18]. The magnitude of the Reynolds number for the specific application is calculated in the following section, that the selection point is defined, along with the piston's velocity.

3.4 Working Point Selection

The selection of a specific working point for the engine is needed for defining the pressure and the velocity boundary conditions. Commonly, it is described by the pair of the engine's rotational speed and the generated torque. The engine map

is a 2-D illustration of all possible working points for the ICE and its working range is limited by the full-load curve, the minimum and the maximum acceptable rotational speed. Instead of selecting an arbitrary point from the engine map, the friction measurements[11] from a floating liner[25], [26] experiment were used.

The pressure in the combustion chamber, the friction opposing the piston's motion and the thrust force were measured for a naturally aspirated, spark-ignited, 1.797 cm^2 in-line-4-cylinder engine, that was configured based on the floating liner method. Four 3-component force transducers were mounted lengthwise on the cylinder liner, so that they could measure the frictional force between the piston and the cylinder. These force sensors hold tighter to the liner compared to other floating liner configurations, which leads to measurements with higher accuracy.

The non-dimensional friction force measurements are shown in Figure 3.5 for engine rotational speed 2000 rpm. It is observed that the friction acquires its greatest values in the beginning of the power stroke, especially in crank angle $\theta = 0^o$, when the crank reversal is held. In this moment, boundary lubrication is present between the piston ring-pack and the cylinder liner, because most of the lubricating oil has been scrapped off during the compression stroke. Also, the combustion has ignited which leads to high temperature and pressure conditions inside the combustion chamber, that in turn affect the viscosity of the oil and the film thickness. It has become clear that in this lubrication regime, the asperities from the liner's surface and the ring-pack strongly interact with each other, resulting in dry-friction. This type of friction is mostly affected by the geometry and the surface roughness of the interacting parts in the macro-scale and the meso-scale.

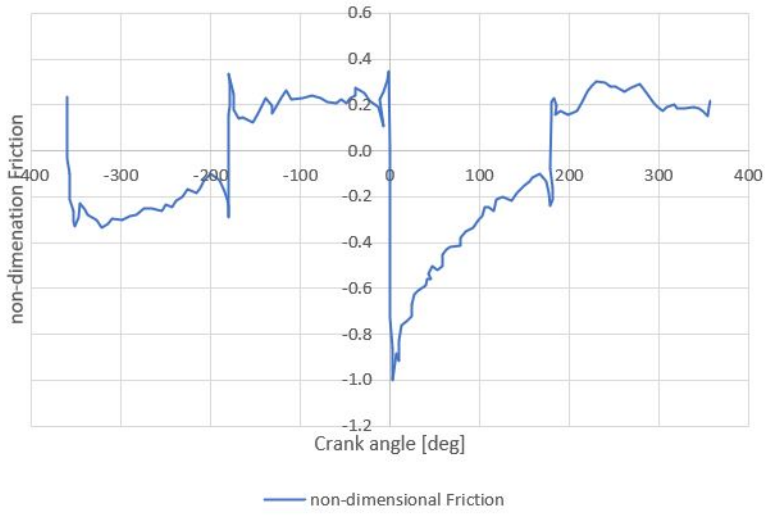

Figure 3.5: *Non-dimensional friction with crank angle relative to TDC*

From Figure 1.7 it is apparent that the lubrication regime between the piston-ring pack and the cylinder liner is either mixed, or hydrodynamic. For this reason, the

working point cannot be selected by merely observing the friction force measurements. An alternative magnitude was used, which is the friction power P_F and is calculated by the product of the measured, frictional force multiplied by the piston's velocity in the respective crank angle,

$$P_F = F \cdot \mathbf{V_p} \tag{3.5}$$

where F is the friction force measurement and $\mathbf{V_p}$ is the piston's velocity as shown in Figure 3.6.

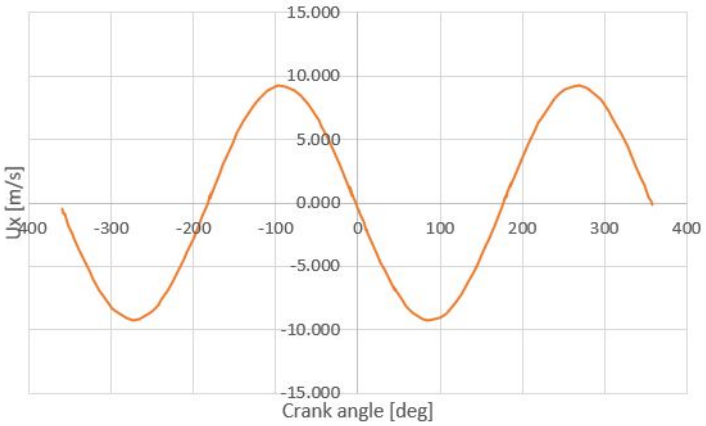

Figure 3.6: *Piston velocity with crank angle relative to TDC*

The results of the non-dimensional power loss are shown in Figure 3.7. It is observed that the most power is lost during the power stroke, namely for $\theta = [0^o - 180^o]$. It is interesting that the variation of power loss with crank angle follows the change of piston velocity with crank angle, regardless the direction of the piston. This is happening because the friction force shows small deviation, or can be considered constant with crank angle during each stroke, except the power stroke.

In this manner, the engine's operation point was selected as the point where the friction power loss is maximum. Thus, the velocity and pressure conditions for this point of operation were chosen for detecting which surface characteristics of the cylinder liner contribute the most in friction reduction. This point is found from Figure 3.7 in crank angle $\theta_{P_{max}} = 60^o$ that the piston velocity is $\mathbf{V_p} = (7.261, 0, 0)\frac{m}{s}$. Since the maximum power loss is found near the middle of the cylinder's stroke, then the piston's velocity receives almost its largest values and a relatively thick film separates the top ring from the cylinder liner. Consequently, hydrodynamic lubrication is present and the passage between the top ring and the cylinder liner was assumed to be filled with lubricating oil. Therefore, the oil film thickness specified the smallest vertical distance between the top ring and the cylinder liner for the investigated geometry. In the same series of experiments, the oil film thickness was measured for the top ring and the second ring of the ring-pack during the operation

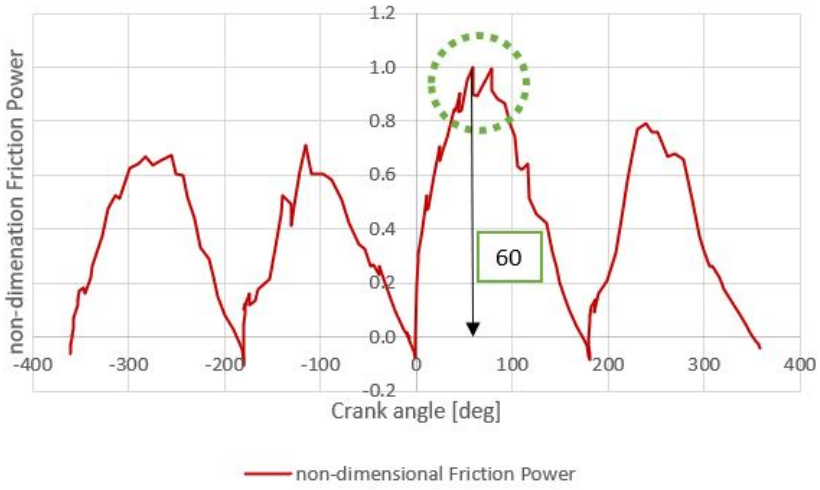

Figure 3.7: *Non-dimensional power loss with crank angle relative to TDC*

cycle of the tested engine. The film thickness between the top ring and the cylinder wall was found as 1.5μm at the crank angle with the greatest power loss.

At this stage the pressure and the velocity conditions are defined at the boundaries of the computational domain. Hence, the Reynolds number is calculated by

$$Re = \frac{7.261 \cdot 1.5\,10^{-6}}{5.10\,10^{-6}} = 2.14 \tag{3.6}$$

which is above one. It is concluded that the lubricant's flow is laminar.

3.5 Boundary Conditions

Boundary conditions are essential for solving the flow equations of the lubrication problem at the boundaries of the computational domain. These are dictated by the lubricant's flow at the respective positions. The most common types of boundary conditions(BC) are:

- **Dirichlet BC**, where a specific value of the independent variable is assigned to the boundary.
- **Neumann BC**, where a specific value of the independent variable's gradient component, normal to the surface, is assigned to the boundary.

Alternatively, a combination of those types can be utilized such as Robin type conditions. Also, it is possible to impose boundary conditions for quantities such as mass-flow, total pressure etc. which are calculated by the velocity, and/or the pressure field.

For the current problem, a Neumann BC with zero value for the pressure was applied at the top ring and the cylinder's bore surface, because the flow is attached and there in no velocity acceleration normal to the walls. On the other hand, Dirichlet BC for pressure was assigned to the inlet and the outlet of the domain. Since the selected working point belongs to the expansion stroke and the outlet is exposed to the atmospheric conditions, the outlet's pressure is $p_{outlet} = 1\,bar$. Furthermore, the domain's inlet was assumed to have pressure equal to the one of the compressed cylinder gas which is dependent on the piston's displacement. Consequently, the Dirichlet BC is equal to the measured cylinder pressure at the selected working point, specifically $p_{inlet} = 14bar$.

The piston's and top ring's velocity was defined by the selected operating point, thus a Dirichlet BC was used, equal to $\mathbf{V_p} = (7.261, 0, 0)\frac{m}{s}$ where the piston is moving in the x-direction. Given that the engine's cylinder is stationary, then a Dirichlet BC with zero value was assigned to the inner cylinder wall. While a zero Neumann BC was used for the outlet, in order to allow for the flow development. There was no experimental measurement for defining the velocity BC at the inlet. For this reason, a comparison was conducted between zero Neumann BC and a mixed BC for the velocity, namely pressureInletVelocity[27]

$$pressureInletVelocity(\mathbf{u}) = \begin{cases} \frac{\partial \mathbf{u}}{\partial n} = 0, if\ flux > 0 \\ \frac{flux}{S_f}|_n, if\ flux < 0 \end{cases} \tag{3.7}$$

where n corresponds to the direction normal to the surface of the cell, flux is the mass-flow entering, or exiting the domain's inlet and S_f is the surface's area. It is usually applied to boundaries where the pressure is specified and the inflow velocity is obtained from the flux with a direction normal to the boundary. The difference in the resultant forces was below 0.01%, so zero Neumann BC was used for the domain's inlet too. The specified boundary conditions are summarized in Table 3.2.

Boundary	**Velocity**	**Pressure**
topRing	Dirichlet $\vec{V} = (7.261, 0, 0)$	zero Neumann
topR	zero Neumann	zero Dirichlet
topL	zero Neumann	Dirichlet $p = 14bar$
grooved	zero Dirichlet	zero Neumann
inlet	zero Neumann	Dirichlet $p = 14bar$
outlet	zero Neumann	zero Dirichlet
front	Periodic	Periodic
back	Periodic	Periodic

Table 3.2: *Boundary conditions for pressure and velocity between the top ring and the bore's grooved surface*

3.6 Numerical Schemes & Convergence Criteria

Prior to numerically solving the fluid-flow equations, these must be discretized using the cell-centered Finite Volume infrastructure of the OpenFOAM toolbox. Since this process as explained in Section 2.4, is automated, the user has only to specify the numerical integration schemes to be used for discretizing the terms of the surface, or volume integrals in the momentum equations. These integrals may include the gradient of a magnitude i.e. the pressure term $\frac{\partial p}{\partial x_i}$, the divergence of a magnitude ϕ i.e. the diffusion term $\Gamma^{\phi}\nabla\phi$, the laplacian of a magnitude i.e. the viscous stresses for constant viscosity $\mu\nabla^2\mathbf{u}$. Also, it is possible to utilize corrections or limiters depending on the grid's properties, to the scheme that is applied for the gradients normal to cells' surface. At the same time, an interpolation scheme is chosen for approximating the unknown variables from the cell's centre to the cell's faces, given that a cell-centered, collocated approach is followed for their storage.

The selected discretization schemes for the current application are summarized in Table 3.3. All convection terms were discretized using second-order upwind schemes which were "bounded" for ensuring stability. "Bounded" schemes[28] are common in steady-state flows because by utilizing them, the unknown variables are constrained by the conservation of mass until the former is satisfied. The spatial gradients and the diffusion terms were discretized using central differences. A limiter was applied at the velocity gradient to ensure uniformity between the velocity values of neighboring cells. This way, when using upwind schemes, the face values are bounded by the values of the surrounding cells. Non-orthogonal correction was applied on normal to surface gradient and laplacian discretizations in order to maintain second-order accuracy.

Symbol	**Name**	**Discretization or Interpolation scheme**
$\nabla\phi$	gradSchemes	Gauss linear corrected
$\nabla\mathbf{u}$	grad(U)	cellLimited Gauss linear 1
$\nabla\cdot(\phi\mathbf{u})$	div(phi, U)	bounded Gauss linearUpwind grad(U)
$\nabla^2\phi$	laplacianSchemes	Gauss linear corrected
$\phi_C \Rightarrow \phi_f$	interpolationSchemes	linear

Table 3.3: *The discretization and interpolation schemes for the lubrication problem following the OpenFOAM terminology. The index C corresponds to the value of ϕ at the cell centre and index f to the value of phi at the cell face.*

The linearized system of the primal equations is numerically solved by the SIMPLE algorithm until the user-defined residual threshold for the unknown field variables is achieved. The residual control for the pressure and momentum PDEs was set as $1e-08$ in the lubrication problem. Furthermore, under-relaxation factors are applied to stabilize calculations by limiting the rate of change of the pressure field and the velocity equations. Also, a linear solver is selected for each unknown variable

depending on whether the matrices are symmetric or not. They are implemented in every iteration until the residuals of the equations fall below $1e-12$ which was the user-defined solver's tolerance. Furthermore, the solver's relative tolerance that is the ratio of current to initial residuals is determined for each unknown variable and was set as 0.01 for both. Once the equation's residual or the relative tolerance of the current iteration falls below its pre-defined value, the solution can be considered sufficiently accurate because the present residual is small enough.

The velocity field was initiated by solving the velocity's potential equation $\nabla^2\Phi = \nabla\mathbf{u}$, where Φ is the velocity potential in $\frac{m^2}{s}$ and $\mathbf{u} = \nabla\Phi$. The solution starts from the boundaries of the domain and marches in space from one side to another in order to calculate the flux-field. This is reconstructed back to the velocity field which serves as the initialization prior to solving the Navier-Stokes equations.

3.7 Mesh Sensitivity Analysis

Before proceeding with the parametric analysis, two different investigations were conducted related with the computational domain's geometry and its mesh. In both cases 2-D geometries were employed. In the first part, the length of the computational domain before and after the top ring was examined. This study was performed in order to find the minimum lengths that didn't numerically affect the simulation results. They were assessed based on the forces, that were applied on the top ring whose geometry remained constant in every alternative computational domain's geometry. In the second part, grid independence studies were carried out with different mesh densities, or a combination of these. Again, their results were evaluated based on the top ring's forces and the computational time, which was needed for generating those meshes.

The initial geometry consisted of the top ring's profile and the grooved liner surface with 20μm groove pitch, equal to the groove width, which implies that the edges of the consecutive grooves were attached to each other. The groove depth was 5μm and 15 grooves were placed before and after the top ring. This served as the reference case whose results were compared with the force magnitudes that were computed by alternative combinations. These pairs were made between different number of grooves, that is 1, 3 and 5, following the inlet as shown in Figure 3.8 and preceding the outlet. All the examined couples of grooves are shown in Table 3.4 where the first row depicts the number of groove following the inlet and the first column represents the number of grooves preceding the outlet. The combination with the minimum number of grooves was selected before and after the top ring, whose difference from the reference scenario was lower than 1 %. This way, the needed memory for the storage of the mesh is low enough and for the cases that groove pitch is greater than the groove width, the length that was found serves as the lower limit for the liner's wall length.

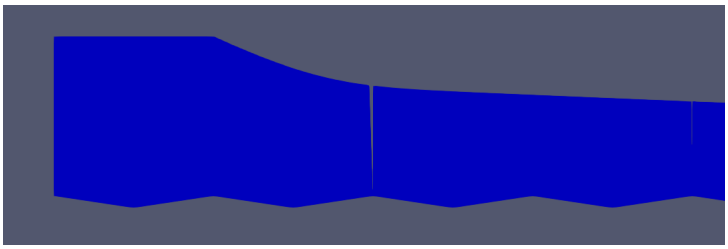

Figure 3.8: *Focus on 1 groove placed after the domain's inlet*

Combinations	1	3	5	15
1	•	•	•	
3	•	•	•	
5	•	•	•	
15				•

Table 3.4: *Combinations of the number of grooves following the inlet (first row) and preceding the outlet (first column)*

The percentage of force $\mathbf{F} = (F_x, F_y)$ differences between alternative pairs are shown in Tables 3.5 & 3.6. Especially for all possible combinations including one groove in either of the sides, they showed great deviation from the reference case and were immediately rejected. In the remaining combinations, it is observed that forces are more dependent on the number of grooves preceding the outlet, than the ones that are following the inlet. For this reason, the first row in both tables contains the greatest percentages. Consequently, five grooves should be preceding the outlet of the domain at least, or the minimum, acceptable length of the liner wall after the top ring is 100μm. The desired level of accuracy is achieved by the three grooves after the inlet, hence the minimum length of the liner before the top ring is 60μm.

Difference(%) from reference for F_x	3	5
3	> 50	> 50
5	0.24	0.02

Table 3.5: *Difference from reference case in longitudinal force F_x*

Difference(%) from reference for F_y	3	5
3	37.56	19.78
5	-0.02	< 0.01

Table 3.6: *Difference from reference case in vertical force F_y*

Next, the grid dependency studies were carried out for the same groove characteristics of the cylinder liner and with three grooves before the top ring and five grooves after it. The alternative meshes were assessed based on the needed time for their computation and the level of accuracy of their results compared to the force magnitudes that were calculated by the most dense mesh. The most dense grid comprised of $1e + 06$ cells, since the laminar flow of the lubricant is simulated for a 2-D geometry. In case that the flow was turbulent, the mesh would contain many more cells, or for 3-D geometries the resultant meshes easily exceed $2e + 06$ cells in average. On the contrary, the most sparse mesh that was investigated, contained 178 119 cells. Meshing the triangular shape of the grooves' cross-section, required a relatively large number of small cells in order to be simulated accurately and to avoid the distortion of its shape.

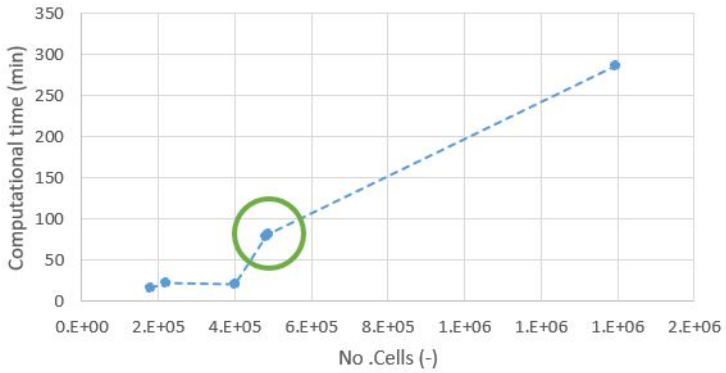

Figure 3.9: *Variation of computational time with increasing number of grid's cells(same number of CPUs, same architecture)*

The variation of time that is required for the mesh generation with increasing number of cells is illustrated in Figure 3.9. In reality, the relationship of computation time with the total number of cells isn't usually linear, but the graph's points are connected to each other with lines in order to depict the trends of their alterations. It is observed that the computation time is increasing as the number of cells increases too. However, the necessary time for the meshes with 2e+05 and 4e+05 cells, remains constant. Even though the disparity in their number of cells is notable, this is happening because the meshes' global level of refinement is the same for both cases, but the areas where a denser grid has been applied are different. In particular, for the grid with 4e+05 cells, the areas with denser grid compared to the global level of refinement are larger. Three different levels of refinement were investigated in general and are depicted from the Figure 3.9 points with 1.78e+05, 4.80e+05 and 1e+06 cells.

The change of the results' accuracy level with regards to the number of cells is shown in Figure 3.10. Instead of presenting the percentage of difference for the force components separately, the results for the longitudinal force are illustrated, because it showed the greatest variation between alternative meshes. The point with 0 % of

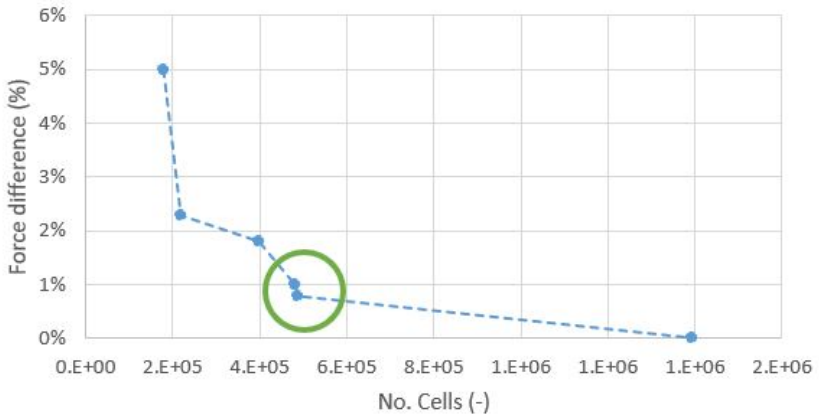

Figure 3.10: *Force variation percentages from the most dense mesh(1e+06 cells) with increasing number of the grid's cells*

difference corresponds to the most dense grid whose results are used for calculating the percentages of force difference. Again, the relationship between the accuracy of the results and the number of cells isn't linear and the points are connected with lines for illustration purposes. It is observed that the accuracy level is improved by increasing the number of cells. However, the rate of change for the accuracy of results is different between alternative meshes. It is expected to obtain quick, but not very accurate results with sparse grids. Still, it is interesting that the accuracy level is doubled by increasing the number of cells by one fifth of its initial value. As the number of cells is increased the level of accuracy is improved rapidly until the mesh with 4.88e+05 cells is reached. From this point forward, the rate of accuracy growth is very slow, compared to the rate of increase for the number of cells.

The grids for the present analysis and the following simulations were generated using the snappyHexMesh[29] utility supplied with OpenFOAM. In general, it creates 3-D meshes containing hexahedra (hex) and split-hexahedra (split-hex) automatically from triangulated surface geometries in specific file format. The mesh approximately conforms to the shape of the surface by iteratively refining an initial mesh and morphing the resulting split-hex mesh to the surface. An optional step is the addition of cell layers. The specification of mesh refinement level is very flexible and the surface handling is robust with a pre-specified final mesh quality. It runs in parallel with a load balancing step in each iteration. Since this mesh generator creates 3-D meshes, additional actions were taken in order to convert the 3-D meshes to 2-D. First, one side of the 3-D mesh which was normal to the direction were the flow wouldn't be solved, was selected. Then, this patch was extruded towards a specified length using the extrude utility(extrudeMesh) of OpenFOAM. This way, the resultant grid was converted to 2-D given that the direction normal to the fluid's flow contained only one cell which is the condition for identifying 2-D flows in the OpenFOAM toolbox.

Based on Figures 3.9 & 3.10, the level of refinement and the settings which lead to a mesh with 4.78e+05 cells were selected. This option resulted in the most accurate results compared to the most dense mesh alternative, notably below 1 % of difference between force magnitudes with double of the computational time needed for the most sparse alternative. This is depicted in both figures inside the orange circle. Nevertheless, this marking contains two points which correspond to alternative meshes with equal global level of refinement, but for the case with the greater number of cells, additional areas with denser mesh are present. These areas assist in increasing the accuracy of the results at the cost of higher computation time. It was concluded that the improvement in accuracy wasn't worth the higher computation time and the more complex settings for the mesh generation in the following simulations.

3.8 Case-Studies

The parametric analysis was conducted in order to observe the influence of the cylinder liner's surface characteristics over the friction that is opposing the piston's motion with focus on the top ring. The design space which is comprised by the design variables, namely the groove width, pitch and depth, was limited by the available manufacturing techniques. These parameters were selected instead of more generic ones such as depth over diameter ratio[30] $e = \frac{depth}{width}$ etc., because they allow to detect which groove feature highly affects the lubrication performance. The grooves are created by utilizing the honing process[13] described in Section 1.3.4, during which triangular grooves can be generated with pitch $[121 - 1000]\mu$m, depth $[1.5 - 10]\mu$m and width $[20 - 50]\mu$m. The honing configuration and the abrasive stones, or wheels, can be selected according to the desired accuracy for the most influential characteristic.

The design space was sampled in order to reduce the examined combinations for the parametric analysis. Every alternative option is described by three values, one for each design variable. The size of the design variables' ranges made it impossible to test every possible pairing within reasonable time. For this reason, the current analysis was conducted based on three points from every range. These were the maximum and the minimum value for each range. The third point was chosen based on the surface features of the liner that was used during the experiments for measuring friction. In particular, those were groove width=40μm, pitch=472μm and depth=5μm. The values of the design variables that were paired with each other, are summarized in Table 3.7.

The execution of the simulations was automated using a BASH script which performs the steps shown in Figures A.1, A.3 as long as the available processing units(CPU) are pre-defined. Firstly, the selected design variables of Table 3.7 are imported to the code. Secondly, the script calls the framework for generating the geometry files

Depth	Pitch	Width
1.5	121	20
5	472	40
10	1000	50

Table 3.7: *The values of the design variables in μm that were paired for the parametric analysis*

in convenient format. Each time, a unique pair of the design variables is imported to the framework along with the ring's profile. Then, the simulation folder is created for each combination and the geometry files are transferred to their designated position. A template case has been created which includes the necessary files and folders with the selected boundary conditions, field initialization, discretization schemes and algorithm controls for the examined application. These are copied inside every alternative case folder and the simulation begins. Upon the simulation's completion, the forces that are applied on the top ring are computed based on the resultant pressure and velocity fields. Only the force magnitudes on the top ring are taken into account, because among different surface characteristics of the cylinder liner the ring's profile remains constant. Therefore, their results can be directly compared even though they arose from computational domains with different dimensions.

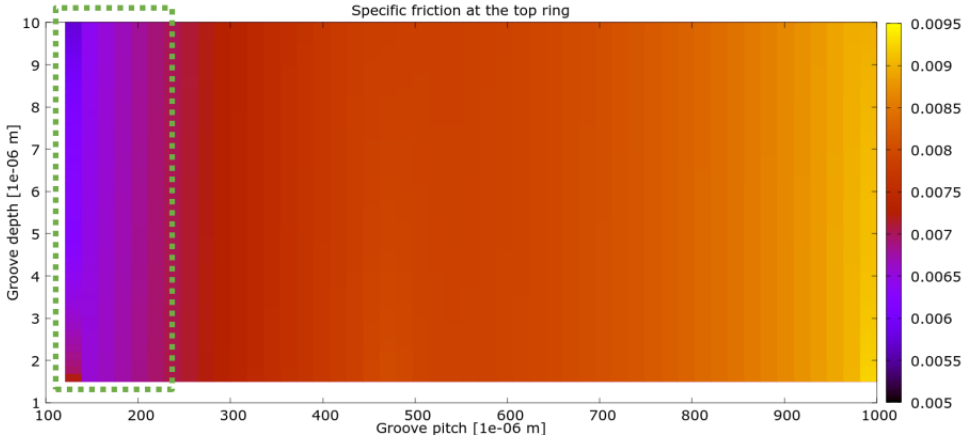

Figure 3.11: *Variation of specific friction on the top ring with regards to groove depth and pitch*

The results of these simulations are shown in Figures 3.11 & 3.12. These are colourmaps of specific friction at the top ring with regards to groove depth and pitch for Figure 3.11, or to groove width and depth for Figure 3.12. The light and warm colours correspond to high values for specific friction while the opposite is true for the dark and cold colours(purple). Hence, the areas of interest have purple colour since low values of specific friction are achieved by reduced friction for almost constant vertical load. From Figure 3.11 it is evident that lower specific friction is acquired with small groove pitch, regardless the value of depth.

Also, from Figure 3.12 it is observed that reduced specific friction is achieved with large values for the groove width as long as the depth is greater than 5μm.

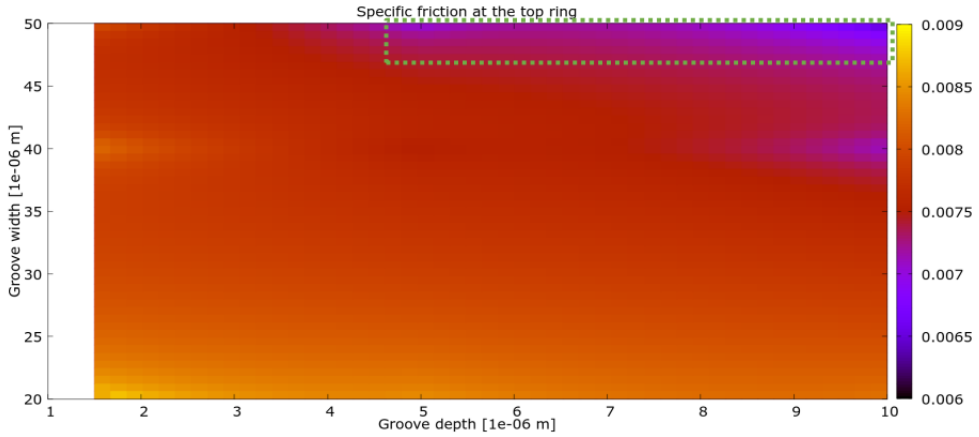

Figure 3.12: *Variation of specific friction on the top ring with regards to groove width and depth*

In total, 27 simulations were performed and the post-processed results are grouped together according to the varying design variable, while the remaining two are kept constant. The relationship between the specific friction and the examined design variable is not necessarily linear as shown in the following figures. Nonetheless, consecutive points in each diagram are connected to each other with a line, in order to depict the tendency of influence that the examined design variable has over the top ring's specific friction.

3.8.1 Varying the Groove Depth with Constant Pitch & Width

The first group of results is illustrated in Figures 3.13 & 3.14 where the change of specific friction is shown with regards to the groove depth for specific values of groove width and pitch.

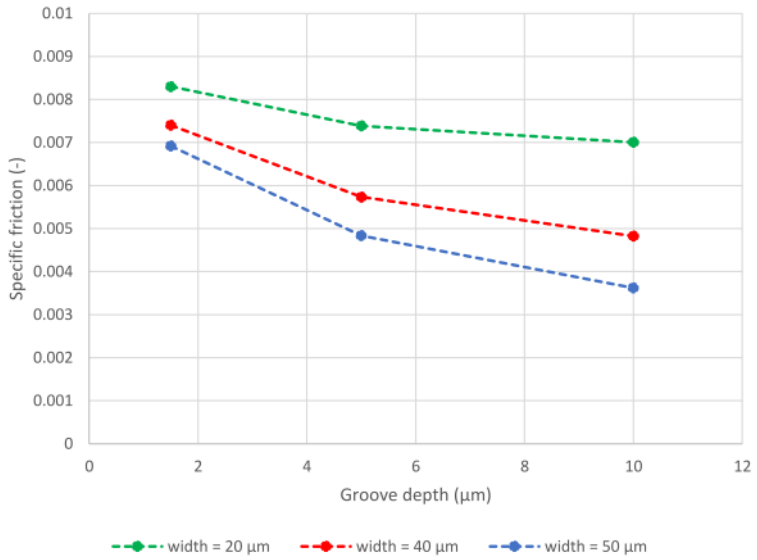

Figure 3.13: *Variation of specific friction on the top ring with regards to groove depth for pitch=121µm*

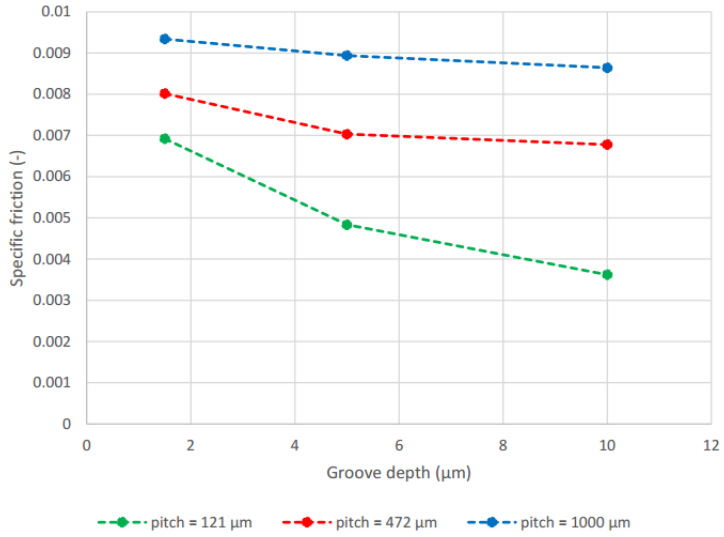

Figure 3.14: *Variation of specific friction on the top ring with regards to groove depth for width=50µm*

In Figure 3.13, it is observed that specific friction is reduced with increasing groove depth for every alternative width. However, the rate of change is different between low and high values of the groove depth. In particular, the reduction rate of specific friction is greater for small depths and this is common for every examined width. In Figure 3.14 specific friction decreases with increasing groove depth too for every alternative pitch. Although the rate of friction change is almost constant between different values of pitch. It should be noticed that for medium and large values of groove pitch, the specific friction is comparable between the two diagrams, but for the case with pitch=121μm, the results are better than the ones which belong to the data which are represented by width=20μm in Figure 3.13.

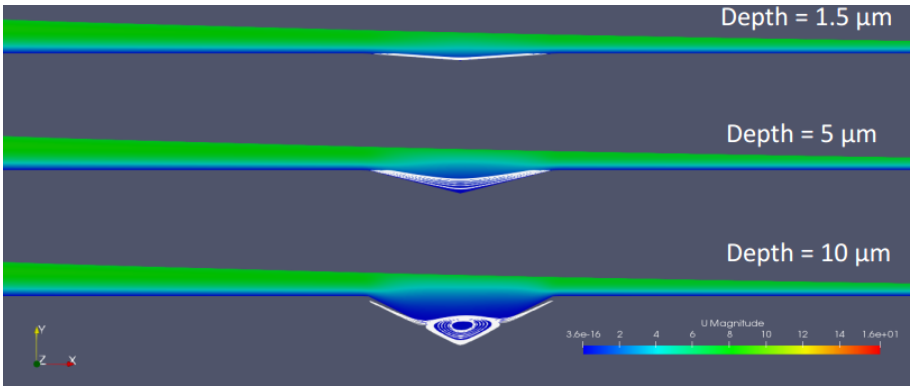

Figure 3.15: *Comparison of the streamlines inside the grooves between groove depth* 1.5μm, 5μm *and* 10μm *consequtively*

Based on both Figures 3.13 & 3.14, reduced specific friction can be acquired with increased groove depth. This statement is justified by observing the field of velocity magnitude between different groove depths with equal pitch and width as shown in Figure 3.15. The streamlines of the lubricant are presented inside the grooves. It is clear that as the groove depth increases, more oil is entering/exiting the groove's volume. By further increasing groove depth, the oil is depicted recirculating inside the groove. Since the velocity magnitude is 0 in the vicinity of the liner wall, then the lubricant is "trapped" inside the groove. Therefore, in deeper grooves, more oil is stored inside them which enhances the lubrication effectiveness.

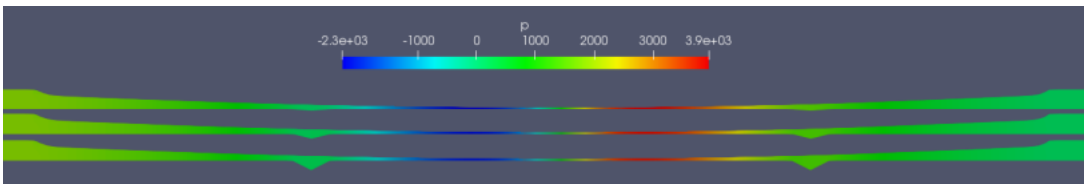

Figure 3.16: *Comparison of the pressure field between groove depth* 1.5μm, 5μm *and* 10μm *consequtively*

In Figure 3.16, the pressure field between different groove depths with equal pitch and width is shown. Every alternative case has the same minimum and maximum value, but they occur in different positions on the cylinder liner. This is explained by the mass-conservation at any cross-section of the domain. In particular, the fluid's velocity is increasing in the converging section of the domain. Also, the cross-section on shallow grooves is smaller than the one on deep grooves. For this reason, the velocity rise which is accompanied with pressure drop, is occurring sooner for the geometries with shallow grooves. The same is applicable to the diverging part of the domain, where the velocity decreases in order to maintain the same mass-flow.

3.8.2 Varying the Groove Width with Constant Pitch & Depth

The second group of results is illustrated in Figures 3.17 & 3.18 where the change of specific friction is shown with regards to the groove width for specific values of groove pitch and depth.

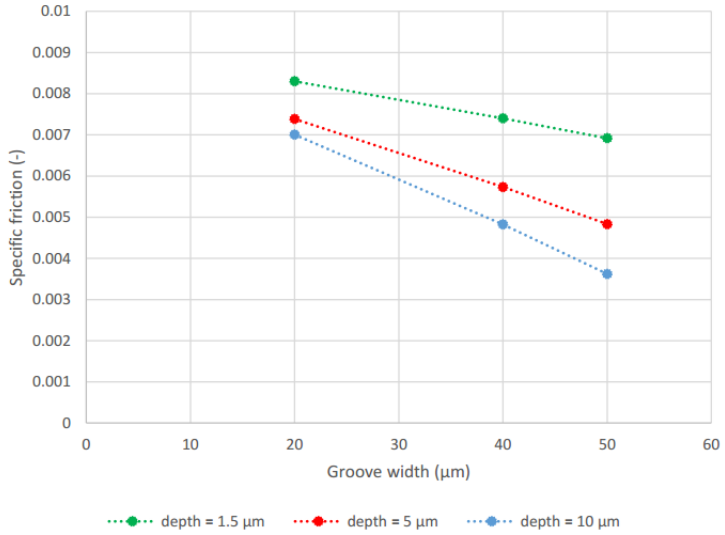

Figure 3.17: *Variation of specific friction on the top ring with regards to groove width for pitch=121μm*

From Figure 3.17, it is evident that specific friction decreases by increasing the groove width for each depth. The rate of change is almost constant through the entire width range and is greater for larger groove depths. The same are concluded from Figure 3.18. It is worth mentioning that the coefficient's reduction rate is increasing in a great manner as the groove pitch is decreased. The most sharp line of data is depicted in Figure 3.18 for pitch=121μm where the lowest value of specific friction is achieved. Also, the alternatives with medium to high groove pitch show

the greatest values of specific friction from both diagrams and lower reduction rate when compared with the medium and large groove depths.

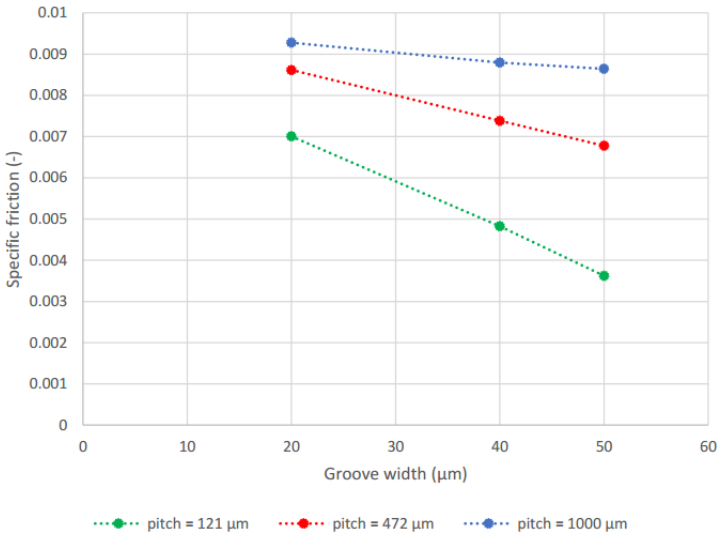

Figure 3.18: *Variation of specific friction on the top ring with regards to groove width for depth=10μm*

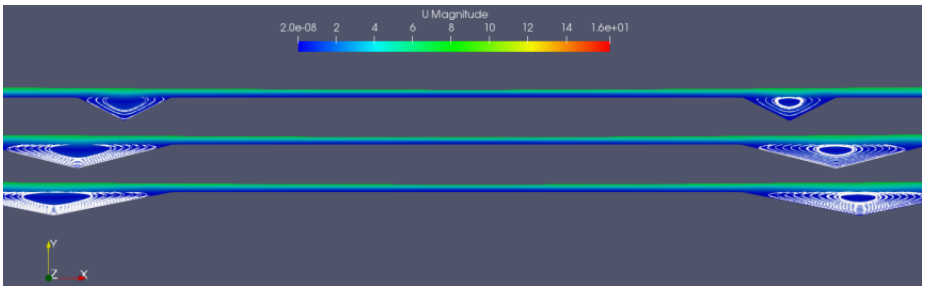

Figure 3.19: *Comparison of the streamlines inside the grooves between groove width 20μm, 40μm and 50μm consequtively*

From Figures 3.17 & 3.18, it is apparent that larger groove widths lead to lower specific friction on the top ring. This is justified by observing the field of velocity magnitude, which is shown in Figure 3.19, along with the fluid's flow streamlines inside the grooves. Attention is not given to the field of velocity vector because it is similar among alternative groove widths for constant depth and pitch. In Figure 3.19, as the groove width increases, the groove's volume becomes larger too. This way, more oil is entrapped inside the groove, because the velocity magnitude is almost zero inside the grooves and near the walls. The stationary lubricant inside the groove serves as oil-supply and improves the lubrication performance. Also, larger groove volume contributes in elongated circular paths for the lubricant, thus it prevents the oil from exiting the groove.

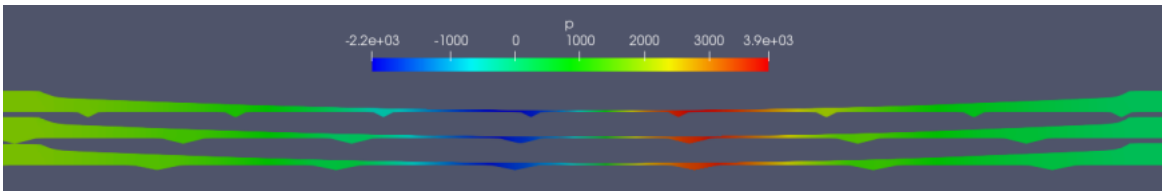

Figure 3.20: *Comparison of the pressure field between groove width* $20\mu m$*,* $40\mu m$ *and* $50\mu m$ *consequtively*

The pressure field between different groove widths with equal pitch and depth are presented in Figure 3.20. It is observed that as the groove width increases, the pressure field values decrease. Therefore, the vertical load which is applied at the top ring, is reduced with larger groove widths. It can be explained by considering the groove's volume and its influence over the lubricant's flow. The oil is moving from the inlet to the outlet of the domain, that is from right to left in Figure 3.20. The grooves with smaller width have steeper walls than the grooves with larger width. Therefore, when the lubricant enters the smaller groove, the wall's slope forces the velocity to sharply change. On the other hand, in wider grooves the velocity change is more gradual and smooth. Consequently, the slower variation of velocity contributes in lower pressure changes.

3.8.3 Varying the Groove Pitch with Constant Depth & Width

The third group of results is illustrated in Figures 3.21 & 3.22 where the change of specific friction is shown with regards to the groove pitch for specific values of groove width and depth. It is clear from Figure 3.21, that specific friction increases with the increase of groove pitch for every depth. Also, it is not highly affected by the groove depth, since the data-points with the middle and large value of depth almost coincide. This was obvious from the colour-map in Figure 3.11 too. Furthermore, the rate of change is different between the pitch intervals. Specifically, as the groove pitch increases from 121μm to 472μm, the specific friction is growing in a greater manner, when compared with the rate of change between 472μm and 1000μm data-points. Again in Figure 3.22, specific friction is shown to increase as the groove pitch increases for every width. However, the rate of change is different between the pitch intervals and greatest decrease in specific friction is found among small values of groove pitch. Also, the lowest values are achieved with the largest width option. Lastly, the specific friction variation with pitch is more sensitive to groove width than depth. This is demonstrated from the fact that small and medium width options deliver lower specific friction when compared with every depth alternative.

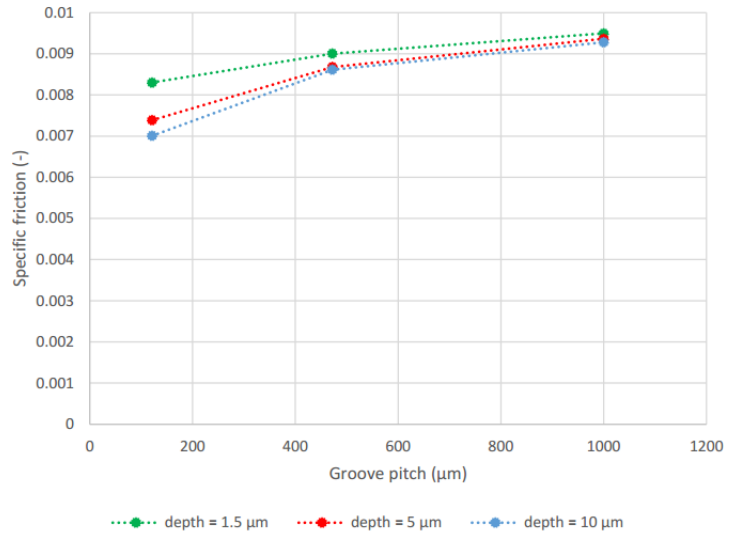

Figure 3.21: *Variation of specific friction on the top ring with regards to groove pitch for width=20µm*

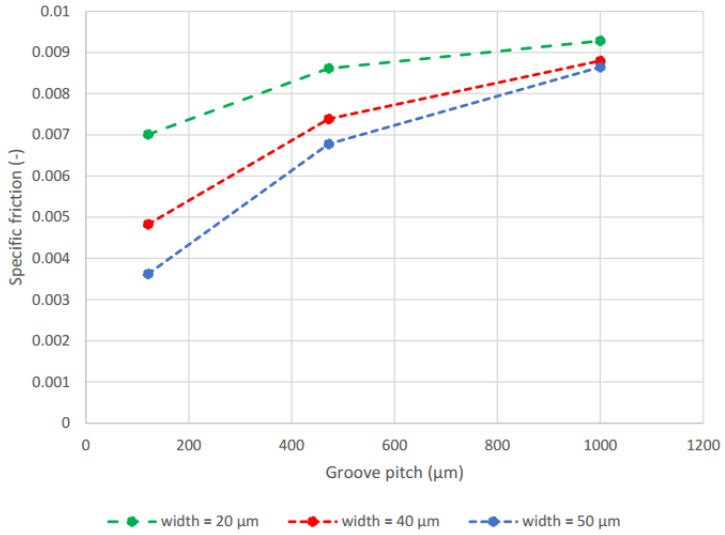

Figure 3.22: *Variation of specific friction on the top ring with regards to groove pitch for depth=1µm*

From Figures 3.21 & 3.22, it is displayed that lower specific friction can be attained with small groove pitch. This is justified by simply observing the cylinder liner surface topography with small and large groove pitch. In particular, the number of grooves present on the inner cylinder wall is larger in case of small groove pitch. Therefore, more oil can be stored inside the grooves which in turn assists in the lubrication effectiveness. The opposite is true for the large pitch.

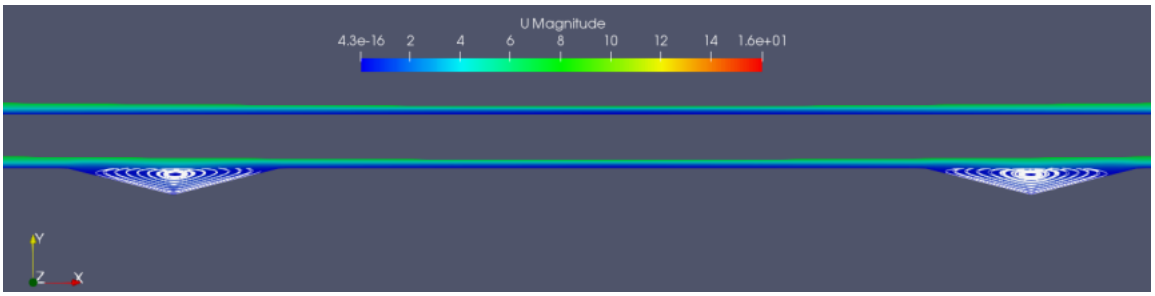

Figure 3.23: *Comparison of the streamlines inside the grooves between groove pitch* $121\mu m$ *and* $1000\mu m$

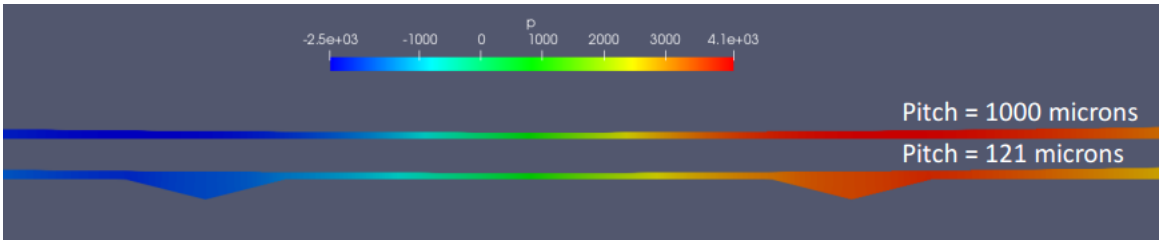

Figure 3.24: *Comparison of the pressure field between groove pitch* $121\mu m$ *and* $1000\mu m$

The pressure field between groove pitch 121μm and 1000μm with equal width and depth are presented in Figure 3.24. The grooves with pitch 1000μm are not displayed in this figure because they are wide apart with each other and didn't fit inside the picture's limits in order to be visible. It is observed that the pressure field with pitch 1000μm has larger values compared to the ones with 121μm. Thus, the vertical load applied on the top ring is expected to be larger for the case with 1000μm. In this event, increased specific friction and high vertical load lead to high friction magnitude. Since friction is opposing the lubricant's motion, with greater friction comes higher deceleration. This results in greater pressure increase which explains the reason for the high values of pressure field with groove pitch 1000μm.

3.9 Summary

In this chapter, a model for assessing the lubrication performance between the top ring and the cylinder liner has been demonstrated. The influence of the cylinder liner surface features was examined through the parametric analysis. It was discovered that lower friction can be achieved with smaller groove pitch and larger width and depth. However, greater vertical load is applied on the top ring when the cylinder liner has grooves with large pitch and small width, while the groove's depth doesn't affect the values of the pressure field but their distribution.

Chapter 4

Comparing the Fundamental Fluid-Flows with the Reynolds Equation

4.1 Introduction

The most common method for modelling the lubrication between the piston ring-pack and the cylinder liner in the automotive industry is using the mean-flow Reynolds equation. In the following sections, the Reynolds equation is derived from the Navier-Stokes PDEs and its simplifying assumptions are presented. It is suitable for describing the oil's flow in the hydrodynamic lubrication regime. Patir & Cheng [22] proposed an alternative form of the Reynolds equation which includes the flow-factors in order to simulate the mixed lubrication regime with the same equation. These serve as corrections for the oil's flow and their implementation to the mean-flow equation is further described. Alternative ways for describing surface roughness are discussed from [11], [21], [22]. For the selected method of describing the liner's surface topography, as shown in Section 1.3.4, simulations were conducted with CFD and the flow-factor results are compared with [11] for the same pressure and velocity boundary conditions.

4.2 The Reynolds Equation & its Variants

Many tribo-systems are modelled using the Reynolds equation, accompanied with suitable boundary conditions. This method is preferred because various, complex fluid phenomena[31] can be treated in a simplified manner. In particular, cavitation is simulated by modifying the boundary conditions[32], the interaction of the lubricant with the compressed gasses is considered between the piston ring-pack and the cylinder liner[33] by their mass and force equilibriums. For low Reynolds number applications, as in the case of creeping flows, the Stokes model is more appropriate[24]. In the previous chapter, the lubrication between the piston's top ring and cylinder liner was simulated by a CFD model. Both methods have their limitations and describe the lubrication mechanisms with different accuracy and specific, simplifying assumptions. In the following section, the current, reference model[11], based on the Reynolds equation, is presented.

4.2.1 The General Reynolds Equation

The Reynolds equation[6] is derived from the NS equations, as shown in Appendix **??**, for a fixed control volume(CV) in space, that extends across a lubricating film. It is formed upon the assumption that the lubricant moves only on plane $z = 0$. Regardless of the film thickness shape i.e. as shown in Figure 4.1, the motion of the upper and lower, discrete surfaces of the CV towards x, y axis are taken into consideration by their velocity vectors. The general Reynolds equation is

$$h_T\frac{\partial \rho}{\partial t} - \rho v_a\frac{\partial h_T}{\partial y} - \rho u_a\frac{\partial h_T}{\partial x} + \rho(w_a - w_b) + \frac{\partial}{\partial y}[\frac{\rho h_T(v_a + v_b)}{2}] + \frac{\partial}{\partial x}[\frac{\rho h_T(u_a + u_b)}{2}] + \frac{\partial}{\partial x}[-\frac{\rho h_T^3}{12\mu}\frac{\partial p}{\partial x}] + \frac{\partial}{\partial y}[-\frac{\rho h_T^3}{12\mu}\frac{\partial p}{\partial y}] = 0 \tag{4.1}$$

where $h_T = h_T(x, y)$ is the oil's film thickness at the examined (x, y) position, $\boldsymbol{V_a} = (u_a, v_a, w_a)$ is the velocity vector of the CV's upper surface, or the level of the film thickness and $\boldsymbol{V_b} = (u_b, v_b, w_b)$ is the velocity vector of the CV's lower surface. The variation of velocity's vertical component is expressed through the alteration of film thickness. This equation is numerically solved to acquire the pressure field as long as the oil film thickness profile is known.

The first term in equation 4.1 expresses the net flow rate due to local expansion. The second, third and fourth terms describe the net flow rates due to squeezing motion of the film thickness. The fifth and the sixth are the Couette terms and express the developed flow rates due to surface velocities. The final two are the Poiseuille terms and express the net flow rate due to pressure gradients existing in the lubricated area.

It can be concluded that the mechanisms which sufficiently describe a lubricant's flow under the Reynolds equation, are a combination of Couette and Poiseuille flows, the "squeeze" effect and the oil's local expansion, which is usually a negligible, transient mechanism of pressure generation.

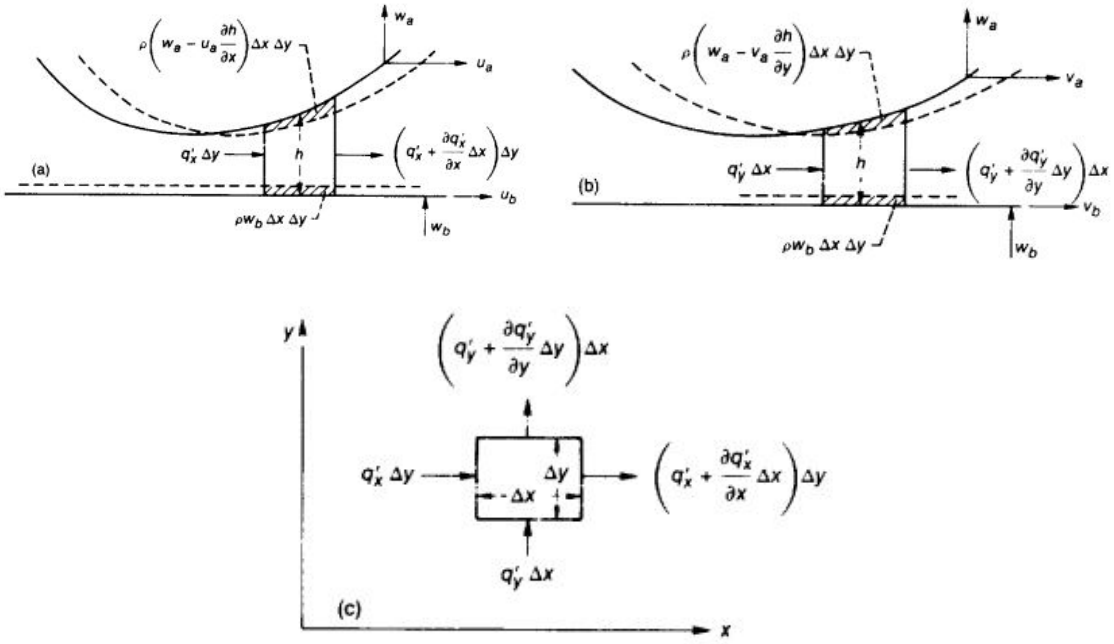

Figure 4.1: *Mass-flow q_i through the cross-section of rectangular CV where index $i = x, y$ expresses the mass-flow direction. From [34].*

The Couette terms are expanded under the simplification that the side-leakage term $\frac{\partial}{\partial y}$ is ignored and three more terms emerge

$$\frac{\partial}{\partial x}[\frac{\rho h_T(u_a + u_b)}{2}] = \frac{h_T(u_a + u_b)}{2}\frac{\partial \rho}{\partial x} + \frac{\rho h_T}{2}\frac{\partial}{\partial x}(u_a + u_b) + \frac{\rho(u_a + u_b)}{2}\frac{\partial h_T}{\partial x} \quad (4.2)$$

where the first term on the right hand side is the density wedge, the second term expresses the stretch motion of the flow and the third term represents the physical wedge of the film thickness. The density wedge denotes the pressure generation due to developing flow-rates along the axis where density variation occurs. The former two terms of equation 4.2 are further explained in the next paragraph. Generally, each wedge term has obtained its name by the phenomena that it describes. In particular, a pressure profile is generated along the flow-rate's axis of motion due to the domain's converging shape. The same is applicable to other wedge terms, but the cause of this effect may be the density variation etc.

The mechanisms, that contribute the most to the generation of the pressure field, are the physical wedge and the normal squeeze-effect. In case of the physical wedge, the

pressure build-up between a plane slider and a stationary bearing pad is displayed in Figure 4.2. The volumetric flow passing through each cross-section is dependent on the distance between the bearing and the slider, h and the velocity profile at each corresponding position. Given that the examined flow undergoes a Couette flow, the velocity profile is triangular with constant, maximum velocity equal to the slider's velocity. The distance h varies along the bearing, therefore the volumetric flow is different at each cross-section. In order to satisfy the continuity of the volumetric flow, a balancing Poiseuille flow is superimposed, which also leads to the generation of additional pressure field. The normal squeeze-effect provides a cushioning effect when two lubricated surfaces tend to be pressed together. Positive pressure is developed when the difference in surfaces' normal velocities leads to a decrease in film thickness, as shown in Figure 4.3.

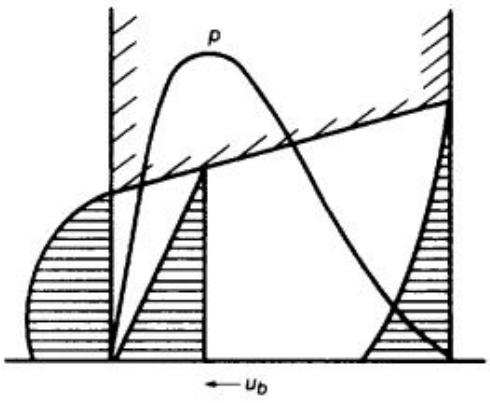

Figure 4.2: *Physical wedge from [34]*

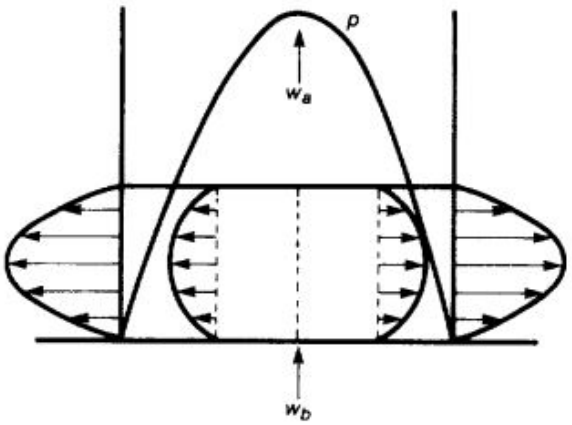

Figure 4.3: *Normal squeeze from [34]*

The derivation of the Reynolds equation is based upon the simplifying assumptions which are described in the following list:

1. The lubricant oil behaves as a Newtonian fluid.
2. Inertia forces of the lubricant are neglected.
3. Pressure is constant across the thickness of the lubricant fluid.
4. The flow is laminar.
5. The lubricant's viscosity is held constant.
6. No-slip condition is employed on the fluid-wall interfaces.
7. External body forces acting on the fluid film are neglected.

It has become evident, that the applicability of Reynolds equation to the investigated tribo-system is limited to flows with low Reynolds number, in which the viscous forces dominate over the inertia forces. For most lubrication problems, the

Reynolds number is calculated by equation 3.4. In this form, the Reynolds number is used for characterizing the flow regime as laminar or turbulent, given that its value is above one[24]. On the other hand, if its value is below one, there is no specific criterion that assesses the suitability of Reynolds equation for the problem under investigation. Also, further attention must be given for not confusing the case of a creeping flow with a case to which the Reynolds equation is relevant. Consequently, for distinguishing between creeping flows and non-creeping flows, another non-dimensional number is used, namely the reduced Reynolds number[24]

$$Re^* = Re \cdot \frac{h_T}{L} \tag{4.3}$$

where L is the length for one of the intersecting walls. If $0.001 < Re^* < 0.1$, then the convective, inertia forces can be ignored and the pressure can be assumed as constant towards z axis, therefore the Reynolds equation can be used for describing the examined flow.

An alternative criterion for checking the applicability of the Reynolds equation in tribo-systems, where macro-roughness influence is investigated, is based on the geometric characteristics of the surface roughness. Assuming that the surface roughness is described by a simplified, continuous profile of consecutive, alternating valleys and hills, then it is characterized by two parameters, namely the dimple spacing, λ and the peak to bottom distance, c as shown in Figure 4.4. Providing that the film thickness h_T is known for the investigated geometry, it is examined whether $h_T \ll \lambda$. If the comparison is validated, then the Re^* belongs to the acceptable range for using the Reynolds equation. For the opposite case, where the film thickness is greater than the dimple spacing, another set of equations should be used for acquiring the oil's flow field. Earlier, it was shown that the lubrication regime is hydrodynamic in the examined application.

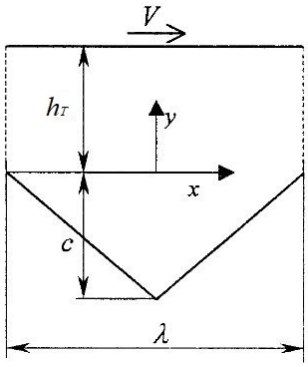

Figure 4.4: *Geometry of 2-dimensional, triangular macro-roughness*

4.2.2 Reference Model

In the automotive industry, the lubrication modelling between two rough surfaces in relative motion is usually built upon the proposal of Patir & Cheng[22]. Its novelty is associated with the model's ability to simulate the oil's flow, using the Reynolds equation over 3-D, rough surfaces and its potential to be applied for simulating the oil's behaviour in partial lubrication regime. One important aspect is that each surface is expressed by its roughness head readings, or is generated using stochastic methods with known statistical properties. Therefore, it is possible to account for the influence of the realistic surfaces features to the oil's mean flow field. Since [22], many variations of their model have been presented [32], [35], [36]. Each of them tackles one, or more, additional problems for multiple applications, in order to simulate with greater accuracy the lubricant's behaviour and express qualitatively the complex, undergoing phenomena.

To determine the pressure field between two lubricated surfaces, that move relatively to each other with velocities U_1 and U_2, respectively, along the longitudinal direction, the unsteady Reynolds equation for an isothermal, incompressible lubricant is solved

$$\frac{\partial}{\partial x}\left(\frac{h_T^3}{12\mu}\frac{\partial p}{\partial x}\right) + \frac{\partial}{\partial y}\left(\frac{h_T^3}{12\mu}\frac{\partial p}{\partial y}\right) = \frac{(U_1 + U_2)}{2}\frac{\partial h_T}{\partial x} + \frac{\partial h_T}{\partial t} \tag{4.4}$$

where $h_T = h + \delta_1 + \delta_2$ is the oil film thickness, h is the nominal distance between the mean levels of the lubricated surfaces, δ_1 and δ_2 are the random roughness amplitudes of the two surfaces as depicted in Figure 4.5. In [22], the surface roughness is generated by stochastic methods and follow a Gaussian distribution, having zero mean value and standard deviations σ_1, σ_2 respectively. Therefore, the standard deviation of the combined roughness $\delta = \delta_1 + \delta_2$ is $\sigma^2 = \sigma_1^2 + \sigma_2^2$.

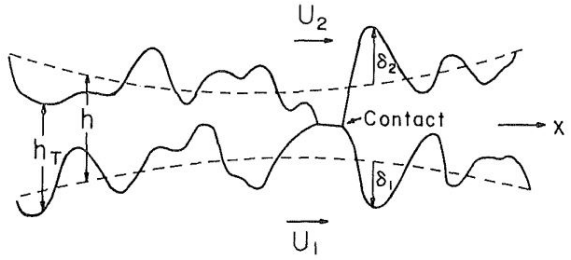

Figure 4.5: *Rough surfaces moving relatively to each other. From [22].*

Another important aspect for modelling rough surfaces as shown in Figure 4.5, is the ratio $\frac{h}{\sigma}$, which can be used for identifying the lubrication regime. For $\frac{h}{\sigma} \ll 3$ [22], the roughness effects are negligible and the Reynolds equation in the current form is sufficiently accurate for modelling the hydrodynamic lubrication regime. This is not the case when $\frac{h}{\sigma}$ approaches to 3; then the roughness effects become important. Further decrease in this ratio implies partial, or mixed, lubrication between

the surfaces, where asperity interaction and contact are present. In this case, additional measures[37] are taken, when using the Reynolds equation for calculating the lubricant's flow field more accurately.

As seen in Figure 4.5, two length scales are introduced. The first is related with the geometry of the interacting components which is expressed in mm. The second is associated with the surface roughness of each element and is usually described in μm. The difference in their order of magnitude requires great spatial resolution for numerically solving equation 4.4. This situation frequently hinders from performing unsteady simulations due to large computational time or data storage. This problem is solved by introducing to equation 4.4 the flow-factors. These indicate the influence of surface roughness over the lubricant's flow. In detail, they express the portion of the lubricant which is entrapped inside the valleys of each rough surface and follow the respective surface's motion.

The flow-factors serve as corrections for the Reynolds equation and filter the volumetric flow between two lubricated surfaces according to their roughness. Then, the resultant mean pressure field is computed by the "corrected" Reynolds equation under appropriate boundary conditions. The acquired pressure field is characterized as "mean", since it doesn't consider the local flow phenomena inside the valleys of each surface's roughness. For the case of one moving surface with velocity U in the positive x direction, on top of a stationary surface and with a pressure difference applied towards the same direction, the corrected Reynolds equation[22] is

$$\frac{\partial}{\partial x}(-\phi_x \frac{h_T^3}{12\eta}\frac{\partial \overline{p}}{\partial x} + \phi_s \frac{h_T U}{2}) + \frac{\partial h_T}{\partial t} = 0 \tag{4.5}$$

where ϕ_x is the pressure flow-factor that compares the pressure-driven flow between two rough surfaces to that of a pair of smooth surfaces, $\overline{p}$ is the mean pressure field and ϕ_s represents the additional flow transport due to sliding between two rough surfaces. In this form, the Reynolds equation can be used for simulating more accurately the developed flow field in the partial lubrication regime.

The adjustment of generated forces is essential to comply with the mass-flow correction. For that purpose, the shear stress factors[21] are recommended which are defined in such way that the mean hydrodynamic stress is computed by the mean quantities as

$$\overline{\tau} = \phi_{fs}\frac{\mu U}{h} - \phi_{fp}\frac{h}{2}\frac{\partial \overline{p}}{\partial x} \tag{4.6}$$

where $\overline{\tau}$ is the mean shear-stress which is applied at the moving top wall, ϕ_{fs} is the shear stress-factor which expresses the influence of surface roughness over the stresses caused by the velocity-driven component of the examined flow, ϕ_{fp} is the pressure stress-factor which quantifies the impact of roughness over the stresses generated by the pressure-driven component.

In general, the stress-factors are defined by

$$\phi_{fi} = \frac{F_{x,real}}{F_{x,flat//plates}} \tag{4.7}$$

where the index $i = s$ corresponds to the Couette term of the flow and $i = p$ to the Poiseuille term, x is the moving pair's axis of motion and F_x is the friction force opposing the pair's relative motion. Hence, $F_{x,flat//plates}$ is computed by the Couette and Poiseuille flows' expressions and $F_{x,real}$ is calculated for the pair of rough flat-plates with the same vertical distance and boundary conditions as in the fundamental fluid flows for various roughness configurations.

The values of the flow-factors and stress-factors are specific to each application. The generality of the corrected Reynolds equation relies upon the way that these factors are computed. For roughness profiles generated by random Gaussian distributions with known statistical moments, these should be computed, at least, for ten different random distributions with the same statical moments. Then, their average values are calculated and used as the final flow and stress factors in the Reynolds equation.

The major advantage of this method stems from the ability to compute the flow-factors for any surface topography features. For different features of roughness, the flow-factors are expressed as functions of the surface roughness characteristics i.e. $\phi_i = f(\frac{h}{\sigma})$. After interpolating the data, it is possible to find the flow-factors without executing the above mentioned, tedious process. Therefore it is possible to assess the lubrication performance for any type of surface roughness, that belongs within the simulated range using the mean-flow Reynolds equation.

A model was developed by Toyota Motor Corporation (TMC)[11] for the piston ring-pack and the cylinder bore, which is based on [21], [22]. The innovative features of [11] are related with the surface roughness description of the cylinder liner and the computational solution of the mean-flow Reynolds equation. In particular, the liner's roughness accounts for the groove width, depth, hatch angle and directional properties[38], while the ring-pack surfaces are assumed smooth. As far as the solution of Reynolds equation is concerned, cavitation boundary condition is applied to the side of the combustion chamber and the entire operation cycle of the cylinder is examined. Thereby, the friction, or friction mean effective pressure (FMEP) opposing the piston and ring-pack motion is computed and compared with experimental measurements. In [11], good correlation is achieved between experimental and numerical FMEP for light loads and small engine rotational speed. However, as the engine load and rotational speed increase, larger deviation is observed.

4.3 Flat Plate on Grooved Cylinder Wall

In the following section, an alternative method is presented for computing the flow-factors with CFD instead of solving the 2-D Reynolds equation. Since, the flow-factors are calculated based on the equivalent Couette and Poiseuille flows between rough surfaces, the top ring is treated as a horizontal surface for the examined application. Also, considering that each flow-factor is defined by the fraction of the rough surfaces' volumetric flow divided by the smooth surfaces' volumetric flow in the same conditions, these are independent of the cylinder's simulated area. For this reason, the entire cylinder stroke is not simulated. In detail, only a segment of the cylinder wall is selected so that it includes at least two parallel or crossing grooves.

4.3.1 Geometry

The geometry comprises of a flat plate located on top of the grooved surface of the cylinder liner at a distance h, as shown in Figure 4.6, where the distance h is measured from the base of each triangular groove until the top wall.

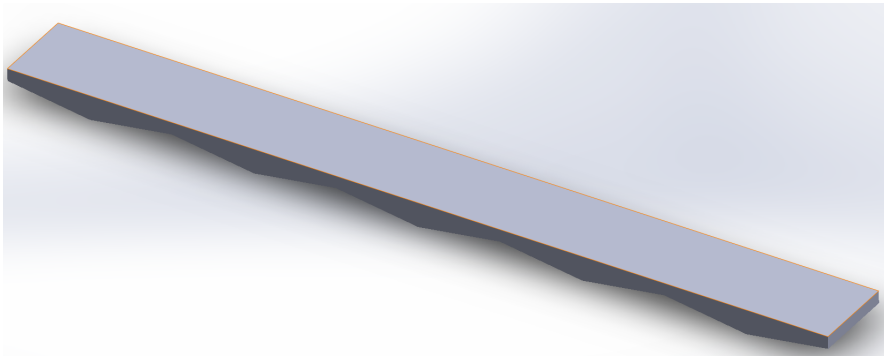

Figure 4.6: *Flat-plate on grooved cylinder wall for hatch angle 0^o, groove depth 2 μm, groove width and pitch 20 μm.*

Three different sets of geometries were examined based on varying geometric characteristics of the cylinder liner. Initially, they were divided by their hatch angles. The first group comprises of grooved surfaces with 0^o cross-hatch angle as illustrated in Figure 4.6, the second with 30^o and the third with 150^o as shown in Figure 4.7. Then, each group was simulated with groove pitch 472μm and for the case of 0^o hatch angle with groove width=20μm equal to groove pitch. The groove width was set as 20μm and the depth as 1.5μm. The alternative features of surface roughness are summarized in Table 4.1. The scope of this investigation was to extract a relationship between the flow-factors and the non-dimensional parameter $\frac{h}{D}$ where D is the groove depth. For that reason, the vertical distance between the plates varies according to the fraction's value so as $\frac{h}{D} \in [1, 10]$ with $D = 1.5\mu$m.

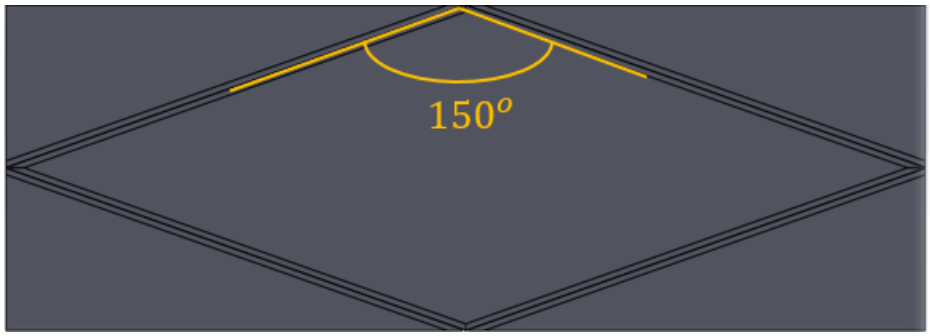

Figure 4.7: *Flat-plate on grooved cylinder wall for hatch angle* 150^o*, groove depth 1.5* μm*, width 20* μm *and pitch 472*μm*.*

Cross-hatch angle	**0°**	**30°**	**150°**
Pitch μ**m**	20, 472	472	472
Depth μ**m**	1.5	1.5	1.5
Width μ**m**	20	20	20

Table 4.1: *Examinded combinations of surface roughness.*

The boundaries of the computational domain were named according to their position or physical properties and are summarized in Table 4.2. In particular, the top, moving wall was named top patch as shown in Figure 4.8 and the bottom, stationary, grooved wall was named grooved patch as shown in Figure 4.9. The remaining boundaries of the rectangular domain are depicted in the same figures. The same names are used for presenting the simulations' results at each surface of interest.

Name	**Explanation**
top	Top, moving wall
grooved	Stationary, grooved cylinder liner
inlet	Vertical section of the domain, normal to the longitudinal axis
outlet	Vertical section of the domain, normal to the longitudinal axis
front	Longitudinal section of the domain (front side)
back	Longitudinal section of the domain(rear side)

Table 4.2: *The boundaries of the rectangular domain between the flat and the grooved plate.*

4.3.2 Boundary Conditions

The shear flow-factor calculation requires the mass-flow between the pair of flat and rough plates, where one of them is moving. This type of flow follows the principles of Couette flow whose boundary conditions were described in Section 2.3.3. Therefore, the applied boundary conditions are summarized in Table 4.3 and are shown in

Figure 4.8. Also, the pressure flow-factor needs the mass-flow between the same pair but in case of the pressure-driven flow, namely Poiseuille. For this type of flow, its boundary conditions are listed in Table 4.4 which are applied to the investigated geometry as shown in Figure 4.9.

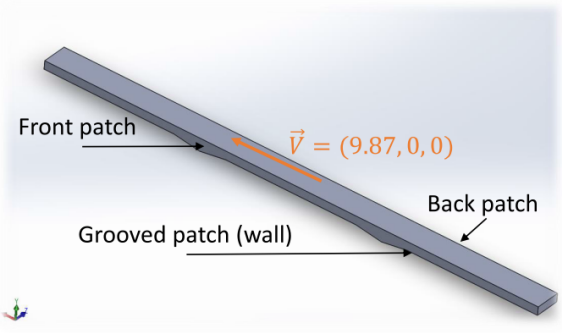

Figure 4.8: *Flat-plate on grooved cylinder wall, near top view.*

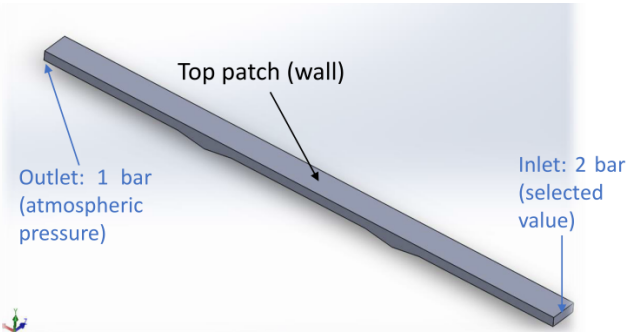

Figure 4.9: *Flat-plate on grooved cylinder wall, near bottom view.*

Boundary	Velocity	Pressure
top	Dirichlet $\vec{V} = (9.87, 0, 0)$	zero Neumann
grooved	zero Dirichlet	zero Neumann
inlet	zero Neumann	Dirichlet $p = 1bar$
outlet	zero Neumann	Dirichlet $p = 1bar$
front	Periodic	Periodic
back	Periodic	Periodic

Table 4.3: *Couette boundary conditions for pressure and velocity for the pair of flat and grooved surfaces.*

Boundary	Velocity	Pressure
top	zero Dirichlet	zero Neumann
grooved	zero Dirichlet	zero Neumann
inlet	zero Neumann	Dirichlet $p = 1bar$
outlet	zero Neumann	Dirichlet $p = 2bar$
front	Periodic	Periodic
back	Periodic	Periodic

Table 4.4: *Poiseuille boundary conditions for pressure and velocity for the pair of flat and grooved surfaces.*

4.3.3 Couette Flow Results

The Couette flow simulations converged fast but their results were sensitive to the mesh quality. For this reason, especially for the cases where $\frac{h}{D} < 3$, grid dependency studies were conducted. The results of the shear flow-factor with regards to $\frac{h}{D}$ for hatch angle 0^o are shown in Figure 4.10 for alternative groove width and pitch. It is worth mentioning that during the flow-factor calculation, the distance between the smooth flat-plates plays an important role. This was determined by assuming that the pair of smooth flat-plates occupies the same volume as the pair of rough plates.

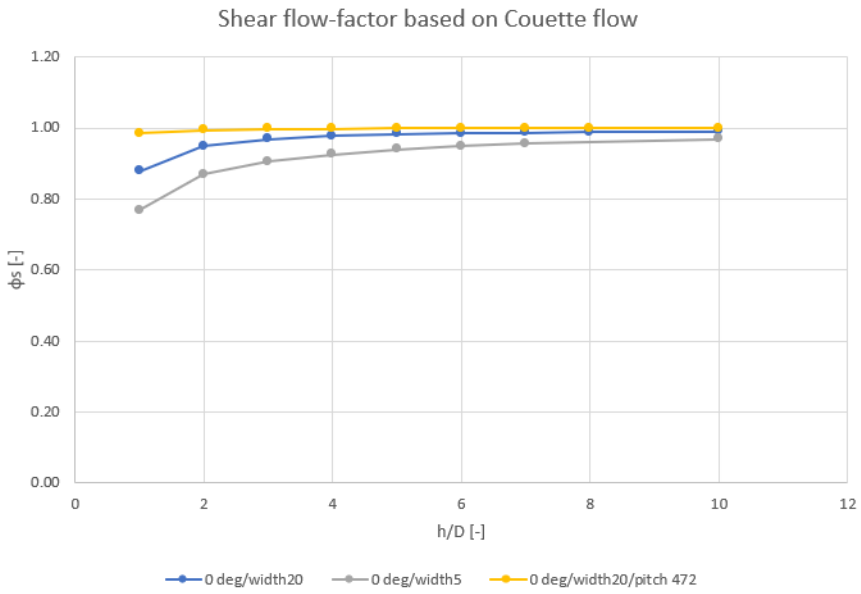

Figure 4.10: *Shear flow-factor with regards to* $\frac{h}{D}$ *for hatch angle* 0^o *and different groove width & pitch.*

In Figure 4.10, it is observed that as the distance between the pair of plates increases, the shear flow-factor increases too for every combination of surface roughness. Shear flow-factor values near to one mean that the surface topography doesn't affect the lubricant's flow between the pair of rough plates, thus it is similar to the pair of smooth plates. However, when the distance between the plates is equal or close to the groove depth, the oil's flow is affected by the surface roughness as demonstrated by the flow-factor reduction. There is greater flow-factor reduction in small values of $\frac{h}{D}$ as the groove pitch decreases. Shear flow-factor values below one indicate that a portion of the lubricant's mass is entrapped inside the grooves and cannot exit the examined flow-field since the rough wall is stationary.

The shear flow-factor reduction with groove pitch decrease is justified by observing the fields of velocity magnitude which are shown in Figure 4.11.

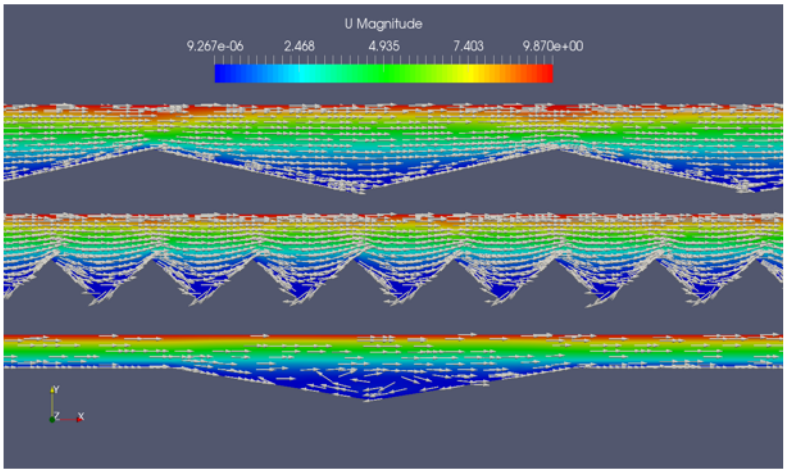

Figure 4.11: *Field of velocity magnitude for different groove widths and hatch angle* 0^o*. From top to bottom width=*$20\mu m$*,* $5\mu m$ *equal to pitch and at last* $(width, pitch) = (20, 472)$ *in* μm*.*

Firstly, fewer grooves are engraved on the rough wall with large groove pitch. Thus, the available volume for confining the lubricant is depleted and the flow is more likely to resemble the ideal Couette flow. In the same figure, it is also clear that greater fluid recirculation is present with small groove widths. Therefore, it is harder for the lubricant to exit the groove which leads to lower mass-flow than the one between the smooth pair.

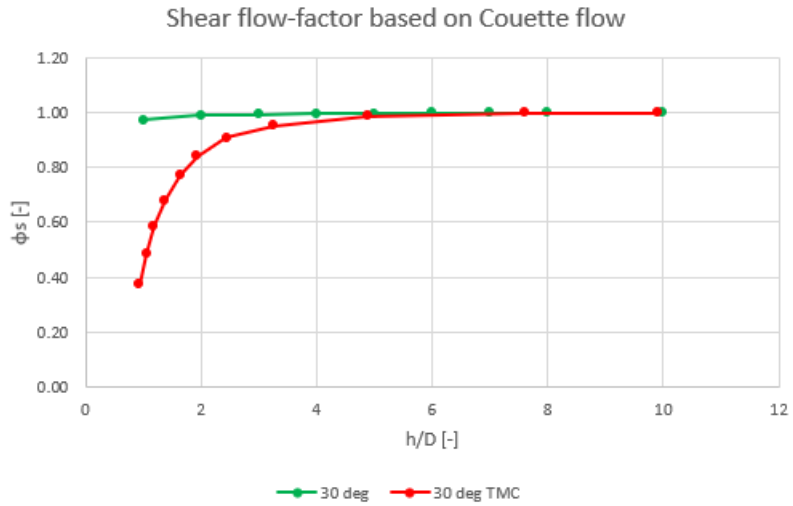

Figure 4.12: *Comparison of shear flow-factor for hatch angle* 30^o *between CFD and [11].*

The shear flow-factor results are presented in Figure 4.12 for hatch angle 30^o with regards to $\frac{h}{D}$ and are compared with the equivalent ones from [11]. Total correlation is achieved for $\frac{h}{D} > 5$, since the simulated flow is similar to the ideal Couette flow.

Nonetheless, great deviation is noticed as the distance between the plates decreases. In particular, $\phi_{s,CFD} = 2\phi_{s,TMC}$ for the lowest value of $\frac{h}{D} = 1$. The flow-factors from [11] are computed by numerically solving the 2-D Reynolds equation where the lubricant is assumed not to move in the vertical direction. This simplifying assumption is not validated from the 3-D CFD flow-fields. In Figure 4.13, the vertical component of velocity U_y is illustrated. It is discovered that U_y near the edges of the grooves is not zero and is comparable with the streamwise velocity component U_x. Furthermore, in the examined geometry, $L_x < L_z$ where z is the lateral direction of motion. Consequently, most of the crossing grooves' length belongs to the lateral direction of motion and is impeding the lubricant's motion towards x'x. This remark along with the previously mentioned assumption contribute in severely lower values of the flow-factors than the ones that were computed by CFD.

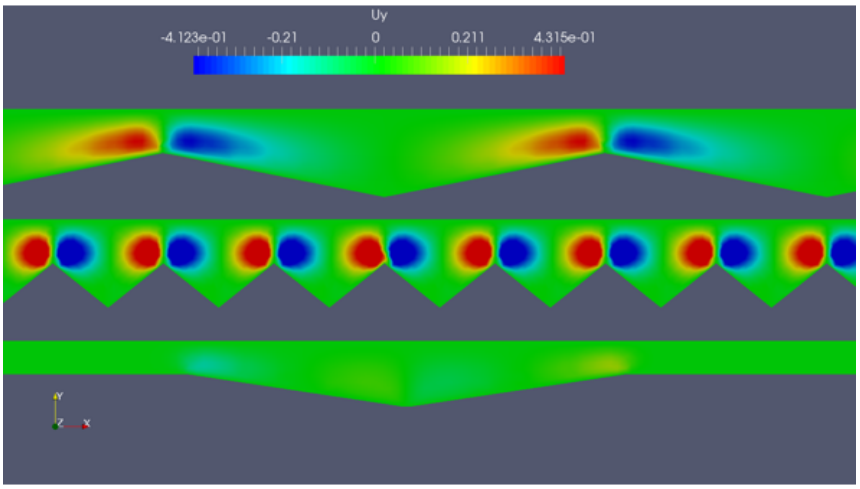

Figure 4.13: *The velocity field for U_y component with $h = D$, width=20μm, 5μm equal to pitch and at last $(width, pitch) = (20, 472)$ in μm.*

It is interesting to observe the variation of shear flow-factors for hatch angle 150^o between CFD and [11] which are depicted in Figure 4.14. The data-points between alternative methods almost coincide with each other. This is related with the length's relationship where $L_x > L_z$ and the length of the crossing grooves is towards the streamwise direction. Therefore, the resultant flow-field is expected to be similar to the ideal Couette-flow. There is a small deviation in case of $h = D$. It can be justified by considering that the lubricant is not moving perpendicular to xz plane for the flow-factors which are calculated by the Reynold equation. Therefore, the oil that enters the groove, remains trapped inside it until the simulation completion. For this reason, the difference between the mass-flow passing through the rough plates for CFD and for 2-D Reynolds equation is expected to be equal with the lubricant's mass-flow which is enclosed by the grooves.

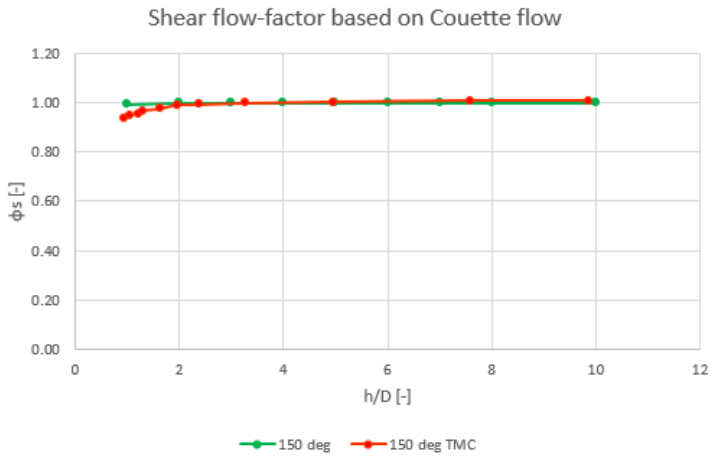

Figure 4.14: *Comparison of shear flow-factor for hatch angle* 150^o *between CFD and [11].*

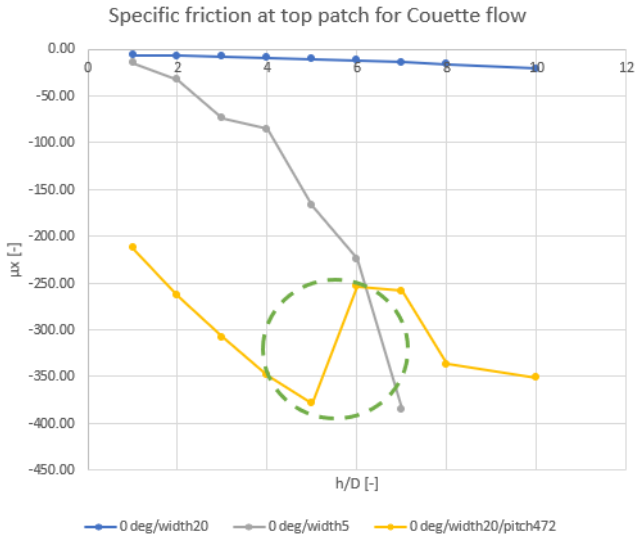

Figure 4.15: *Specific friction at the top wall with regards to* $\frac{h}{D}$ *for width=*$20\mu m$*,* $5\mu m$ *equal to pitch and* $(width, pitch) = (20, 472)$ *in* μm*.*

The specific friction with regards to $\frac{h}{D}$ for hatch angle 0^o and alternative groove (width, pitch) is presented in Figure 4.15. Normally, the absolute values of specific friction are below one. This is not relevant to the current diagram because the normal force F_y which is computed by the integral of pressure over the surface of interest, is very low. It is common in Couette flows for the pressure field to be constant and equal to the pressure values of the domain's inlet and outlet. This is obvious for the roughness features with width=pitch=5μm and (width, pitch)=(20, 472) in μm. However, for the alternative with width=pitch=20 μm, the absolute specific friction is below one. Hence, it is concluded that the resultant pressure field is not constant along the domain's length with grooves of sufficient volume. This is

not applicable to the scenario with width=pitch=5μm, because the groove's volume is very small. In the same figure, the sudden increase in specific friction is circled for the alternative with (width, pitch)=(20, 472) in μm. This abrupt variation is caused by the low values of vertical load F_y, since in Figure 4.16 the friction force constantly increases with the increase of $\frac{h}{D}$. Lastly, it is clear that the specific friction decreases with increasing distance between the pair of plates.

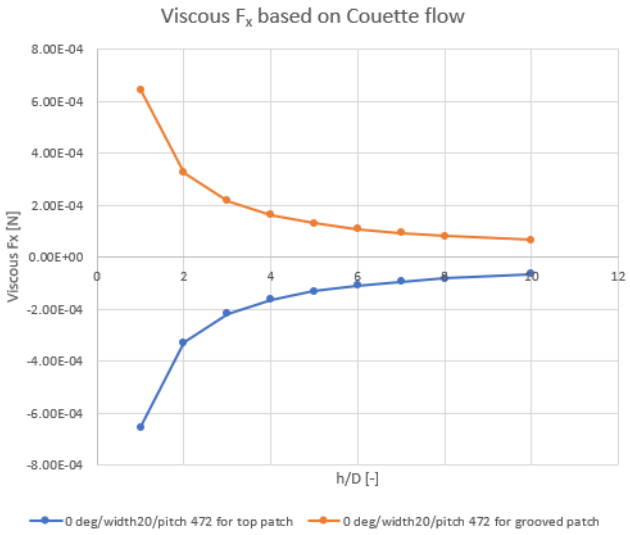

Figure 4.16: *Viscous force component F_x at the top wall with regards to $\frac{h}{D}$ for $(width, pitch) = (20, 472)$ in μm and hatch angle 0^o.*

4.3.4 Poiseuille Flow Results

The Poiseuille flow simulations weren't sensitive to the mesh quality, though fine tuning of the solution controls was necessary in order to achieve convergence. The pressure flow-factors were computed for hatch angle 0^o with different groove (width, pitch) as shown in Figure 4.17. It is noticed that the pressure flow-factor increases with the increase of $\frac{h}{D}$. Also, the rate of increase is greater for $\frac{h}{D} < 4$. In the opposite case, the flow-factor is slowly increasing in a linear manner until its value becomes almost one. Since the distance between the rough plates increases, the surface roughness influence is reduced and the resultant flow is similar to the flow between the smooth plates. However, for the alternative with (width, pitch)=(20, 472) in μm, the flow-factor remains close to one for every value of $\frac{h}{D}$. This was to be expected since the roughness profile includes the largest pitch value. In particular, as the groove pitch increases and the number of grooves decreases, it is anticipated for the flow between rough plates to be similar with the ideal Poiseuille flow which leads to flow-factor near one. Furthermore, the pressure flow-factor values decrease as the groove width is reduced.

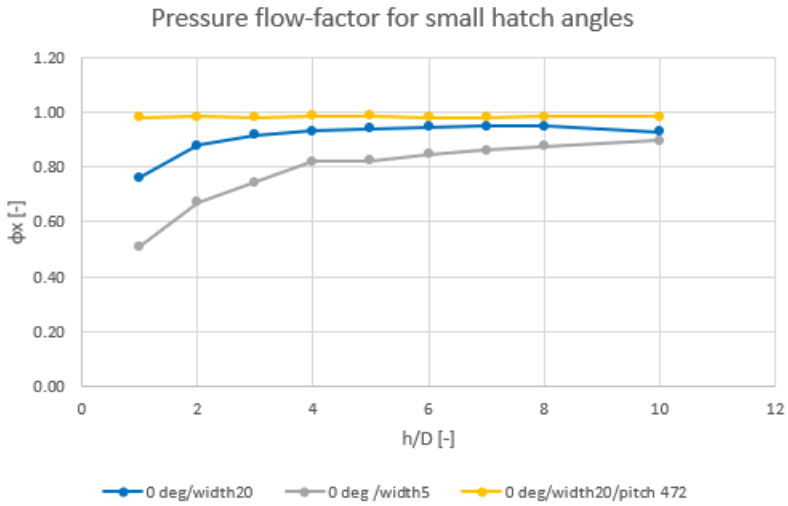

Figure 4.17: *Pressure flow-factor with regards to* $\frac{h}{D}$ *for hatch angle* 0^o *and different groove width & pitch.*

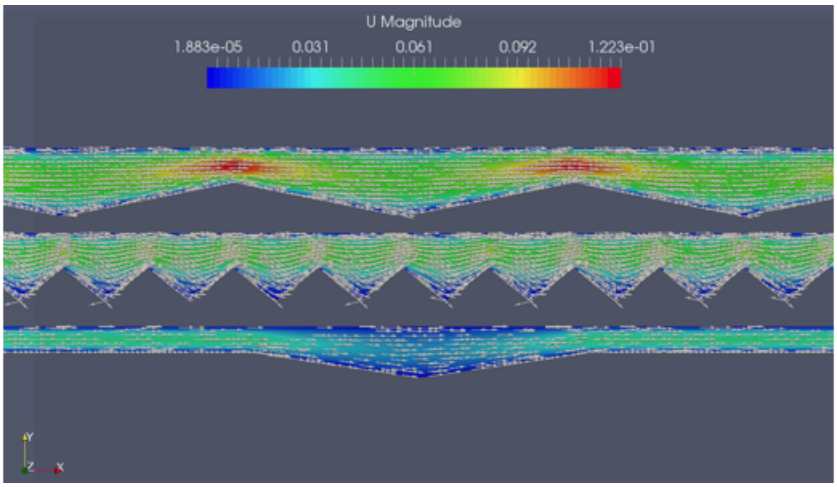

Figure 4.18: *Field of velocity magnitude for hatch angle* 0^o *and* $h = D$*. From top to bottom width=*$20\mu m$*,* $5\mu m$ *equal to pitch and at last* $(width, pitch) = (20, 472)$ *in* μm*.*

The pressure flow-factor decrease with smaller pitch and width can be explained by observing the velocity field in Figure 4.18. Firstly, as it was mentioned earlier, fewer grooves are present for large values of groove pitch, thus lesser oil is entrapped inside the grooves and the resultant flow-field resembles the ideal Poiseuille flow, hence the pressure flow-factors are close to one. As seen in Figure 4.18, the flow recirculation is greater with decreased groove width. Therefore, the lubricant that enters the grooves with smaller width gets trapped inside them and cannot exit the groove's volume. This effect contributes in reduced value for the pressure flow-factor. Additionally, as the groove width increases, the flow is observed to accelerate more towards the streamwise direction. This remark, depending on the flow conditions, may justify pressure flow-factors with values above one.

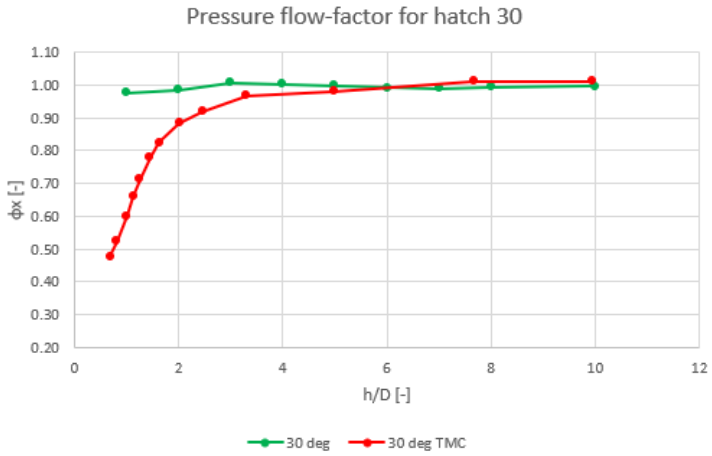

Figure 4.19: *Comparison of pressure flow-factor for hatch angle* 30^o *between CFD and [11].*

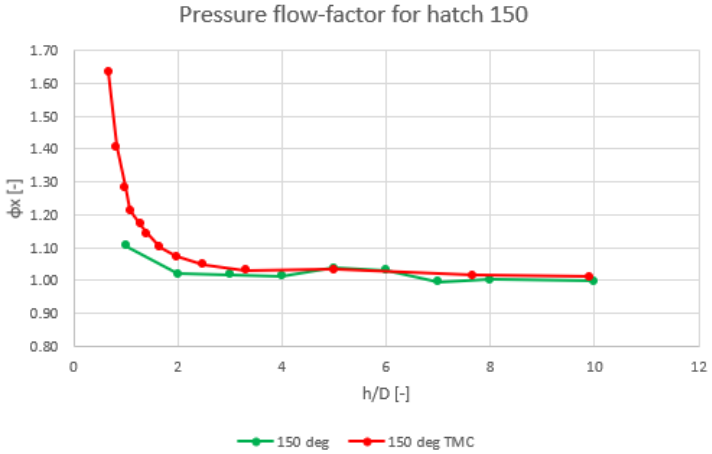

Figure 4.20: *Comparison of pressure flow-factor for hatch angle* 150^o *between CFD and [11].*

The results of pressure flow-factor for hatch angle 30^o with regards to $\frac{h}{D}$ are displayed in Figure 4.19. They are compared with the ones that were computed from [11]. In particular, total correlation is achieved for $\frac{h}{D} \geq 5$ where the distance between the pair of plates is large and the resultant flow closely resembles the ideal Poiseuille. However, large deviation is noticed for $\frac{h}{D} < 5$ and is increasing as the distance between the plates is reduced. This can be attributed to three reasons. Firstly, the computational model of [11] does not account for the influence of groove pitch. Secondly, $L_x < L_z$, thus the groove's length is towards the lateral direction of motion and is restraining the lubricant's acceleration towards the streamwise direction. Thirdly, in [11] the lubricant is assumed not to move along the vertical axis. This simplifying assumption is not verified by the 3-D CFD simulations. In detail, the field of vertical velocity component U_y is shown in Figure 4.22 and its values are comparable with the streamwise velocity component U_x which is presented in Figure

4.21. By combining the last two reasons, it is deduced that in [11] the oil enters the grooves, it fills the groove's volume and the remaining oil is moving between the top flat-plate and the generated, stationary oil film above the grooves.

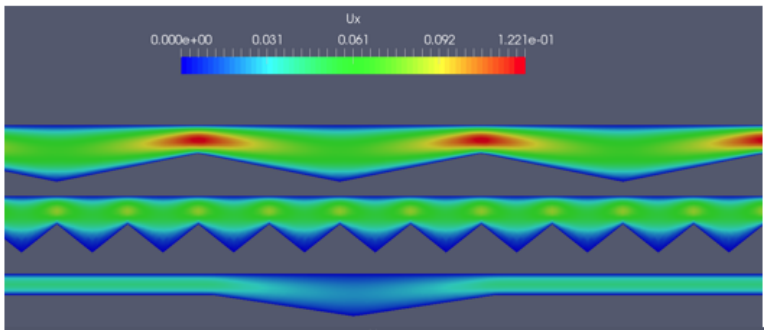

Figure 4.21: *The velocity field for U_x component with width=20μm, 5μm equal to pitch and at last $(width, pitch) = (20, 472)$ in μm.*

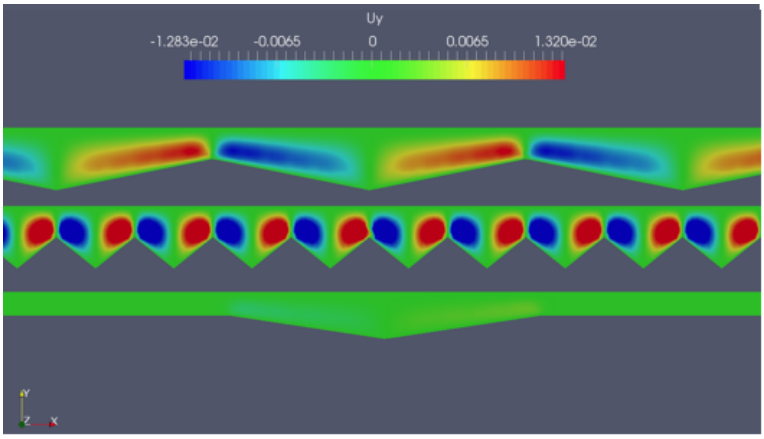

Figure 4.22: *The velocity field for U_y component with width=20μm, 5μm equal to pitch and at last $(width, pitch) = (20, 472)$ in μm.*

The pressure flow-factors for hatch angle 150^o are compared between 3-D CFD and [11] in Figure 4.20. Their results almost coincide with each other for $\frac{h}{D} \geq 3$, because the groove's length is towards the streamwise direction, $L_x > L_z$. Thus, the directional properties of roughness don't hinder the lubricant's flow, hence the resultant flow resembles the ideal Poiseuille and the pressure flow-factors are near one. In the opposite side where $\frac{h}{D} < 3$, larger deviation is observed between the flow-factors computed from CFD and [11]. Also, in the same area of the diagram, the pressure flow-factors are above one and further increase as the distance between the pair of plates is decreased. This remark can be explained by observing the field of streamwise velocity component in Figure 4.21. In more detail, it is detected that the lubricant' flow is accelerating towards the streamwise direction at the grooves' edges. The increase of velocity is greater for large groove width and many grooves.

Also, its maximum value is displayed as greater than the maximum velocity of the ideal Poiseuille flow. Therefore, the resultant parabolic profile of velocity has larger maximum value compared to the Poiseuille one which contributes in greater mass-flow between the rough plates than the mass-flow between smooth plates.

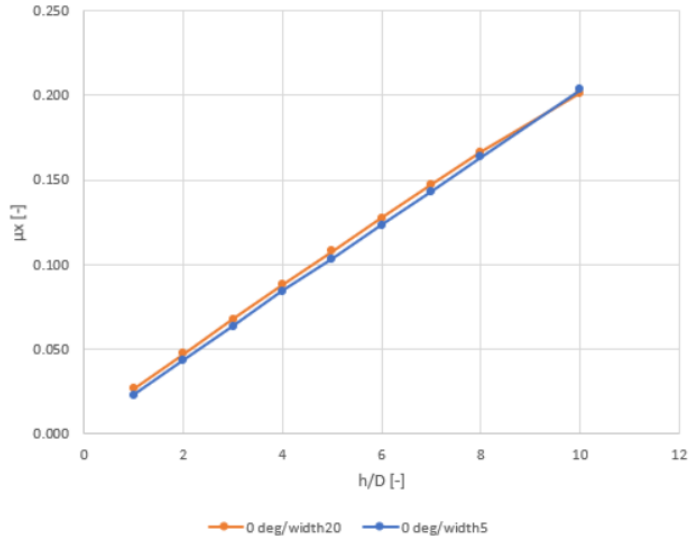

Figure 4.23: *Specific friction at the top wall with regards to* $\frac{h}{D}$ *for width=*$20\mu m$*,* $5\mu m$ *equal to pitch.*

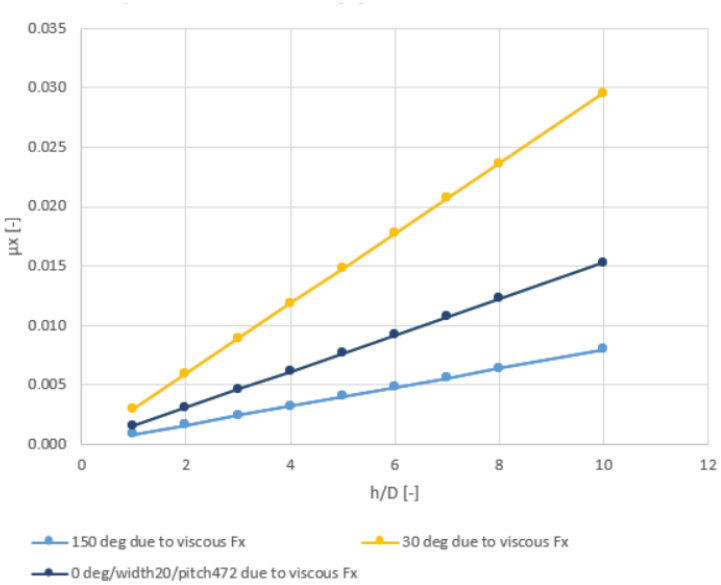

Figure 4.24: *Specific friction at the top wall with regards to* $\frac{h}{D}$ *for hatch angles* $0^o, 30^o$ *&* 150^o*, width=*$20\mu m$ *and pitch=*$472\mu m$*.*

The variation of specific friction with regards to $\frac{h}{D}$ for hatch angle 0^o is presented in Figure 4.23 with different groove widths equal to groove pitch. It is demonstrated

that specific friction increases with the increase of distance between the pair of rough plates in a linear manner. Also, the rate of change is almost the same for alternative groove widths. The results of specific friction for groove pitch=472μm are shown in Figure 4.24 and were separated from Figure 4.23, because they are lower than the specific friction for hatch angle 0^o. In particular, the variation of specific friction with regards to $\frac{h}{D}$ is illustrated in Figure 4.24 for alternative hatch angles. Again, specific friction increases in a linear manner with the increase of $\frac{h}{D}$. However, the rate of change is different depending on the surface's hatch angle. Specifically, as the hatch angle increases, the rate of specific friction increase is reduced.

From Figures 4.23 & 4.24, in pressure-driven flows is concluded that lower specific friction is achieved with grooved surfaces where crossing grooves are present, or hatch angle is greater than zero. Also, the variation of specific friction with the distance between the pair of rough plates is lower with large hatch angle values.

4.4 Conclusions - Summary

Remarks on the mean-flow Reynolds equation

The investigation of surface roughness influence in macro-scale where every engine component operates, is a complex task. It requires sufficient handling of the parts' geometry, the transient operation of the engine cylinders, the undergoing fluid-phenomena during its cycle etc. These alone are difficult to combine in a single computational model. By adding the detailed form of surface roughness from experimental measurements or stochastic methods in the component's geometry, the model's complexity and computational requirements would render it impossible to perform. For this reason, the mean-flow Reynolds equation is used where the impact of roughness in meso-scale is treated separately from the effect of geometry/engine movement and their resultant fluid-phenomena. Even though the accuracy of this method is lower compared to CFD, it has already been shown in Section 3.3 that it is computationally expensive to perform unsteady CFD simulations with detailed surface roughness on the examined piston ring-pack & cylinder assembly. By utilizing the mean-flow Reynolds equation, it is possible to calculate the friction opposing the piston's motion during the entire engine cycle. These results can be compared with equivalent experimental data in order to further tune the mean-flow modelling parameters or the flow-factor computation, thus improve the accuracy of this simplified model.

Remarks on using the Reynolds equation for calculating the flow-factors

In this chapter, an alternative method was examined for calculating the flow-factors by numerically solving the Couette and Poiseuille flows between rough plates with CFD. The resultant pressure and shear flow-factors were compared with the equiv-

alent ones from [11]. Firstly, it was observed that both flow-factors decrease as the distance between the pair of plates is reduced and as the groove width and pitch is decreased. Good correlation was achieved between the flow-factors that were computed from [11] and CFD for $\frac{h}{D} \geq 4$. However, greater deviation is demonstrated among them as the pair's vertical distance approaches the value of groove depth. Further attention should be paid concerning the validity of Reynolds equation in this type of geometries, since it relies upon the Reynolds number and the surface topography[39]. Also, the simulated flow-factors are greater on grooved surfaces where the groove's length is along the moving wall's axis of motion. Therefore, the directional properties of roughness considerably affect the resultant flow-factors. Furthermore, the simplifying assumption that the lubricant does not move along the vertical axis, made to derive the Reynolds equation, was invalidated. In particular, CFD analysis indicated that the vertical velocity component is comparable to the streamwise velocity component.

Chapter 5

Equations in the Relative Frame – The MRF Approach

5.1 Introduction

In this chapter, the unsteady Navier-Stokes flow equations are derived for an incompressible lubricant in multiple frames of reference for the examined application. This way, the relative motion between the piston, its rings and the cylinder liner is considered without utilizing an unsteady solver which incorporates moving meshes. It should be noted that this set of equations is tailored for the examined application.

5.2 Clarifications

This study focuses on developing the flow equations for a fluid which moves between a pair of surfaces in relative motion. The bodies under investigation are the piston, its rings and the engine's cylinder. The derived set of equations is applicable to every cylinder of the engine. The prime area of interest is the lubricant's flow between the piston rings and the cylinder liner. The piston ring-pack performs a periodic, translational motion inside the cylinder while the former is stationary. Therefore, the inertial coordinate system is placed on the cylinder wall and the relative, or moving coordinate system belongs to the piston ring-pack assembly. Both are Cartesian coordinate systems and the flow-fields are expressed using the Eulerian description[18]. Thus, the position vector of the points consisting the examined area of the flow-field are determined by $\mathbf{r}_i = (x_i, y_i, z_i)$ where the index $i = I$ corresponds

to the position vector with regards to the inertial coordinate system and $i = R$ to the relative coordinate system. The datum of inertial coordinate system O_I is placed on the cylinder wall for convenience reasons as shown in Figure 5.1 and the datum of relative coordinate system O_R on the piston's upper surface. In the same figure, the distance between these coordinate systems with regards to O_I is marked by $\mathbf{O_I O_R} = \mathbf{d}$. This distance varies according to the translational motion of the piston.

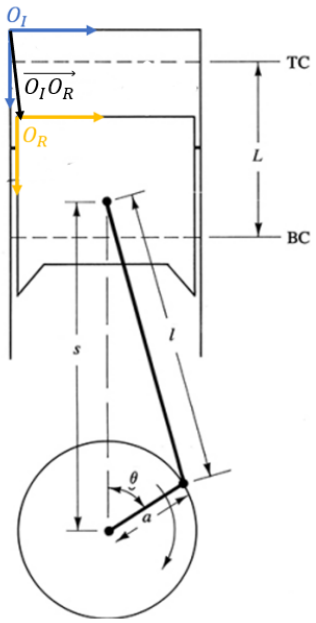

Figure 5.1: *2-D Schematic of cylinder, piston, connecting rod and crankshaft where L = stroke, l = connecting rod's length, α = crank radius and θ = crank angle. From [12].*

In the following section, the flow-equations are expressed in both the inertial and the relative coordinate system. It is aimed to describe the lubricant's relative flow in terms of the absolute velocity and the distance between the datums of each coordinate system. This way, the relative motion between the moving and the stationary body is simulated without using computationally expensive unsteady solvers which incorporate moving meshes. Furthermore, it's preferred to use the flow equations in the moving coordinate system, because the undergoing flow phenomena are more easily described. However, the velocity field is computed with regards to the inertial coordinate system in order to calculate the forces applied to each body.

5.3 Derivation of the MRF Flow Equations

The system of Navier-Stokes PDEs comprises of the continuity and the momentum equations. These are expressed for an incompressible lubricant with constant viscosity in the inertial coordinate system by

$$Continuity: \ \nabla \cdot \mathbf{u_I} = 0 \tag{5.1}$$

$$Momentum: \ \frac{D\mathbf{u_I}}{Dt} = -\frac{\nabla p}{\rho} + \nu \nabla \cdot \nabla \mathbf{u_I} \tag{5.2}$$

where index I specifies the velocity vector in the Inertial or stationary coordinate system.

The relationship between the lubricant's position vector $\mathbf{r}$ at the inertial and the relative coordinate system is

$$\mathbf{r_I} = \mathbf{r_R} + \mathbf{O_I O_R} \tag{5.3}$$

where index R specifies the position vector in the Relative or moving coordinate system and the position vector $\mathbf{d} = \mathbf{O_I O_R}$ corresponds to the vector of distance between the datums of inertial and relative coordinate systems.

The fluid's velocity in the inertial coordinate system is defined by

$$\mathbf{u_I} = \frac{D\mathbf{r_I}}{Dt} = \frac{\partial \mathbf{r_I}}{\partial t} + \mathbf{r_I} \cdot \nabla \mathbf{r_I} \tag{5.4}$$

In the same manner, the fluid's velocity vector in the relative coordinate system is expressed by

$$\mathbf{u_R} = \frac{D\mathbf{r_R}}{Dt} = \frac{\partial \mathbf{r_R}}{\partial t} + \mathbf{r_R} \cdot \nabla \mathbf{r_R} \tag{5.5}$$

Also, the rate of distance change $\dot{\mathbf{d}}$ between the datums of inertial and relative coordinate systems is calculated by

$$\dot{\mathbf{d}} = \frac{D\mathbf{O_I O_R}}{Dt} = \frac{\partial \mathbf{O_I O_R}}{\partial t} + \mathbf{O_I O_R} \cdot \nabla \mathbf{O_I O_R} \tag{5.6}$$

The fluid's acceleration is defined by the temporal derivate of the velocity vector,

$$\alpha_{\mathbf{I}} = \frac{D\mathbf{u_I}}{Dt} = \frac{\partial \mathbf{u_I}}{\partial t} + \mathbf{u_I} \cdot \nabla \mathbf{u_I} \tag{5.7}$$

$$\alpha_{\mathbf{R}} = \frac{D\mathbf{u_R}}{Dt} = \frac{\partial \mathbf{u_R}}{\partial t} + \mathbf{u_R} \cdot \nabla \mathbf{u_R} \tag{5.8}$$

$$\ddot{\mathbf{d}} = \frac{D\dot{\mathbf{d}}}{Dt} = \frac{\partial \dot{\mathbf{d}}}{\partial t} + \dot{\mathbf{d}} \cdot \nabla \dot{\mathbf{d}} \tag{5.9}$$

The relationship between the acceleration of the fluid's absolute velocity $\alpha_{\mathbf{I}}$ and its relative acceleration $\alpha_{\mathbf{R}}$ is found by substituting equation 5.3 in 5.7,

$$\begin{aligned} &\alpha_{\mathbf{I}} = \frac{D\mathbf{u_I}}{Dt} = \frac{D(\mathbf{u_R} + \dot{\mathbf{d}})}{Dt} = \frac{\partial(\mathbf{u_R} + \dot{\mathbf{d}})}{\partial t} + (\mathbf{u_R} + \dot{\mathbf{d}}) \cdot \nabla(\mathbf{u_R} + \dot{\mathbf{d}}) = \\ &\frac{\partial \mathbf{u_R}}{\partial t} + \frac{\partial \dot{\mathbf{d}}}{\partial t} + (\mathbf{u_R} + \dot{\mathbf{d}}) \cdot \nabla \mathbf{u_R} + (\mathbf{u_R} + \dot{\mathbf{d}}) \cdot \nabla \dot{\mathbf{d}} = \\ &\frac{\partial \mathbf{u_R}}{\partial t} + \mathbf{u_R} \cdot \nabla \mathbf{u_R} + \frac{\partial \dot{\mathbf{d}}}{\partial t} + \dot{\mathbf{d}} \cdot \nabla \dot{\mathbf{d}} + \mathbf{u_R} \cdot \nabla \dot{\mathbf{d}} + \dot{\mathbf{d}} \cdot \nabla \mathbf{u_R} \end{aligned} \tag{5.10}$$

By combining equations 5.8 & 5.9 in 5.10, its final form is

$$\frac{D\mathbf{u_I}}{Dt} = \frac{D\mathbf{u_R}}{Dt} + \frac{D\dot{\mathbf{d}}}{Dt} + \mathbf{u_R} \cdot \nabla \dot{\mathbf{d}} + \dot{\mathbf{d}} \cdot \nabla \mathbf{u_R} \tag{5.11}$$

The continuity equation in the relative, or moving coordinate system is derived from equation 5.1 by applying 5.3

$$\nabla \cdot \mathbf{u_I} = 0 \Leftrightarrow \nabla(\mathbf{u_R} + \dot{\mathbf{d}}) = 0 \Leftrightarrow \frac{\partial u_{i,R}}{\partial x_i} + \frac{\partial \dot{d}_i}{\partial x_i} = 0 \tag{5.12}$$

The momentum equation for the fluid's relative flow is

$$\frac{D\mathbf{u_R}}{Dt} = -\frac{\nabla p}{\rho} + \nu \nabla \cdot \nabla \mathbf{u_R} \tag{5.13}$$

By substituting equation 5.11 and $\mathbf{u_R} = \mathbf{u_I} - \dot{\mathbf{d}}$ in 5.13, the conservation of the fluid's momentum in the relative coordinate system in terms of the absolute velocity $\mathbf{u_I}$ and the rate of distance change between the datums of the afore-mentioned coordinate

systems is expressed by,

$$\begin{aligned}
&\frac{D\mathbf{u_I}}{Dt} - \frac{D\dot{\mathbf{d}}}{Dt} - \mathbf{u_R}\cdot\nabla\dot{\mathbf{d}} - \dot{\mathbf{d}}\cdot\nabla\mathbf{u_R} = -\frac{\nabla p}{\rho} + \nu\nabla\cdot\nabla(\mathbf{u_I} - \dot{\mathbf{d}}) \Leftrightarrow \\
&\frac{D\mathbf{u_I}}{Dt} - \frac{D\dot{\mathbf{d}}}{Dt} - (\mathbf{u_I} - \dot{\mathbf{d}})\cdot\nabla\dot{\mathbf{d}} - \dot{\mathbf{d}}\cdot\nabla(\mathbf{u_I} - \dot{\mathbf{d}}) = -\frac{\nabla p}{\rho} + \nu\nabla\cdot\nabla(\mathbf{u_I} - \dot{\mathbf{d}}) \Leftrightarrow \\
&\frac{\partial\mathbf{u_I}}{\partial t} + \mathbf{u_I}\cdot\nabla\mathbf{u_I} - \frac{\partial\dot{\mathbf{d}}}{\partial t} - \mathbf{u_I}\cdot\nabla\dot{\mathbf{d}} - \dot{\mathbf{d}}\cdot\nabla\mathbf{u_I} + \dot{\mathbf{d}}\cdot\nabla\dot{\mathbf{d}} = \frac{\nabla p}{\rho} + \nu\nabla\cdot\nabla(\mathbf{u_I} - \dot{\mathbf{d}}) \Leftrightarrow \\
&\frac{\partial(u_{i,I} - \dot{d}_i)}{\partial t} + u_{i,I}\frac{\partial u_{i,I}}{\partial x_i} - u_{i,I}\frac{\partial\dot{d}_i}{\partial x_i} - \dot{d}_i\frac{\partial u_{i,I}}{\partial x_i} + \dot{d}_i\frac{\partial\dot{d}_i}{\partial x_i} = \frac{1}{\rho}\frac{\partial p}{\partial x_i} + \nu\frac{\partial}{\partial x_i}(\frac{\partial(u_{i,I} - \dot{d}_i)}{\partial x_i})
\end{aligned} \tag{5.14}$$

where the terms with the index i in the final form of the equation are expressed in tensor notation. From equation 5.14 is observed that three more convective terms contribute in the flow-field of absolute velocity. These are the third, fourth and firth terms of the equation's left-hand side. The first one expresses the transportation of distance rate of change with the fluid's absolute velocity. The next indicates the exact opposite, meaning the transportation of information regarding to the fluid's velocity via the rate of distance change. The last convective term expresses the transport of distance change rate with itself. Each one them represents the interaction of absolute velocity field with the distance change between the coordinate systems' datums as the former varies with time.

The flow between any pair surfaces that move relatively to each other in the longitudinal direction can be studied using the system of equations 5.12 & 5.14. The analytical expression of the distance between the datums of the inertial and the relative coordinate system is required for numerically solving these equations. It depends on the application, the geometries of interacting components and the selected positions of the datums. Also, its temporal derivate is needed for computing the rate of distance change in every position of the computational domain.

5.4 Summary

The unsteady Navier-Stokes equations were derived for an incompressible lubricant in the relative coordinate system using the fluid's absolute velocity and the rate of distance change between the datums of the relative and the inertial coordinate system. Even though the examined application concerns the lubrication between the piston ring-pack and the cylinder liner, the final form of equations is suitable for every assembly whose components move relatively to each other in translational motion. The major benefit of these equations is that they account for the relative motion between two bodies without utilizing numerical solvers with moving meshes.

Chapter 6

Conclusions

6.1 Overview

In this thesis, the influence of cylinder liner's surface roughness was investigated over the friction opposing the motion of piston's top ring in Chapter 3. Typically, the friction between two engineering components in relative motion is reduced by applying a lubricant between them. Initially, a 3-D computational model was developed with the purpose of numerically solving the Navier-Stokes flow equations for an incompressible lubricant. It was deduced in Section 3.3 that it is computationally expensive to perform unsteady simulations in the examined micro-fluidics problem. Therefore, a steady solver was utilized to acquire the lubricant's flow fields for the selected engine's operation point. A parametric analysis was conducted to extract the most dominant surface feature of the cylinder liner among the groove's width, depth and pitch with regards to the applied friction at the top ring. A framework was developed for quickly generating the geometries of the top ring with alternative surface characteristics of the cylinder liner in order to perform this study. The process of geometry & mesh generation, case files & folders creation and simulation execution was automated using a BASH script.

Furthermore, the most common method in the automotive industry for modelling the lubrication between moving components was presented in Chapter 4. It employs the mean-flow Reynolds equation which is a corrected variant of the general Reynolds equation. This form incorporates the flow-factors which serve as corrections of the volumetric flow passing through a pair of rough plates. This way, the surface roughness impact over the lubricant's flow is treated separately from the investigated geometry and aspects of the physical problem. Thus, it is possible to simulate 3-D rough surfaces with the 2-D Reynolds equation in macro-scale where hydrodynamic, or mixed lubrication is present as long as the asperity interaction is minor. This

model is currently adopted from [11] to compute the friction opposing the motion of the piston ring-pack during the cylinder's entire cycle. The pressure and shear flow-factors were computed utilizing 3-D CFD simulations of the fundamental fluid flows. These were compared with the ones that are used in [11] and their differences were justified.

6.2 Conclusions

Upon completion of the studies that were presented in the previous chapters, the following conclusion are drawn:

1. Lower friction is applied at the piston's top ring with smaller groove pitch, larger width and depth. Also, for low values of groove pitch, the width doesn't affect the resultant specific friction. The same is applicable to groove depth as long as the groove width is large. Therefore, based on Section 3.8, it is proposed to design the inner cylinder wall with small groove pitch, large width and depth.

2. Greater vertical load is exerted on the top ring with large groove pitch and small width. The groove's depth doesn't affect the top ring's load carrying capacity. It is preferred to design engineering components with reduced friction and increased load carrying capacity, thus the magnitude of the liner's surface characteristics need to compromise for satisfying both design goals.

3. The Reynolds equation is a useful tool for computing the necessary Couette and Poiseuille flows whose results are utilized for calculating the flow-factors. Good correlation was achieved between the flow-factors that were computed by CFD and the general Reynolds equation for large distance between the rough plates. The opposite is true in cases with small distance between the rough plates. The Reynolds equation' simplifying assumptions are limiting the accuracy of the simulated fundamental fluid flows. Especially for cases with small distance between the pair of plates, the Reynolds equation demonstrates that the lubricant entering the groove cannot exit from it and the resultant flow-field is moving between the top plate and the generated oil film formed at the groove's base.

4. The Reynolds equation assumption that the fluid does not move in the vertical axis was invalidated by 3-D CFD simulations. In particular, the field of velocity's vertical components was found in Sections 4.3.3 & 4.3.4 to be comparable with the streamwise velocity component.

5. The groove pitch should be considered in surface topography description, because it affects the flow-factors. In detail, as the groove pitch decreases, the flow-factors are reduced.

6. The unsteady Navier-Stokes equations were derived for an incompressible fluid in the relative, or moving frame of reference in terms of absolute velocity and rate of distance change between the inertial and the relative coordinate system. This system of equations can be implemented to numerically solve for the unsteady flow between bodies in relative motion without incorporating an unsteady solver with moving meshes. The final form of the momentum equation includes three more convective terms which express the interaction between the absolute velocity and the rate of distance change.

Future Work Proposals

Based on the key-findings of the present thesis, this work can be further extended by:

1. Perform a gradient-based or gradient-free optimization for the surface roughness pattern on the cylinder wall by utilizing the geometry generation framework and the developed codes for automating the steps of creating and executing the CFD simulations. These runs would be focused towards the groove's shape and their spacing.
2. Perform a 3-D parametric analysis which includes the hatch angle as a design variable. Then, the design space would be limited to the design variable's ranges that they considerably affected the applied specific friction at the top ring. This extended design space could be used for conducting gradient-based or gradient-free optimization to which the directional properties of surface roughness would be taken into account.
3. Validate the 3-D CFD model which includes the detailed geometry of the top ring and the cylinder liner with experiments that will be conducted by TMC.
4. Conduct simulations with the mean-flow Reynolds equation in which the flow-factors were computed by 3-D CFD. Based on the resultant pressure-field, the friction mean effective pressure (FMEP) should be computed and compared with experimental data during the same engine rotational speed and load.
5. Select the uncertain variables for the examined system of piston rings and cylinder liner and compute the statistical moments of specific friction for the proposed surface topography of the liner, utilizing a method for uncertainty quantification.

Appendix A

Flowcharts

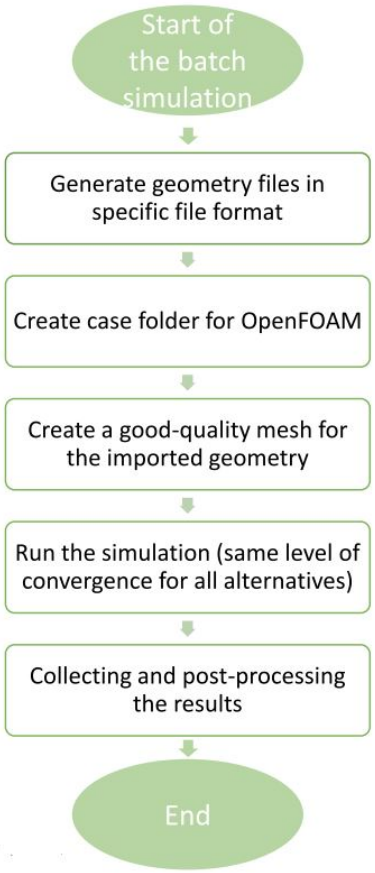

Figure A.1: *The necessary steps for performing the parametric analysis*

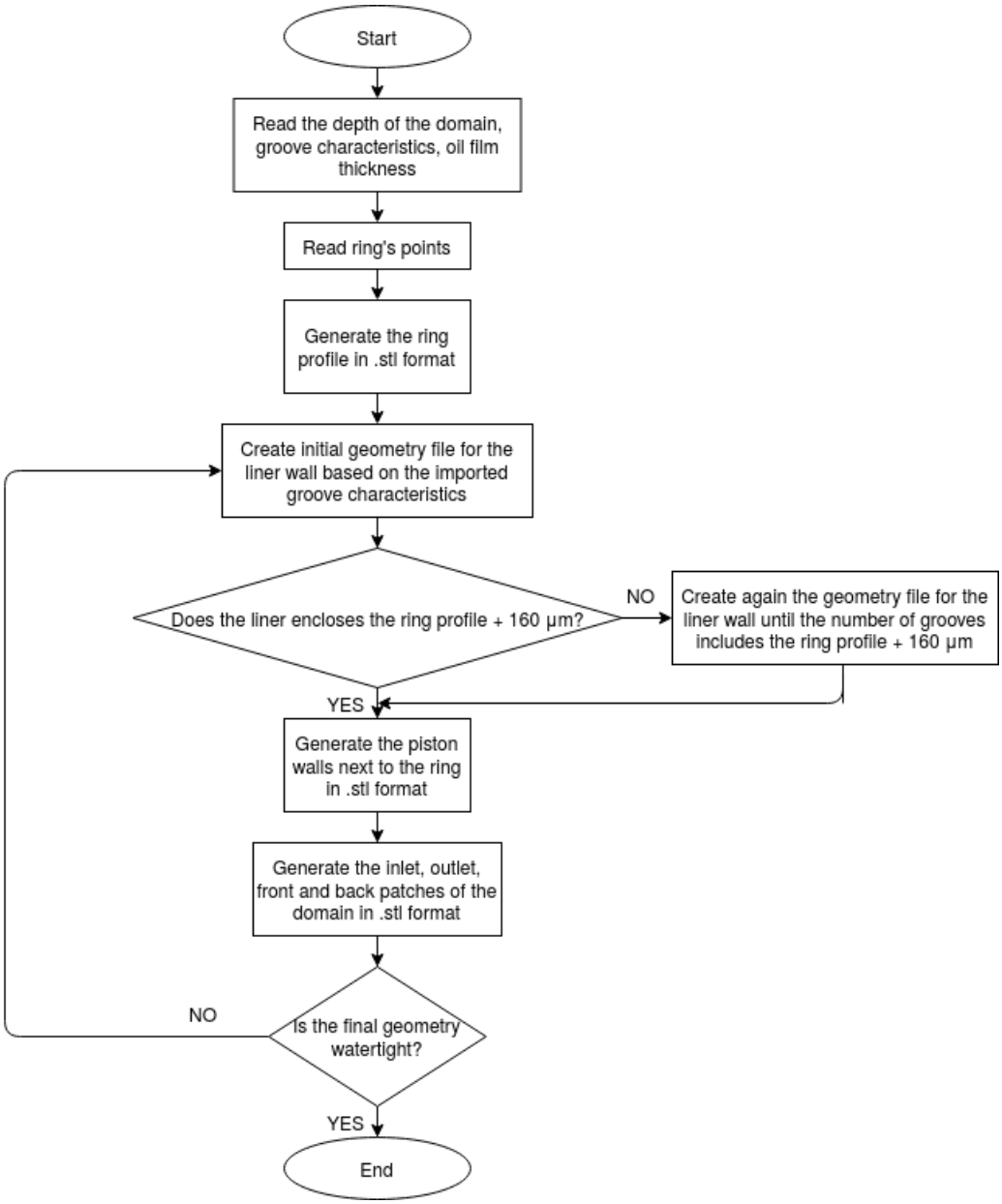

Figure A.2: *Flow-chart of the framework for generating the geometry files*

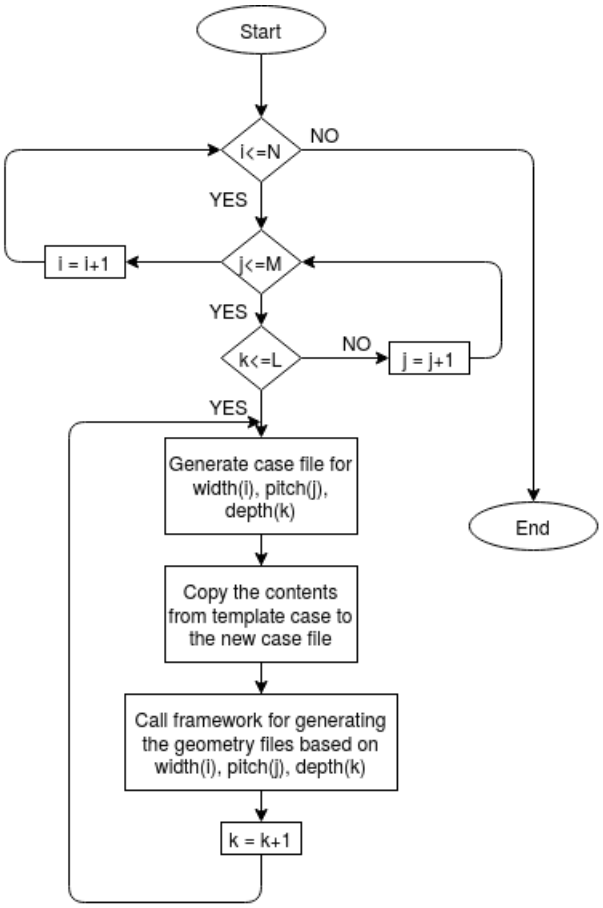

Figure A.3: *Flow-chart of the script in BASH for creating the case files*

Appendix B

Derivation of the Reynolds Equation

The Reynolds equation can be derived in two different ways. In this section, the Reynolds equation is obtained from the mass and force equilibrium in an elementary volume of a viscous and newtonian fluid. The fluid is only moving along the x-direction and y-direction, thus the vertical component of velocity is assumed zero. Then, the forces which contribute to its motion belong the same axis. These forces are the normal load due to the generated pressure field and the shear stresses τ_x & τ_y which oppose the fluid's motion. In Figure B.1, the forces which are applied at the fluid's control volume are illustrated along the x-axis.

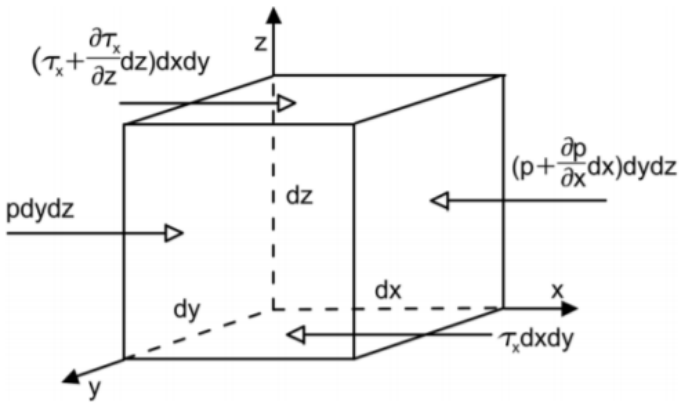

Figure B.1: *Force equilibrium in an elementary volume.*

The force equilibrium expresses that the sum of forces which are applied at the selected fluid's volume is zero,

$$\begin{aligned} &pdydz + \tau_x dxdy = (\tau_x + \frac{\partial \tau_x}{\partial z}dz)dxdy + (p + \frac{\partial p}{\partial x}dx)dydz \Leftrightarrow \\ &\frac{\partial \tau_x}{\partial z}dxdydz = \frac{\partial p}{\partial x}dxdydz \\ &\frac{\partial \tau_x}{\partial z} = \frac{\partial p}{\partial x} \end{aligned} \tag{B.1}$$

since $dxdydz \neq 0$ is the volume of the examined section of the flow field. The same is applicable to the lateral direction of motion(y-axis), thus

$$\frac{\partial \tau_y}{\partial z} = \frac{\partial p}{\partial y} \tag{B.2}$$

Also, it is assumed that the pressure field is constant along the vertical axis (z-axis), therefore $\frac{\partial p}{\partial z} = 0$. Provided that the examined fluid is newtonian and has constant dynamic viscosity μ, the shear stress along its axis of motion are expressed from

$$\tau_x = \mu \frac{\partial u}{\partial z} \tag{B.3}$$

$$\tau_y = \mu \frac{\partial v}{\partial z} \tag{B.4}$$

By combining equations B.1 & B.3 and assuming that the pressure difference is constant between the edges of the finite volume

$$\begin{aligned} &\frac{\partial p}{\partial x} = \frac{\partial}{\partial z}(\mu \frac{\partial u}{\partial z}) \Leftrightarrow \\ &\frac{\partial p}{\partial x}\frac{z^2}{2} + C_1 z + C_2 = \mu u \end{aligned} \tag{B.5}$$

where C_1, C_2 are coefficients that arised after integrating twice the equation which includes both B.1 & B.3. These coefficient are calculated from the boundary conditions of the problem. In this section, it is assumed that the upper surface of Figure B.1 is moving with velocity $\mathbf{V} = (U, 0, 0)$ and the bottom surface is stationary, therefore the fluid's velocity components are

$$u = (\frac{z^2 - zh}{2\mu})\frac{\partial p}{\partial x} + U\frac{z}{h} \tag{B.6}$$

$$v = (\frac{z^2 - zh}{2\mu})\frac{\partial p}{\partial y} \tag{B.7}$$

where h is the distance between the upper and the lower surface of the investigated volume. This relationship shows that the flow is described by superimposing the pressure-driven and velocity-driven flows along the corresponding axis of motion.

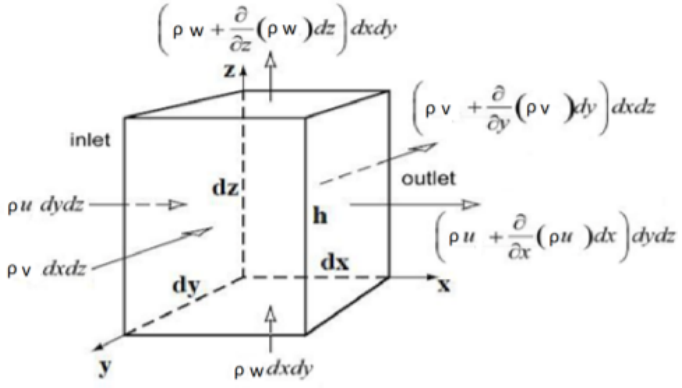

Figure B.2: *Mass equilibrium in an elementary volume.*

In the same examined volume of the fluid, the mass equilibrium determines that flow rates which enter or exit the control volume are equal to accumulation rate of mass inside the control volume as depicted in Figure B.2,

$$\begin{aligned} &\rho u dydz + \rho v dxdz + \rho w dxdy - (\rho u + \frac{\partial}{\partial x}(\rho u)dx)dydz \\ &- (\rho v + \frac{\partial}{\partial y}(\rho v)dy)dxdz - (\rho w + \frac{\partial}{\partial z}(\rho w)dz)dxdy = \frac{\partial \rho}{\partial t}dxdydz \Leftrightarrow \\ &- \frac{\partial}{\partial x}(\rho u) - \frac{\partial}{\partial y}(\rho v) - \frac{\partial}{\partial z}(\rho w) = \frac{\partial \rho}{\partial t} \end{aligned} \tag{B.8}$$

It has been clarified that $w = 0$. By substituting equations B.6 & B.7 to B.8 and integrating the resultant equation from the lower to the upper surface, the Reynolds equation is derived

$$\frac{\partial \rho h}{\partial t} + \frac{U}{2}\frac{\partial(\rho h)}{\partial x} - \frac{\partial}{\partial x}(\frac{\partial p}{\partial x}\frac{\rho}{12\mu}h^3) - \frac{\partial}{\partial y}(\frac{\partial p}{\partial y}\frac{\rho}{12\mu}h^3) = 0 \tag{B.9}$$

Bibliography

[1] A.Senatore: *Editorial: Special Issue "Automotive Tribology"*. Lubricants, 8(4):48, 2020.

[2] *Toyota aims for sales of more than 5.5 million electrified vehicles including 1 million zero emission vehicles per year by 2030*. `https://global.toyota/en/newsroom/corporate/20353243.html`.

[3] *Tribology, Wikipedia, the free encyclopedia*. `https://en.wikipedia.org/wiki/Tribology`.

[4] R.Gohar and H.Rahnejat: *Fundamentals of Tribology*. Imperial College Press, 2008.

[5] M.Nosonovsky and B.Bhushan: *Multiscale friction mechanisms and hierarchical surfaces in nano- and bio-tribology*. Material Science and Engineering: R: Reports, 58(3–5):162–193, 2007.

[6] B.J.Hamrock: *Fundamentals of fluid film lubrication*. NASA Office of Management, Scientific and Technical Information Program, 1991.

[7] H.Rahnejat: *Tribology and dynamics of engine and powertrain, Fundamentals, applications and future trends*. Woodhead Publishing, 2010.

[8] I.Hutchings and P.Shipway: *Tribology, Friction and Wear of Engineering Materials*. Elsevier, 2017.

[9] DB.J.Tevis, J.Till and P.Lars: *Quantitative characterization of surface topography using spectral analysis*. Surface Topography: Metrology and Properties, 5(1):013001, 2017.

[10] H.Chen and T.Tian: *The Influences of Cylinder Liner Honing Patterns and Oil Control Ring Design Parameters on the Interaction between the Twinland Oil Control Ring and the Cylinder Liner in Internal Combustion Engines*. SAE International, 2008.

[11] S.Sanda, H.Nagakura, N.Katsumi S.Hotta K.Kawai and M.Murakami: *Analysis of piston frictional force under engine firing condition - effect of cylinder bore crosshatch angle on friction between piston ring pack and cylinder bore*. Transactions of Society of Automotive Engineers of Japan, 45(5):799–804, 2014.

[12] J.B.Heywood: *Internal Combustion Engine Fundamentals, Second Edition.* McGraw-Hill Education, 2018.

[13] *Honing(metalworking)-, Wikipedia, the free encyclopedia.* `https://en.wikipedia.org/wiki/Tribology`.

[14] P.Anderson, J.Tamminen and C.Sandstrom: *Piston ring tribology - a literature survey.* VTT Tiedotteita - Research Notes 2178, 2002.

[15] S.V.Patankar and D.B.Spalding: *A calculation procedure for heat, mass and momentum transfer in three-dimensional parabolic flows.* International Journal of Heat and Mass Transfer, Volume 15, Issue 10, Pages 1787-1806, October 1972.

[16] B.E.Rapp: *Microfluidics: Modeling, Mechanics and Mathematics.* Elsevier, 2016.

[17] *PetroWiki, oil fluid characteristics.* `https://petrowiki.org/Oil_fluid_characteristics`.

[18] Σ.Τσαγγάρης: *Μηχανική των ρευστών, θεωρία & ασκήσεις.* Εκδόσεις ΤΣΟΤΡΑΣ, 2015.

[19] F.Moukalled, L.Mangani and M.Darwish: *The Finite Volume Method in Computational Fluid Dynamics: An Advanced Introduction with OpenFOAM® and Matlab.* Springer International Publishing, 2016.

[20] Ε.Παπουτσής-Κιαχαγιάς: *Συζυγείς μέθοδοι χαμηλού υπολογιστικού κόστους για τυρβώδεις ροές, στην αεροδυναμική βελτιστοποίηση.* Διδακτορική διατριβή, Εργαστήριο Θερμικών Στροβιλομηχανών, Ε.Μ.Π., Αθήνα, 2013.

[21] N.Patir and H.S.Cheng: *Application of average flow model to lubrication between rough sliding surfaces.* Journal of Lubrication Technology, 101(2):220–229, 1979.

[22] N.Patir and H.S.Cheng: *An average flow model for determining effects of three-dimensional roughness on partial hydrodynamic lubrication.* ASME. J. of Lubrication Tech, 100(1):12–17, 1978.

[23] *Openfoam: User guide v2006, The open source CFD toolbox.* `https://www.openfoam.com/documentation/guides/latest/doc/guide-fos-field-CourantNo.html`.

[24] M.Arghir, N.Roucou, M.Helene and J.Frene: *An average flow model for determining effects of three-dimensional roughness on partial hydrodynamic lubrication.* ASME. J. of Tribology, 125(2):309–318, 2003.

[25] M.Gore, S.J.Howell-Smith, P.D.King and H.Rahnejat: *Measurement of In-Cylinder Friction Using the Floating Liner Principle*, 2012.

[26] M.Gore, M.Theaker, S.Howell Smith H.Rahnejat and P.D.King: *Direct measurement of piston friction of internal-combustion engines using the floating-*

liner principle. Proceedings of the Institution of Mechanical Engineers, Part D: Journal of Automobile Engineering, 228(3):344–354, 2014.

[27] *Openfoam: User guide v2006:a.4 standard boundary conditions, The open source CFD toolbox*. `https://www.openfoam.com/documentation/user-guide/standard-boundaryconditions.php`.

[28] *Openfoam 2.2.0: Numerical methods*. `https://openfoam.org/release/2-2-0/numerics-boundedness/`.

[29] *Openfoam v6 user guide: 5.4 mesh generation with snappyhexmesh*. `https://cfd.direct/openfoam/user-guide/v6-snappyhexmesh/`.

[30] S.A.Mohamad, X.Lu and Q.Zheng: *Effect of Cylinder Liner Oil Grooves Shape on Two-Stroke Marine Diesel Engine's Piston Ring Friction Force*. Advances in Mechanical Engineering, 7(2):837–960, 2015.

[31] M.Masjedi and M.M.Khonsari: *On the effect of surface roughness in point-contact ehl: Formulas for film thickness and asperity load*. Tribology International, 82:228–244, 2015.

[32] N.Morris, M.Leighton, M.De la Cruz R.Rahmani H.Rahnejat and S.Howell-Smith: *Combined numerical and experimental investigation of the micro-hydrodynamics of chevron-based textured patterns influencing conjunctional friction of sliding contacts*. Proceedings of the Institution of Mechanical Engineers, Part J: Journal of Engineering Tribology, 229(4):316–335, 2015.

[33] N.Morris, R.Rahmani, H.Rahnejat P.D.King and S.Howell-Smith: *A numerical model to study the role of surface textures at top dead center reversal in the piston ring to cylinder liner contact.* ASME. J. Tribol., 138(2), 2016.

[34] B.J.Hamrock and D.Dowson: *Ball bearing lubrication: the elastohydrodynamics of elliptical contacts*. 1981.

[35] O.Akalin and G.M.Newaz: *Piston Ring-Cylinder Bore Friction Modeling in Mixed Lubrication Regime: Part I—Analytical Results* . Journal of Tribology, 123(1):211–218, 1999.

[36] J.Yeau-Ren: *Theoretical Analysis of Piston-Ring Lubrication Part II—Starved Lubrication and Its Application to a Complete Ring Pack*. Tribology Transactions, 35(4):707–714, 1992.

[37] J.A.Greenwood and J.H.Tripp: *The contact of two nominally flat rough surfaces*. Proc. IMechE, J. Mech. Eng. Sci., 185(1):625–633, 1971.

[38] J.Peklenik: *New Developments in Surface Characterization and Measurements by Means of Random Process Analysis*. Proceedings of the Institution of Mechanical Engineers, Conference Proceedings, 182(11):108–126, 1967.

[39] MB.Dobrica and M.Fillon: *About the validity of reynolds equation and inertia effects in textured sliders of infinite width.* Proceedings of the Institution of Mechanical Engineers, Part J: Journal of Engineering Tribology, 223(1):69–78, 2009.

Εθνικό Μετσόβιο Πολυτεχνείο
Σχολή Μηχανολόγων Μηχανικών
Τομέας Ρευστών
Μονάδα Παράλληλης Υπολογιστικής Ρευστοδυναμικής & Βελτιστοποίησης

Ανάπτυξη Λογισμικού Προσομοίωσης της Λίπανσης μεταξύ των Δαχτυλιδιών Πιστονιού/Χιτωνίου Μηχανής Εσωτερικής Καύσης

Διπλωματική Εργασία

Αλεξάνδρα-Ιωάννα Λιόση

Ακαδημαϊκός Επιβλέπων:
Κυριάκος Χ. Γιαννάκογλου, Καθηγητής ΕΜΠ

Βιομηχανικός Επιβλέπων:
Δρ. Κωνσταντίνος Γκαγκάς, Ειδικός, Toyota Motor Europe

Αθήνα 2021

ΕΚΤΕΝΗΣ ΠΕΡΙΛΗΨΗ ΣΤΑ ΕΛΛΗΝΙΚΑ

Εισαγωγή - Περιγραφή Προβλήματος

Κάθε χρόνο οι κρατικές και διεθνείς νομοθεσίες σχετικά με τη ρύπανση των επίγειων οχημάτων γίνεται πιο αυστηρή. Οι κατασκευαστές βελτιώνουν τη λειτουργία των εμβολοφόρων μηχανών που παράγουν, για να συμβαδίζουν με τα νέα επιτρεπτά όρια. Στοχεύουν στη μείωση της κατανάλωσης καυσίμου, η οποία μπορεί να επιτευχθεί και με τη μείωση των απωλειών τριβής στα κινούμενα μέρη. Από τη βιβλιογραφία, είναι γνωστό ότι 25 % με 40 % των συνολικών απωλειών τριβής οφείλονται στην αλληλεπίδραση του χιτωνίου με τα δαχτυλίδια του εμβόλου. Έτσι, σε αυτήν τη διπλωματική εξετάζεται η λίπανση αυτής της περιοχής, εστιάζοντας στην επιρροή των επιφανειακών χαρακτηριστικών, ή τραχύτητας, του χιτωνίου στην τριβή των δαχτυλιδιών του εμβόλου. Για αυτή τη μελέτη, επιλύονται οι εξισώσεις Navier-Stokes για τη μόνιμη, στρωτή ροή ασυμπίεστου λιπαντικού στην περιοχή όπου επικρατεί υδροδυναμική λίπανση, στο περιβάλλον του OpenFOAM.

Συγκεκριμένα, η διπλωματική εργασία χωρίζεται σε δύο τμήματα. Το πρώτο από αυτά ασχολείται με την εύρεση των χαρακτηριστικών της επιφάνειας του χιτωνίου που οδηγούν σε μειωμένες απώλειες λόγω τριβής. Ακόμη, προετοιμάζει το μεγαλύτερο μέρος

των απαιτούμενων εργαλείων για τη βελτιστοποίηση με αιτιοκρατικές ή στοχαστικές μεθόδους σε ενδεχόμενη επόμενη φάση. Στο δεύτερο τμήμα, σχολιάζεται το υπολογιστικό μοντέλο της μέσης ροής που συνήθως χρησιμοποιείται για τη μοντελοποίηση της λίπανσης μεταξύ του χιτωνίου και των δαχτυλιδιών του εμβόλου. Αυτό προϋποθέτει των υπολογισμό συντελεστών, οι οποίοι μέχρι σήμερα υπολογίζονται από την εξίσωση Reynolds. Αυτοί υπολογίστηκαν μέσω προσομοιώσεων Υπολογιστικής Ρευστοδυναμικής (ΥΡΔ) και συγκρίθηκαν με τους αντίστοιχους που έχουν προκύψει από [1]. Αξιολογούνται τα πλεονεκτήματα και τα μειονεκτήματα μεταξύ των διαφορετικών μεθόδων για τον υπολογισμό των συντελεστών.

Περιγραφή Τραχύτητας Χιτωνίου

Η τραχύτητα στο εσωτερικό του χιτωνίου διαμορφώνεται από κατεργασίες φινιρίσματος και είναι τάξης μm. Η ποιότητα επιφανείας χωρίζεται σε τρεις κατηγορίες ανάλογα με το αίτιο που την προκαλεί, όπως επεξηγείται στο Υποκεφάλαιο 1.2 του αγγλικού κειμένου. Η τραχύτητα συνήθως περιγράφεται από το μέσο ύψος τραχύτητας R_a και το ενδεικνύμενο ύψος τραχύτητας (RMS) R_z, όπως αυτά ορίζονται στο Υποκεφάλαιο 1.2.2. Παρόλα αυτά, στο πλαίσιο της διπλωματικής εργασίας η τραχύτητα στο εσωτερικό του χιτωνίου αποτελείται από διαδοχικές ή διασταυρούμενες αυλακώσεις τριγωνικής διατομής όπως φαίνεται στο Σχήμα Β′.3. Συνεπώς, τα χαρακτηριστικά μεγέθη, ή μεταβλητές σχεδιασμού, της παραμετρικής ανάλυσης αποτελούν το βάθος, το βήμα και το πλάτος αυλάκωσης. Στο δεύτερο τμήμα της εργασίας εξετάζεται και η επίδραση της γωνίας αυλάκωσης. Οι αυλακώσεις συνεισφέρουν στην αποθήκευση και στην καλύτερη διανομή λιπαντικού, ευνοώντας τις συνθήκες λίπανσης.

Παραμετρική Ανάλυση

Δεδομένου ότι τα χαρακτηριστικά της επιφάνειας του χιτωνίου είναι τάξης μm, δεν προσομοιώνεται ολόκληρη η διαδρομή του εμβόλου, η οποία είναι τάξης mm. Ακόμη, πάνω στο έμβολο υπάρχουν τα δαχτυλίδια συμπίεσης, λαδιού και τα βοηθητικά δαχτυλίδια. Εξ αυτών, προσομοιώθηκε μόνο η επιρροή του χιτωνίου στην τριβή που ασκείται πάνω σε ένα δαχτυλίδι συμπίεσης για διαφορετικό βάθος, βήμα, πλάτος αυλάκωσης, όπως ενδεικτικά φαίνεται στο Σχήμα Β′.5, ενώ η γωνία αυλάκωσης λήφθηκε μηδέν. Αυτό σημαίνει ότι το χιτώνιο απαρτίζεται από διαδοχικές, παράλληλες αυλακώσεις που απέχουν μεταξύ τους απόσταση ίση με το βήμα. Οι απαραίτητες γεωμετρίες για την πραγματοποίηση των προσομοιώσεων ΥΡΔ δημιουργούνται μέσω ενός αλγορίθμου που αναπτύχθηκε κατά διάρκεια της εργασίας. Αυτός λαμβάνει ως εισόδους:

- Τα σημεία στο χώρο που περιγράφουν το προφίλ του δαχτυλιδιού
- Τα χαρακτηριστικά της αυλάκωσης με τριγωνική διατομή
- Το πάχος του στρώματος λιπαντικού, που καθορίζει την κατακόρυφη απόσταση μεταξύ του δαχτυλιδιού και του χιτωνίου
- Το βάθος του υπολογιστικού χωρίου για 3-D προσομοιώσεις

και παράγει τα αναγκαία αρχεία γεωμετρίας, που χρησιμοποιούνται για τη γένεση πλέγ-

ματος. Περισσότερες πληροφορίες για την εξεταζόμενη γεωμετρία και τον αλγόριθμο που δημιουργεί τα αντίστοιχα αρχεία σε κατάλληλη μορφή βρίσκονται στο Υποκεφάλαιο 3.2 του αγγλικού κειμένου.

Είναι υπολογιστικά ασύμφορη η ανάπτυξη ενός μοντέλου ΥΡΔ για τη μελέτη της μημόνιμης ροής του λιπαντικού κατά τη διάρκεια του κύκλου λειτουργίας του εμβόλου όπως φαίνεται στο Υποκεφάλαιο 3.3. Έτσι, εξετάστηκε η μόνιμη ροή ανάμεσα στο δαχτυλίδι συμπίεσης και το χιτώνιο. Οι οριακές συνθήκες για την πίεση και την ταχύτητα επιλέχθηκαν σε μια συγκεκριμένη ταχύτητα περιστροφής και για μια συγκεκριμένη γωνία στροφάλου. Αυτές προέκυψαν από το σημείο λειτουργίας της εμβολοφόρου μηχανής, όπου εμφανίζεται μέγιστη απώλεια ισχύος λόγω τριβών. Το λιπαντικό θεωρείται ασυμπίεστο με σταθερή συνεκτικότητα για τη μέση θερμοκρασία τοιχώματος του κυλίνδρου, η οποία υπολογίστηκε από πειραματικές μετρήσεις. Επιπλέον, το εξεταζόμενο υπολογιστικό χωρίο είναι πλήρες λιπαντικού και ο αέρας από το θάλαμο καύσης δεν λαμβάνεται υπόψη.

Έγινε μελέτη ανεξαρτησίας πλέγματος και αυτοματοποιήθηκε η διαδικασία δημιουργίας γεωμετρίας, γένεσης πλέγματος και εκτέλεσης της προσομοίωσης, πριν την πραγματοποίηση της παραμετρικής ανάλυσης. Τα αποτελέσματα της μελέτης ανεξαρτησίας πλέγματος παρουσιάζονται στο Υποκεφάλαιο 3.7 του αγγλικού κειμένου. Επιλέχθηκαν οι ρυθμίσεις πλέγματος που οδηγούν σε αποτελέσματα με απόκλιση κάτω του 1 % και με χρόνο προσομοίωσης 72 % λιγότερο ως προς την πιο ακριβή λύση που προσομοιώθηκε. Ακόμη, προγραμματίστηκε ένα εργαλείο που είναι υπεύθυνο για τη δημιουργία και την εκτέλεση των προσομοιώσεων που υλοποιήθηκαν με δειγματοληψία τιμών των μεταβλητών σχεδιασμού (ΜΣ). Συγκεκριμένα, αυτό λαμβάνει ως εισόδους τις επιθυμητές τιμές των ΜΣ και για όλους τους πιθανούς συνδυασμούς των ΜΣ καλεί τον αλγόριθμο που δημιουργεί την αντίστοιχη γεωμετρία. Στη συνέχεια, σύμφωνα με μια πρότυπη προσομοίωση, φτιάχνει τα απαραίτητα αρχεία για κάθε σενάριο και ανάλογα με τη διαθέσιμη υπολογιστική ισχύ, διανέμει τις προσομοιώσεις προς εκτέλεση. Οι λειτουργίες αυτού του βοηθητικού εργαλείου περιγράφονται στο Υποκεφάλαιο 3.8.

Αποτελέσματα Παραμετρικής Ανάλυσης

Οι εναλλακτικές γεωμετρίες που εξετάστηκαν, προέκυψαν από συνδυασμούς του βάθους, του βήματος και του πλάτος αυλάκωσης που φαίνονται στον Πίνακα Β′.1.

Βάθος	**Βήμα**	**Πλάτος**
1.5	121	20
5	472	40
10	1000	50

Πίνακας Β′.1: *Τιμές των μεταβλητών σχεδιασμού σε μm στην παραμετρική ανάλυση.*

Τα αποτελέσματα αξιολογήθηκαν ως προς την ειδική τριβή, ή συντελεστή τριβής μ_x οποίος ορίζεται ως

$$\mu_x = \frac{F_x}{F_y} \tag{Β′.10}$$

όπου F_x είναι η τριβή που αντιστέκεται στην κίνηση του δαχτυλιδιού, F_y είναι το κατακόρυφο φορτίο που ασκείται στο δαχτυλίδι και ο δείκτης x αντιστοιχεί στον άξονα της κίνησης του δαχτυλιδιού. Συνολικά, η επίδραση των ΜΣ στο συντελεστή τριβής παρουσιάζεται στις Εικόνες 3.11 & 3.12 και στο Υποκεφάλαιο 3.8 του αγγλικού κειμένου. Συγκεκριμένα, αναζητήθηκε η ΜΣ που είχε τη μεγαλύτερη επιρροή στην ειδική τριβή, διατηρώντας κάθε φορά τις άλλες δύο ΜΣ σταθερές. Η μεταβολή του συντελεστή τριβής ως προς το πλάτος αυλάκωσης με σταθερό βάθος ή βήμα αυλάκωσης απεικονίζεται στα Σχήματα Β′.6 & Β′.7. Σε αυτές είναι εμφανές ότι ο συντελεστής τριβής μειώνεται με την αύξηση του πλάτους αυλάκωσης. Ακόμη, ο ρυθμός μείωσης της ειδικής τριβής είναι μεγαλύτερος για μεγάλα βάθη και μικρά βήματα αυλάκωσης. Αντίστοιχα διαγράμματα έχουν προκύψει για το βάθος και το βήμα της αυλάκωσης, στα οποία οι άλλες δύο ΜΣ παραμένουν σταθερές και βρίσκονται στο Υποκεφάλαιο 3.8. Συνοψίζοντας τις παρατηρήσεις από όλα τα διαγράμματα μεταβολής του συντελεστή τριβής, συμπεραίνεται ότι μειωμένη τριβή επιτυγχάνεται με μικρό βήμα, μεγάλο βάθος και πλάτος αυλάκωσης. Επίσης, μεγαλύτερο κάθετο φορτίο ασκείται στο δαχτυλίδι όταν το χιτώνιο έχει αυλακώσεις με μεγάλο βήμα και μικρό πλάτος, καθώς το βάθος δεν επηρεάζει τις τιμές του πεδίου πίεσης, αλλά την κατανομή του.

Υπολογισμός Παραγόντων Ροής μέσω Προσομοιώσεων ΥΡΔ

Στην αυτοκινητοβιομηχανία, είναι συνήθης η χρήση του μοντέλου μέσης ροής[2], [3], που θεμελιώνεται από την εξίσωση Reynolds για τη μοντελοποίηση της λίπανσης στο εσωτερικό του κυλίνδρου μιας Μηχανής Εσωτερικής Καύσης (ΜΕΚ). Αυτό το μοντέλο αντιμετωπίζει ξεχωριστά την επίδραση της επιφανειακής τραχύτητας και της γεωμετρίας - λειτουργίας της ΜΕΚ στη ροή του λιπαντικού. Η τραχύτητα των επιφανειών λαμβάνεται υπόψη μέσω κάποιων συντελεστών που ονομάζονται παράγοντες ροής και λειτουργούν ως διορθώσεις της παροχής του λιπαντικού που διαρρέει τον κύλινδρο της μηχανής. Οι παράγοντες ροής υπολογίζονται από τις αντίστοιχες ροές των Couette και Poiseuille για ένα ζεύγος επίπεδων πλακών εκ των οποίων η μία έχει ίδια τραχύτητα με αυτήν του χιτωνίου. Ο παράγοντας διάτμησης (shear flow-factor) ϕ_s υπολογίζεται σύμφωνα με τα αποτελέσματα της Couette ροής, ενώ ο παράγοντας πίεσης (pressure flow-factor) ϕ_x σύμφωνα με την Poiseuille ροή και ορίζονται από

$$\phi_s = \frac{Q_{real}}{Q_{Couette}} \tag{Β′.11}$$

$$\phi_x = \frac{Q_{real}}{Q_{Poiseuille}} \tag{Β′.12}$$

όπου Q_{real} είναι η παροχή του λιπαντικού που διαρρέει το ζεύγος των πλακών με τραχύτητα, $Q_{Couette}$ είναι η παροχή της ιδανικής Couette ροής, $Q_{Poiseuille}$ είναι η παροχή

της ιδανικής Poiseuille ροής, δηλαδή της ισοδύναμης ροής του λιπαντικού ανάμεσα στο ζεύγος των λείων, επίπεδων πλακών και ο δείκτης x αντιστοιχεί στον άξονα της κίνησης του λιπαντικού. Αυτοί οι συντελεστές εκφράζουν το μέρος της παροχής που εγκλωβίζεται στις αυλακώσεις της τραχιάς επιφάνειας σε σχέση με την αντίστοιχη μεταξύ των λείων πλακών. Περισσότερες πληροφορίες για τους παράγοντες ροής αναγράφονται στην Ενότητα 2.5.1 του αγγλικού κειμένου, ενώ το μοντέλο της μέσης ροής περιγράφεται στο Υποκεφάλαιο 4.2.2.

Γωνία αυλάκωσης	**0º**	**30º**	**150º**
Βήμα μm	20, 472	472	472
Βάθος μm	1.5	1.5	1.5
Πλάτος μm	20	20	20

Πίνακας Β′.2: *Εναλλακτικοί συνδυασμοί τραχύτητας χιτωνίου.*

Οι παράγοντες ροής συνήθως υπολογίζονται από την εξίσωση Reynolds με σκοπό να προκύψει μια σχέση που συνδέει την τιμή τους με τα χαρακτηριστικά της επιφανειακής τραχύτητας. Εδώ, οι παράγοντες ροής υπολογίστηκαν μέσω προσομοιώσεων ΥΡΔ για τα επιφανειακά χαρακτηριστικά του χιτωνίου που φαίνονται στον Πίνακα Β′.2, έτσι ώστε να βρεθεί η σχέση που συνδέει κάθε flow-factor με το λόγο της κατακόρυφης απόστασης μεταξύ των πλακών προς το βάθος της αυλάκωσης $\frac{h}{D}$. Στην Εικόνα Β′.4 απεικονίζεται η μορφή στοιχειώδους αυλάκωσης για γωνία 150^o. Στη συνέχεια, οι παράγοντες ροής συγκρίθηκαν με τους αντίστοιχους που έχουν προκύψει από την εξίσωση Reynolds, όπως αυτοί παρουσιάζονται στο [1]. Τα αποτελέσματα αυτής της μελέτης για την Couette & Poiseuille ροή παρουσιάζονται στις Ενότητες 4.3.3 & 4.3.4 αντίστοιχα. Επίσης, οι οριακές συνθήκες πίεσης και ταχύτητας για κάθε περίπτωση φαίνονται στα Σχήματα Β′.8 & Β′.9.

Ενδεικτικά, η σύγκριση του παράγοντα πίεσης μεταξύ προσομοιώσεων ΥΡΔ & [1] απεικονίζεται στα Σχήματα Β′.10 & Β′.11 για γωνία αυλάκωσης 30^o και 150^o αντίστοιχα. Σε αυτές, τα αποτελέσματα σχεδόν ταυτίζονται για $\frac{h}{D} \geq 3$ και στις δύο περιπτώσεις. Από την άλλη, για $\frac{h}{D} < 3$, οι παράγοντες αποκλίνουν περισσότερο όσο μειώνεται η απόσταση μεταξύ των πλακών. Οι παράγοντες απέχουν περισσότερο μεταξύ τους ειδικά για γωνία αυλάκωσης 30^o. Η απόκλιση των παραγόντων πίεσης οφείλεται σε τρεις λόγους. Αρχικά, το υπολογιστικό μοντέλο[1] που αξιοποιεί την εξίσωση Reynolds δε λαμβάνει υπόψη το βήμα αυλάκωσης. Δεύτερον, η εξίσωση Reynolds στηρίζεται στην παραδοχή, ότι το λιπαντικό δεν μετακινείται στον άξονα που είναι κάθετος στο επίπεδο της κίνησης. Όμως, από το πεδίο της κατακόρυφης συνιστώσας της ταχύτητας U_y που απεικονίζεται στο Σχήμα Β′.13 είναι προφανές ότι η U_y είναι συγκρίσιμη με την κύρια συνιστώσα της ταχύτητας U_x όπως αυτή παρουσιάζεται στο Σχήμα Β′.12. Συνεπώς, αυτή η απλοποιητική παραδοχή δεν επιβεβαιώνεται από τις προσομοιώσεις ΥΡΔ. Τέλος, η διεύθυνση των αυλακώσεων για γωνία 30^o εμποδίζει τη ροή του λιπαντικού κατά το διαμήκη άξονα. Εκτενής αιτιολόγηση των αποτελεσμάτων αναγράφεται στις Ενότητες 4.3.3 & 4.3.4 του αγγλικού κειμένου.

Ανάπτυξη Εξισώσεων Ροής στο Σχετικό Σύστημα Συντεταγμένων

Η μελέτη επεκτείνεται με τη διατύπωση των εξισώσεων ροής του λιπαντικού στο απόλυτο και στο κινούμενο σύστημα αναφοράς, λαμβάνοντας υπόψη τη σχετική κίνηση του εμβόλου ως προς το χιτώνιο. Συγκεκριμένα, το αδρανειακό ή απόλυτο σύστημα αναφοράς αντιστοιχεί στον κύλινδρο της μηχανής που είναι ακίνητος. Το σχετικό ή κινούμενο σύστημα αναφοράς τοποθετείται στο έμβολο, το οποίο εκτελεί παλινδρομική κίνηση. Είναι επιθυμητό να εκφραστεί η σχετική ροή του λιπαντικού ως προς την απόλυτη ταχύτητα και το ρυθμό μεταβολής της απόστασης μεταξύ των κέντρων του απόλυτου και του σχετικού συστήματος συντεταγμένων. Το προκύπτον σύστημα εξισώσεων προσομοιώνει τη σχετική κίνηση μεταξύ του εμβόλου και του χιτωνίου χωρίς να χρησιμοποιεί υπολογιστικά ακριβούς επιλύτες ροής με κινούμενα πλέγματα. Ακόμη, η ροή εκφράζεται στο σχετικό σύστημα, διότι σε αυτό τα φαινόμενα περιγράφονται πιο εύκολα. Όμως, το σύστημα των εξισώσεων εκφράζεται συναρτήσει της απόλυτης ταχύτητας, για να είναι βολικός ο υπολογισμός των δυνάμεων που ασκούνται σε κάθε σώμα. Το τελικό σύστημα των εξισώσεων ορμής περιγράφεται από

$$\frac{\partial \mathbf{u_I}}{\partial t} + \mathbf{u_I}\cdot\nabla\mathbf{u_I} - \frac{\partial \dot{\mathbf{d}}}{\partial t} - \mathbf{u_I}\cdot\nabla\dot{\mathbf{d}} - \dot{\mathbf{d}}\cdot\nabla\mathbf{u_I} + \dot{\mathbf{d}}\cdot\nabla\dot{\mathbf{d}} = \frac{\nabla p}{\rho} + \nu\nabla\cdot\nabla(\mathbf{u_I} - \dot{\mathbf{d}}) \Leftrightarrow$$
$$\frac{\partial(u_{i,I} - \dot{d}_i)}{\partial t} + u_{i,I}\frac{\partial u_{i,I}}{\partial x_i} - u_{i,I}\frac{\partial \dot{d}_i}{\partial x_i} - \dot{d}_i\frac{\partial u_{i,I}}{\partial x_i} + \dot{d}_i\frac{\partial \dot{d}_i}{\partial x_i} = \frac{1}{\rho}\frac{\partial p}{\partial x_i} + \nu\frac{\partial}{\partial x_i}(\frac{\partial(u_{i,I} - \dot{d}_i)}{\partial x_i}) \tag{B′.13}$$

όπου $\mathbf{u_I}$ το διάνυσμα της ταχύτητας στο αδρανειακό σύστημα αναφοράς (δείκτης I), $\dot{\mathbf{d}}$ το διάνυσμα του ρυθμού μεταβολής της απόστασης μεταξύ των κέντρων των συστημάτων συντεταγμένων, p η πίεση, ρ η πυκνότητα του λιπαντικού, ν η κινηματική συνεκτικότητα και ο δείκτης i = x, y, z στην τανυστική μορφή του συστήματος. Τα βήματα υπολογισμού, καθώς και η γενικότητα της μεθόδου περιγράφονται στην Ενότητα 5.3 του αγγλικού κειμένου.

Σύνοψη - Συμπεράσματα

Συνοψίζοντας, η διπλωματική εργασία ασχολήθηκε με τη διερεύνηση της επίδρασης των επιφανειακών χαρακτηριστικών του χιτωνίου στην ειδική τριβή που ασκείται πάνω στο δαχτυλίδι συμπίεσης μέσω παραμετρικής ανάλυσης. Ακόμη, συνέκρινε εναλλακτικούς τρόπους υπολογισμού των παραγόντων ροής που εφαρμόζονται στο μοντέλο της μέσης ροής. Ολοκληρώθηκε με την ανάπτυξη του συστήματος εξισώσεων ροής του λιπαντικού στο σχετικό σύστημα συντεταγμένων, προκειμένου να ληφθεί υπόψη η σχετική κίνηση μεταξύ εμβόλου και χιτωνίου χωρίς τη χρήση επιλυτών ροής με κινούμενα πλέγματα.

Από την παραμετρική μελέτη συμπεραίνεται ότι μειωμένη τριβή επιτυγχάνεται με βαθιές αυλακώσεις που βρίσκονται κοντά μεταξύ τους. Από την άλλη, αυλακώσεις με μεγάλο βήμα και μικρό πλάτος συνεισφέρουν σε αυξημένο κάθετο φορτίο στο δαχτυλίδι. Το προηγούμενο είναι ανεξάρτητο του βάθους της αυλάκωσης. Έτσι, κατά την επιλογή της τραχύτητας του χιτωνίου απαιτείται ένας συμβιβασμός μεταξύ της μειωμένης τριβής και του αυξημένου κάθετου φορτίου που ασκείται στα δαχτυλίδια του εμβόλου.

Συγκρίνοντας τους παράγοντες ροής που υπολογίστηκαν μέσω προσομοιώσεων ΥΡΔ και [1], παρατηρήθηκε καλή συσχέτιση των αποτελεσμάτων, όταν η απόσταση μεταξύ των πλακών είναι μεγάλη, δηλαδή όταν είναι παχύ το στρώμα λιπαντικού. Στην περίπτωση όπου το πάχος του στρώματος λιπαντικού είναι συγκρίσιμο με το βάθος αυλάκωσης, δεν υπάρχει καλή συσχέτιση μεταξύ αυτών. Οι απόκλιση των αποτελεσμάτων αυξάνει με περαιτέρω μείωση της απόστασης μεταξύ των πλακών. Από αυτήν διαπιστώθηκε ότι η επίδραση του βήματος αυλάκωσης είναι σημαντική στο μέρος της παροχής που εγκλωβίζεται στην τραχιά επιφάνεια. Ακόμη, η απλοποιητική παραδοχή της εξίσωσης Reynolds σχετικά με την κατακόρυφη συνιστώσα της ταχύτητας του λιπαντικού απορρίφθηκε. Συγκεκριμένα, από τις προσομοιώσεις ΥΡΔ προέκυψε ότι η κατακόρυφη συνιστώσα της ταχύτητας είναι συγκρίσιμη με την κύρια συνιστώσα της. Τέλος, η διεύθυνση των αυλακώσεων επηρεάζει σημαντικά τα αποτελέσματα που προκύπτουν από την εξίσωση Reynolds. Η τελευταία δείχνει ότι εγκλωβίζεται περισσότερο λιπαντικό στις αυλακώσεις, διότι το λιπαντικό δεν μπορεί να εξέλθει από τις αυλακώσεις, μόνο να μετακινείται μέσα σε αυτές πάνω στο επίπεδο.

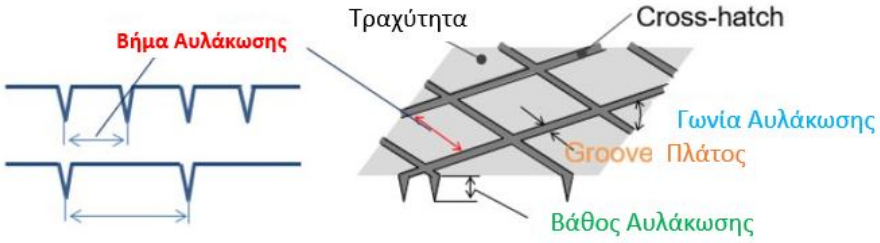

Σχήμα Β′.3: *Τα επιφανειακά χαρακτηριστικά της τραχύτητας του χιτωνίου. Σημειώνονται το βάθος, το βήμα, η γωνία και το πλάτος αυλάκωσης.*

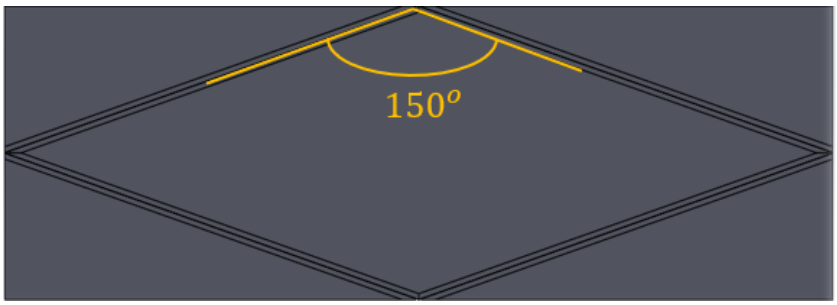

Σχήμα Β′.4: *Επίπεδη πλάκα πάνω από το χαραγμένο τοίχωμα του χιτωνίου για γωνία αυλάκωσης* 150^o*, βάθος 1.5 μm, πλάτος 20 μm και βήμα 472μm.*

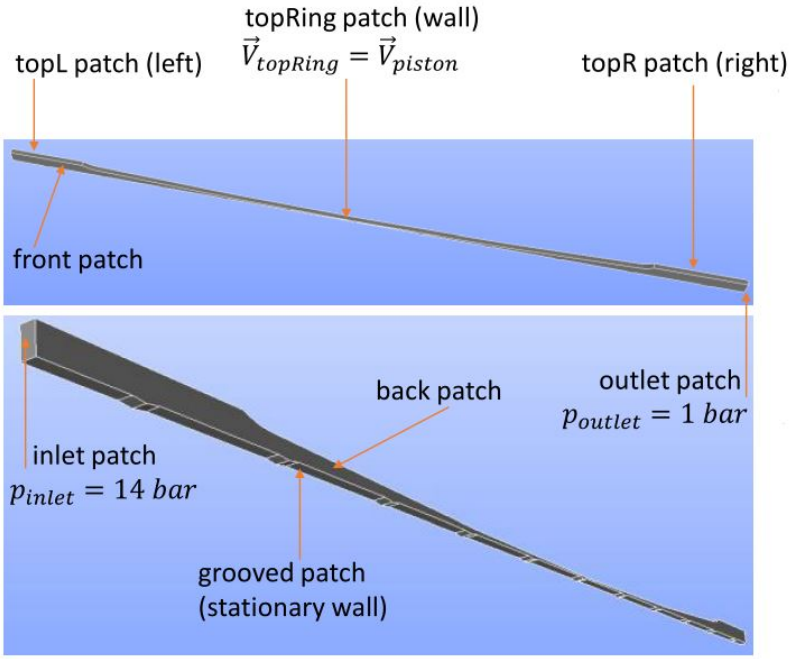

Σχήμα Β′.5: *Το εξεταζόμενο υπολογιστικό χωρίο: Το δαχτυλίδι πάνω από τη χαραγμένη επιφάνεια του χιτωνίου.*

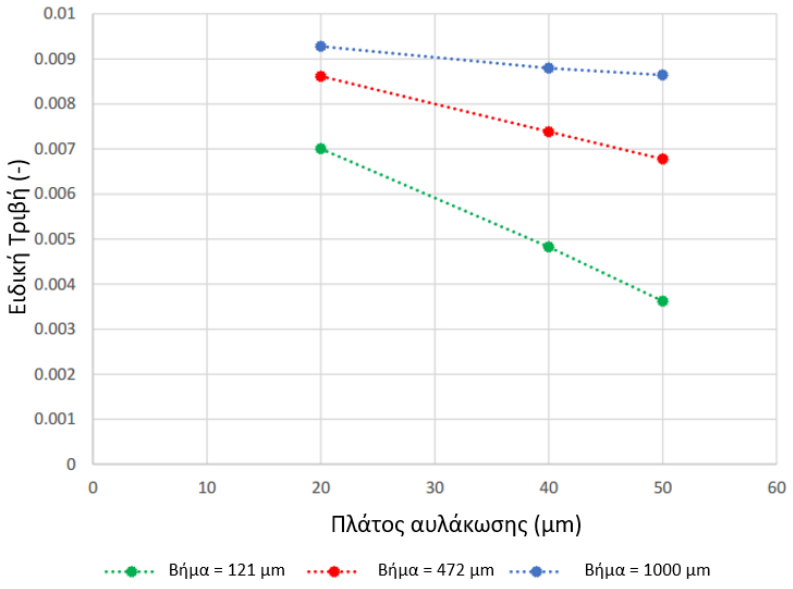

Σχήμα Β′.6: *Μεταβολή του συντελεστή τριβής στο δαχτυλίδι ως προς το πλάτος αυλάκωσης για διαφορετικές τιμές του βήματος.*

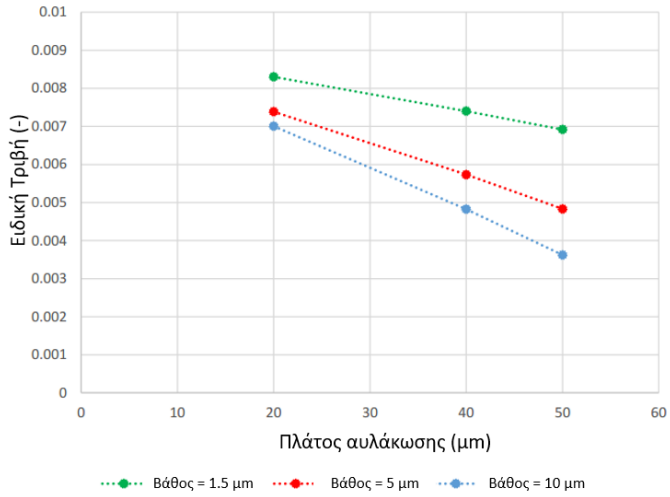

Σχήμα Β'.7: *Μεταβολή του συντελεστή τριβής στο δαχτυλίδι ως προς το πλάτος αυλάκωσης για διαφορετικές τιμές του βάθους.*

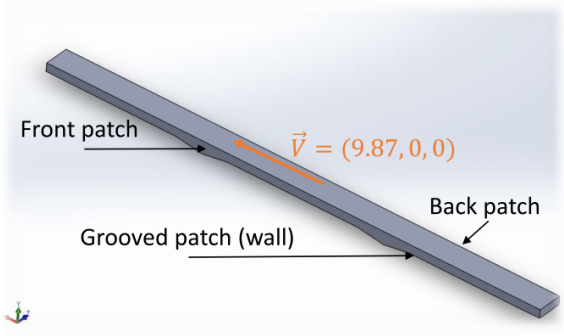

Σχήμα Β'.8: *Couette ροή: Επίπεδη πλάκα πάνω από το χιτώνιο.*

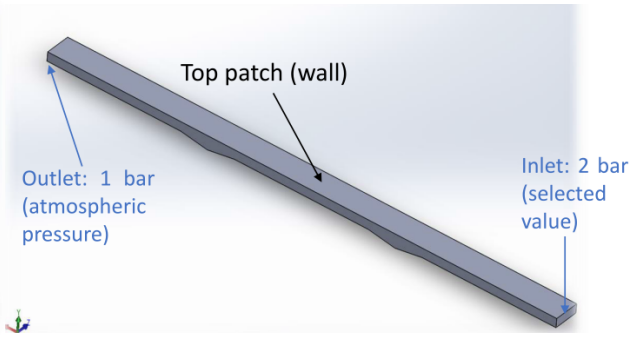

Σχήμα Β'.9: *Poiseuille ροή: Επίπεδη πλάκα πάνω από το χιτώνιο.*

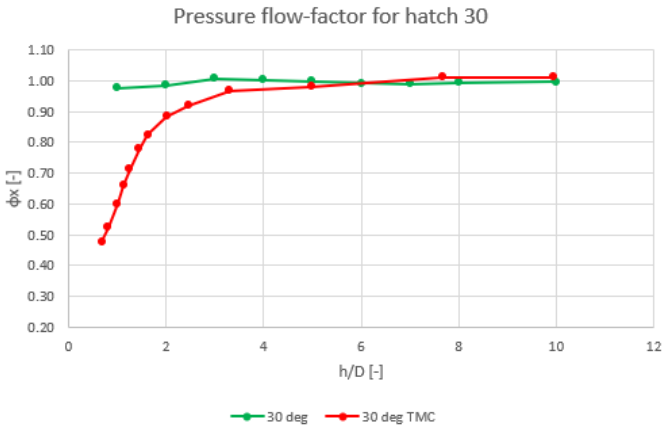

Σχήμα Β'.10: *Σύγκριση Παράγοντα Πίεσης μεταξύ ΥΡΔ &ί [1] για διαφορετικές τιμές του λόγου της απόστασης των πλακών ως προς το βάθος αυλάκωσης* $\frac{h}{D}$ *και γωνία αυλάκωσης* 30^o.

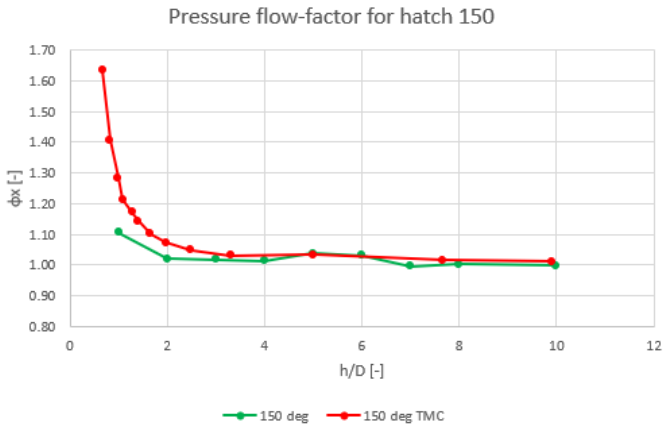

Σχήμα Β'.11: *Σύγκριση Παράγοντα Πίεσης μεταξύ ΥΡΔ & [1] για διαφορετικές τιμές του λόγου της απόστασης των πλακών ως προς το βάθος αυλάκωσης* $\frac{h}{D}$ *και γωνία αυλάκωσης* 150^o.

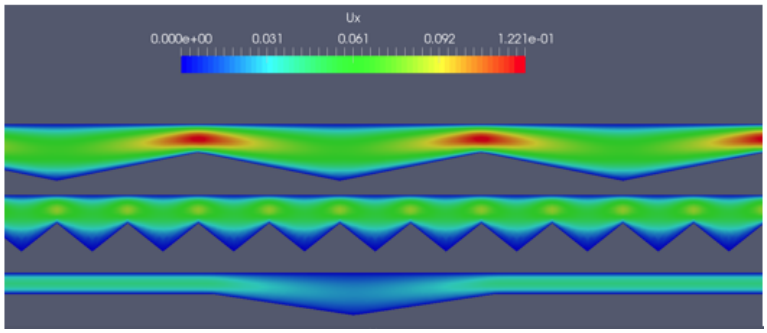

Σχήμα Β'.12: *Η* U_x *συνιστώσα της ταχύτητας με πλάτος*=$20\mu m$, $5\mu m$ *ίσο με το βήμα και για την κατώτατη γεωμετρία πλάτος*=$20\mu m$ *&* *βήμα*=$472\mu m$.

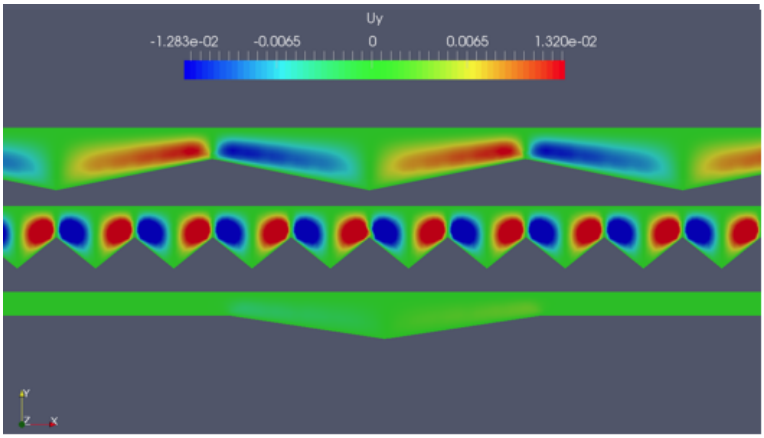

Σχήμα Β'.13: *Η* U_y *συνιστώσα της ταχύτητας με πλάτος*=$20\mu m$, $5\mu m$ *ίσο με το βήμα και για την κατώτατη γεωμετρία πλάτος*=$20\mu m$ *&* *βήμα*=$472\mu m$.

Επιλεγμένη Βιβλιογραφία

[1] S.Sanda, H.Nagakura, N.Katsumi S.Hotta K.Kawai and M.Murakami: Analysis of piston frictional force under engine firing condition - effect of cylinder bore crosshatch angle on friction between piston ring pack and cylinder bore. Transactions of Society of Automotive Engineers of Japan, 45(5):799–804, 2014.

[2] N.Patir and H.S.Cheng: An average flow model for determining effects of three-dimensional roughness on partial hydrodynamic lubrication. ASME. J. of Lubrication Tech, 100(1):12–17, 1978.

[3] N.Patir and H.S.Cheng: Application of average flow model to lubrication between rough sliding surfaces. Journal of Lubrication Technology, 101(2):220–229, 1979.